ABSTRACT

Title of Dissertation: Shape Dynamical Models for Activity Recognition

AND

Coded Aperture Imaging for Light-Field Capture

Ashok Veeraraghavan, Doctor of Philosophy, 2008

Dissertation directed by: Professor Rama Chellappa
Department of Electrical and Computer Engineering

Shape Dynamical Models for Activity Analysis

Classical applications of Pattern recognition in image processing and computer vision have typically dealt with modeling, learning and recognizing static patterns in images and videos. There are, of course, in nature, a whole class of patterns that dynamically evolve over time. Human activities, behaviors of insects and animals, facial expression changes, lip reading, genetic expression profiles are some examples of patterns that are dynamic. Models and algorithms to study these patterns must take into account the nature of the dynamics of these patterns while exploiting the classical pattern recognition techniques. The first part of this dissertation

is an attempt to study and understand such dynamically evolving patterns. We will look at specific instances of such dynamic patterns like Human activities and behaviors of insects and develop algorithms to learn models of such patterns and classify such patterns. The models and algorithms proposed will be validated by extensive experiments on gait based person identification, activity recognition and simultaneous tracking and behavior analysis of insects.

The problem of comparing dynamically deforming shape sequences arises repeatedly in problems like activity recognition and lip reading. We propose, describe and evaluate parametric and non-parametric models for shape sequences. In particular, we emphasize the need to model the execution rate variations and propose a non-parametric model that is invariant to execution-rate variations. These models and the resulting algorithms are shown to be extremely effective for a wide range of applications from gait based person identification to human action recognition. We further show that the shape dynamical models are not only effective for the problem of recognition, but also can be used as effective priors for the problem of simultaneous tracking and behavior analysis. We validate the proposed algorithm for performing simultaneous behavior analysis and tracking on videos of bees dancing in a hive.

Coded Aperture Imaging for Light-Field Capture

Computational Imaging is an emerging field where the process of image formation involves the use of a computer. The current trend in computational imaging is to capture as much information about the scene as possible during capture time so that appropriate images with varying focus, aperture, blur and colorimetric settings may be rendered as required. In this regard, capturing the 4D light-field as opposed to a 2D image allows us to freely vary viewpoint and focus at the time

of rendering an image. In this dissertation, we describe a theoretical framework for reversibly modulating 4D light fields using an attenuating mask in the optical path of a lens based camera. Based on this framework, we present a novel design to reconstruct the 4D light field from a 2D camera image without any additional refractive elements as required by previous light field cameras. The patterned mask attenuates light rays inside the camera instead of bending them, and the attenuation recoverably encodes the rays on the 2D sensor. Our mask-equipped camera focuses just as a traditional camera to capture conventional 2D photos at full sensor resolution, but the raw pixel values also hold a modulated 4D light field. The light field can be recovered by rearranging the tiles of the 2D Fourier transform of sensor values into 4D planes, and computing the inverse Fourier transform. In addition, one can also recover the full resolution image information for the in-focus parts of the scene.

Shape Dynamical Models for Activity Analysis

AND

Coded Aperture Imaging for Light-Field Capture

by

Ashok Veeraraghavan

Dissertation submitted to the Faculty of the Graduate School of the
University of Maryland, College Park in partial fulfillment
of the requirements for the degree of
Doctor of Philosophy
2008

Advisory Committee:

Professor Rama Chellappa, Chair / Advisor
Professor P.S.Krishnaprasad
Professor Min Wu
Professor Anuj Srivastava
Professor Ramesh Raskar
Professor Amitabh Varshney

DEDICATION

To my Grandfather

ACKNOWLEDGEMENTS

TABLE OF CONTENTS

LIST OF TABLES

LIST OF FIGURES

Chapter 1

Introduction

1.1 Research Motivation

Classical applications of Pattern recognition in image processing and computer vision have typically dealt with modeling, learning and recognizing static patterns in images and videos. There are, of course, in nature, a whole class of patterns that dynamically evolve over time. Human activities, behaviors of insects and animals, facial expression changes, lip reading, genetic expression profiles are some examples of patterns that are dynamic. Models and algorithms to study these patterns must take into account the nature of the dynamics of these patterns while exploiting the classical pattern recognition techniques. In the first part of this dissertation, I will develop and evaluate algorithms to model, learn and recognize such dynamic patterns. In particular, I pay special attention to modeling and comparing shape sequences. Several important computer vision applications in human activity analysis can be formulated as a problem of modeling and comparing shape sequences. I will demonstrate and evaluate these shape-dynamical models on computer vision applications such as human action recognition and gait based

human identification.

The second part of this dissertation concerns an interesting application in computational imaging. Computational Imaging is an emerging field where the process of image formation involves the use of a computer. The current trend in computational imaging is to capture as much information about the scene as possible during capture time so that appropriate images with varying focus, aperture, blur and colorimetric settings may be rendered as required. In this regard, capturing the 4D light-field as opposed to a 2D image allows us to freely vary viewpoint and focus at the time of rendering an image. I describe a theoretical framework for reversibly modulating 4D light fields using an attenuating mask in the optical path of a lens based camera. Based on this framework, we present a novel design to reconstruct the 4D light field from a 2D camera image without any additional refractive elements as required by previous light field cameras. The patterned mask attenuates light rays inside the camera instead of bending them, and the attenuation recoverably encodes the rays on the 2D sensor. The mask-equipped camera focuses just as a traditional camera to capture conventional 2D photos at full sensor resolution, but the raw pixel values also hold a modulated 4D light field. The light field can be recovered by rearranging the tiles of the 2D Fourier transform of sensor values into 4D planes, and computing the inverse Fourier transform. In addition, one can also recover the full resolution image information for the in-focus parts of the scene.

1.2 Thesis Contributions

The specific contributions of this thesis are

1. I propose and evaluate several parametric and non-parametric algorithms for comparing shape sequences. The parametric algorithms are based on traditional models such as Hidden Markov model (HMM) and Autoregressive and moving average model (ARMA), while the non-parametric algorithm is based on dynamic programming. These contributions are described in detail in Chapter 2.

2. I study and analyse the importance of execution rate variations in human action analysis and recognition. I model the variations in execution rate by using a composite model. In the composite model, the variations due to external conditions such as illumination, viewpoint and camera parameters are modeled as affecting the feature extracted while the variations due to execution rate are modeled explicitly. The probability distribution of execution rate variations are learnt explicitly and are used in a Bayesian algorithm for execution rate-invariant action recognition. The details of the algorithm and some special cases are discussed in Chapter 3.

3. The importance of shape dynamical models is not restricted to the problem of activity recognition alone. Accurate shape dynamical models may also serve as priors that enable accurate tracking of subjects in a video. This leads to a simultaneous tracking and behavior analysis framework. I describe this simultaneous tracking and behavior analysis framework in Chapter 4 and apply this framework to the problem of tracking and analysis of dances of bees in a hive.

4. Finally, this thesis also makes a significant contribution to the emerging field of computational imaging. I propose a theoretical framework for reversibly

modulating 4D light fields using an attenuating mask in the optical path of a lens based camera. Based on this framework, I present a novel design to reconstruct the 4D light field from a 2D camera image without any additional refractive elements as required by previous light field cameras. The patterned mask attenuates light rays inside the camera instead of bending them, and the attenuation recoverably encodes the rays on the 2D sensor. The light field can be recovered by rearranging the tiles of the 2D Fourier transform of sensor values into 4D planes, and computing the inverse Fourier transform.

1.3 Comparing Shape Sequences

In typical video processing tasks the input is a video of an object or a set of objects that deform or change their relative poses. The essential information conveyed by the video can be usually captured by analyzing the boundary (shape) of each object as it changes with time. The manner in which this shape change occurs provides clues about the nature of the object and sometimes even about the activity performed by the object. There are many such cases where the nature of shape changes of silhouette of a human provides information about the activity performed by the human. Consider the images shown in Fig:1.1. It is not very difficult to perceive the fact that these represent the silhouette of a walking human. Apart from providing information about the activity being performed, there are also several instances when the manner of shape changes provides valuable insights regarding the identity of the object. Therefore, it is important to be able to learn the dynamics of shape changes or at the least to be able to compute meaningful distances between such shape sequences. In Chapter 2 we describe algorithms for comparing shape sequences and evaluate the performance of these algorithms on

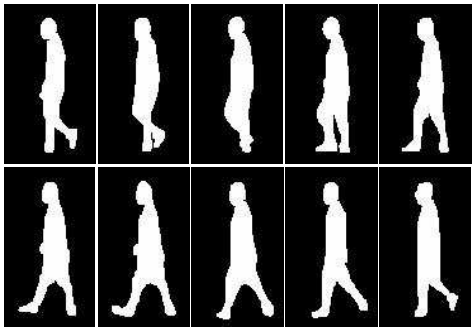

Figure 1.1: Sequence of shapes as a person walks frontoparallely

the problem of gait based person identification.

We begin by providing a literature review of the research in shape analysis. The interested reader may refer to comprehensive surveys of the field [102], [164]. Since the experimental results are for the problem of gait recognition we also provide a brief summary of prior work in gait-based person authentication. Special emphasis is given to understanding the role of shape and kinematics in gait recognition since our experiments lead to interesting observations on this issue.

1.3.1 Previous Work in Shape Analysis

Pavlidis [125] categorized shape descriptors into various taxonomies according to different criteria. Descriptors that use the points on the boundary of the shape are called external descriptors (or boundary descriptors) [87] [127] [7] while those that describe the interior of the object are called internal descriptors (or global descriptors) [17] [72]. Descriptors that represent shape as a scalar or as a feature vector are called numeric descriptors while those like the medial axis transform that describes the shape as another image are called non-numeric descriptors. Descriptors are also classified as information preserving or not based on whether

the descriptor allows accurate lossless reconstruction of a shape.

Global Methods for shape matching

Global shape matching procedures treat the object as a whole and describe it using some features extracted from the object. The disadvantage of these methods is that it assumes that the image given must be segmented into various objects which by itself is not an easy problem. In general, these methods cannot handle occlusion and are not very robust to noise in the segmentation process. Popular moment based descriptors of the object such as [72], [90], [28] are global and numeric descriptors. Goshtasby [63] used the pixel values corresponding to polar coordinates centered around the center of mass of the shape, the shape matrix, as a description of the shape. Parui et. al. [124] used relative areas occupied by the object in concentric rings around the centroid of the objects as a description of the shape. Blum and Nagel [17] used the medial axis transform to represent the shape.

Boundary methods for shape matching

Shape matching methods based on the boundary of the object or on a set of pre-defined landmarks on the object have the advantage that they can be represented using a one dimensional function. In the early sixties, Freeman [53] used chain coding (a method for coding line drawings) for the description of shapes. Arkin et al. [6] used the turning function for comparing polygonal shapes. Persoon and Fu [127] described the boundary as a complex function of the arc length. Kashyap and Chellappa [87] used a circular autoregressive model of the distance from the centroid to the boundary to describe the shape. The problem with a Fourier

representation [127] and the autoregressive representation [87] is that the local information is lost in these methods. Srivastava et al. [149] propose differential geometric representations of continuous planar shapes.

Recently several authors have described shape as a set of finite ordered landmarks. Kendall [88] provided a mathematical theory for the description of landmark based shapes. Bookstein [20] and later Dryden and Mardia [43] have furthered the understanding of such landmark based shape descriptions. There has been a lot of work on planar shapes [130] and [57]. Prentice and Mardia [130] provided a statistical analysis of shapes formed by matched pairs of landmarks on the plane. They provided inference procedures on the complex plane and a measure of shape change in the plane. Berthilsson [8] and Dryden [42] describe a statistical theory for shape spaces. Projective shape and their respective invariants are discussed in [8] while shape models, metrics and their role in high level vision is discussed in [42]. The shape context [7] of a particular point in a point set captures the distribution of the other points with respect to it. [7] uses the shape context for the problem of object recognition. The softassign Procrustes matching algorithm [132] simultaneously establishes correspondences and determines the Procrustes fit.

Dynamics of shapes

The recent explosion in the area of shape discrimination and shape retrieval can be attributed to their effectiveness in object recognition and shape based image retrieval. Inspite of these recent developments there has been very few studies on the variation of object shape as a cue for object recognition and activity classification. Yezzi and Soatto [175] separate the overall motion from deformation in a

sequence of shapes. They use the notion of shape average to differentiate global motion of a shape from the deformations of a shape. [104] proposes a notion of dynamic averages for shape sequences using dynamic time warping for allignment. Vaswani et al. [158] used the dynamics of a configuration of interacting objects to perform activity classification. They apply the learned dynamics for the problem of detecting abnormal activities in a surveillance scenario. Recently, Liu and Ahuja [98] have proposed using autoregressive models on the Fourier descriptors for learning the dynamics of a 'dynamic shape'. They use this model for performing object recognition, synthesis and prediction. Refer to [146], [12] and references therein for the treatment of some related work in the area of tracking subspaces. Mowbray and Nixon [106] use spatio-temporal Fourier descriptors to model the shape descriptions of temporally deforming objects and perform gait recognition experiments using their shape descriptor.

1.3.2 Prior Work in Gait recognition

The study of human gait has recently been driven by its potential use as a biometric for person identification. Since we evaluate the methods for comparing shape sequences on the problem of gait based human identification, here we outline some of the prior work in gait-based human identification.

Shape based methods

Niyogi and Adelson [115] obtained spatio-temporal solids by aligning consecutive images and use a weighted Euclidean distance for recognition. Phillips et al. [129] provide a baseline algorithm for gait recognition using silhouette correlation. Han and Bhanu [68] use the gait energy image while Wang et al. use Procrustes shape

analysis for recognition [167]. Foster et al. [51] use area based features. Bobick and Johnson [19] use activity specific static and stride parameters to perform recognition. Collins et al. build a silhouette based nearest neighbor classifier [32] to do recognition. Several researchers [85] [94] have used Hidden Markov Models (HMM) for the task of gait based identification. Another shape based method for identifying individuals from noisy silhouettes is provided in [152].

Kinematics based methods

Apart from these image based approaches Cunado et al. [34] model the movement of thighs as articulated pendulums and extract a gait signature. But in such an approach robust estimation of thigh position from a video can be very difficult. [11] provides a method for gait recognition using dynamic affine invariants. In another kinematics based approach [10], trajectories of the various parameters of a kinematic model of the human body are used to learn a dynamical system. A model invalidation approach for recognition using a model similar to [10] is provided in [105]. Tanawongsuwan and Bobick [151] have developed a normalization prcedure that maps gait features across different speeds in order to compensate for the inherent changes in gait features associated with the speed of walking. All the above methods have both static (shape) aspects and dynamic features used for gait recognition. Yet the relative importance of shape and dynamics in human motion has not been investigated. The experimental results presented in this dissertation shed some light on this issue.

Role of shape and kinematics in human gait

Johansson [81] attached light displays to various body parts and showed that humans can identify motion with the pattern generated by a set of moving dots. Since Muybridge [109] captured photographic recordings of human and animal locomotion, considerable effort has been made in the computer vision, artificial intelligence and image processing communities to the understanding of human activities from videos. A survey of work in human motion analysis can be found in [56].

Several studies have been done on the various cues that humans use for gait recognition. Hoenkamp [70] studied the various perceptual factors that contribute to the labeling of human gait. Medical studies [108] suggest that there are 24 different components to human gait. If all these different components are considered then it is claimed that the gait signature is unique. Since it is very difficult to extract these components reliably several other representations have been used. It has been shown [35] that humans can do gait recognition even in the absence of familiarity cues. Cutting and Kozlowski also suggest that dynamic cues like speed, bounciness and rhythm are more important for human recognition than static cues like height. Cutting and Proffitt [36] argue that motion is not the simple compilation of static forms and claim that it is a dynamic invariant that determines event perception. Moreover, they also found that dynamics was crucial to gender discrimination using gait. Therefore, it is intuitive to expect that dynamics also plays a role in person identification though shape information might also be equally important. Interestingly, Veres et al. [165] recently did a statistical analysis of the image information that is important in gait recognition and concluded that static information is more relevant than dynamical information. In the light of such

developments, our experiments explore the importance of shape and dynamics in human movement analysis from the perspective of computer vision and analyze their role in existing gait recognition methodologies.

1.4 Modeling Execution Rate Variations for Action Recognition

One of the principal disadvantages of traditional methods for comparing shape sequences is the inability to account for systematic variations in the execution-rates. In activity recognition, different instances of the same activity may consist of varying relative speeds at which the various actions are executed, in addition to other intra- and inter- person variabilities. Most existing algorithms for activity recognition, even if robust to intra- and inter-personal changes of the same activity, are extremely sensitive to warping of the temporal axis due to variations in speed profile. In Chapter 3, we propose a model that can account for variations in feature due to execution rate variations in vision based human activity recognition. Here, we provide a brief literature review of some of the related earlier work in human activity recognition with special emphasis on execution rate variations.

1.4.1 Prior Work in Activity Recognition:

One of the earliest investigations about the nature of human movement was the study done by photographers Etienne Jules Marey and Eadweard Muybridge [109] in the 1850s. They captured photographs of several moving subjects that revealed various interesting aspects of human and animal locomotion. The classic Moving Light Display (MLD) experiment of Johansson [81] provided a great impetus to the

study and analysis of human motion perception in the field of neuroscience. This then paved the way for mathematical modeling of human action and automatic recognition, which naturally fell into the purview of computer vision.

Activity recognition has attracted tremendous interest in recent years because of its potential in applications such as surveillance, security, and human body animation. Activity recognition has been an active research area since the 90's. The reader can refer to the different surveys [4] [25] [55] on activity recognition for a detailed review of previous research in this area. [4] discusses the important issues in an action recognition system while [25] provides a detailed review of the motion based approaches. Broadly action recognition has either been studied using probabilistic graphical models such as hidden markov models [172] [21] [166] [71] and dynamic Bayesian networks [74] [60] [123] [27] [92]. Since our approach is an attempt to account for the variabilities that affect action recognition, we provide a more indepth coverage of prior work in this area. Recently, [141] has explicitly enumerated the three most important sources that contribute to variabilities in human activity videos as a) Viewpoint change, b) Anthropometry of actors and c) Execution rate.

Viewpoint and Anthropometry

Typical approaches for human action recognition begin by extracting features from a single frame or a small set of frames. These features could be simple motion-based features such as optical flow [73], and point trajectories [133], or simple silhouette based features such as binary background subtracted images [101] or shape features [161]. Irrespective of the actual feature used for representation, it becomes extremely important to ensure that these features are then invariant

to viewpoint of the camera and the body stature of the subject (anthropometry). Most approaches use simple scaling based laws to account for anthropometry while more sophisticated approaches including affine invariance are required in order to account for view invariance.

The maximal points of 3D space-time curvature of tracked points are shown to be invariant to viewpoint and therefore used as features for action recognition [133]. Assuming the subject is far enough from the camera, an approach to synthesize side views of subjects from non-side views is proposed and used for view-invariant gait recognition in [84]. [122] presents an approach for extracting 3D model based invariants from 2D images and describes how these invariants may be used in an action recognition algorithm. Another popular approach for action recognition is to represent the action as a 3D spatio-temporal volume and then incorporate some measure of view invariance into features extracted from these 3D spatio-temporal volumes as described in [30] [176] [16] [37]. Shechtman and Irani [140] present an approach based on space-time motion based correlation to match actions with a template. Recently, body stature statistics have been used in order to account for variations in features due to anthropometry [65].

Execution Rate

Inspite of this large body of work in accounting for viewpoint and anthropometry invariance very little has been done to account for the variability in the execution rate of the actors. Results on gait-based person identification shown in [18] indicate that it is very important to take into account the temporal variations in the person's gait. In [159], we presented some preliminary work indicating that accounting for execution rate enhances recognition performance for action recognition. Typical

approaches for accounting for variations in execution rate are either directly based on the dynamic time warping (DTW) algorithm [131] or some variation of this algorithm [159]. A method for computing an average shape for a set of dynamic shapes is provided in [104]. A functional curve synchronisation model to estimate a longitudinal average (referred to as "functional convex average") is presented in [100]. Neither of these methods address the issue of learning the nature of time-warping transformations for each class from the data. A method to learn the best class of time-warping transformations for a given classification problem is proposed in [135].

1.5 Simultaneous Tracking and Behavior Analysis

Accurate shape dynamical models are not only efficient for the problem of recognition, but they also serve as effective priors that enable accurate tracking of subjects in video. In Chapter 4, we show how accurate shape dynamical models can be used for simultaneous tracking and behavior analysis. We apply these principles to the problem of tracking the position, orientation and the behavior of bees in a hive. We present a system that can be used to analyze the behavior of insects and, more broadly, provide a general framework for the representation and analysis of complex behaviors.

Behavioral research in the study of the organizational structure and communication forms in social insects like the ants and bees has received much attention in recent years [54] [145]. Such a study has provided some practical models for tasks like work organization, reliable distributed communication, navigation

etc [112] [107]. Usually, when such an experiment to study these insects is setup, the insects in an observation hive are videotaped. The hours of video data are then manually studied and hand-labeled. This task of manually labeling the video data takes up the bulk of the time and effort in such experiments. In this chapter, we discuss general methodologies for automatic labeling of such videos and provide an example by following the approach for analyzing the movement of bees in a bee hive. Contrary to traditional approaches that first track objects in video and then recognize behaviors using the extracted trajectories, we propose to simultaneously track and recognize behaviors. In such a joint approach, accurate modeling of behaviors act as priors for motion tracking and significantly enhances motion tracking while accurate and reliable motion tracking enables behavior analysis and recognition.

1.5.1 Prior Work in Tracking:

There has been significant work on tracking objects in video. Most tracking methodologies can be classified as either deterministic or stochastic. Deterministic approaches solve an optimization problem under a prescribed cost function [67] [33]. Stochastic approaches estimate posterior distribution of the position of the object in the current frame using a Kalman filter or particle filters [24] [39] [76] [99] [179] [89]. Most of these do not directly adapt well to tracking insects because they exhibit very specific forms of motion (for example, bees can turn by a right angle within 2 or 3 frames). In order to extend such tracking methods, it is important to consider the anatomy (body parts) of these insects and incorporate both their structure and the nature of their motions in the tracking algorithm.

The use of prior shape and motion models to facilitate tracking has been re-

cently explored in several works for the problem of human body tracking. The shape of the human body has been modeled as anything ranging from a simple stick-figure model [93] to a complex super-quadric model [143]. Several tracking algorithms use motion models (like constant velocity model, random walk model etc) for tracking [76] [89] [13] [179]. There have also been some recent attempts to model specific motion characteristics of the human body to aid as priors in tracking [178] [29] [22] [177] [126].

Previous work on tracking insects has concentrated on speed and reliability of estimating just the position of the center of insects in videos [89] [116]. Inspired by the studies in human body tracking mentioned above, we explore the effectiveness of higher level shape and motion models for the problem of tracking insects in their hives. We believe that such methods lead to algorithms where tracking and behavior analysis can both be performed simultaneously i.e., while these motion priors aid reliable tracking, the parameters of the motion models also encode information about the nature of behavior being exhibited. We model the behaviors exhibited by the insect using Markov motion models and use these models as priors in a tracking framework to reliably estimate the location and the orientation of the various body parts of the insect. We also show that it is possible to make inferences about the behavior of the insect using the parameters estimated via the motion model.

1.5.2 Prior Work in Analyzing Bee Dances

There is a great deal of interest, and a significant need for developing automated methods for (a) detecting dancing bees in video sequences (b) accurately tracking dance trajectories and (c) extracting the dance parameters described above. But in

most of these cases, the experimenters manually study the videos of bee dances and annotate the various bee dances. This is usually time-consuming, tiring and error-prone. Some recent efforts into automating such tasks have started emerging with the advances made in vision based tracking systems. [47] suggests the use of Markov models for identifying certain segments of the dances but this method relies on the availability of manually labeled data. [89] suggests the use of a Rao-Blackwellized particle filter to track the center of the bee during dances. The work does not address the issue of behavioral analysis once tracking is done. Moreover, some of the parameters of the dances that are essential for decoding the dance like the orientation of the thorax during the waggle etc., are not estimated directly. [116] suggests the use of parametric switched linear dynamical system (p-SLDS) for learning motions that exhibit systematic temporal and spatial variations. They use the position tracking algorithm proposed by [89] and obtain trajectories of the bees in the videos. An Expectation-Maximization based algorithm is used for learning the p-SLDS parameters from these trajectories. Much in the same spirit, we also model the various behaviors explicitly using hierarchical Markov models (which can be viewed as SLDS). Nevertheless, while position tracking and behavior interpretation are completely independent in their system, here, we close the loop between position tracking and behavior inference thereby enabling persistent and simultaneous tracking and behavior analysis. In such a "simultaneous tracking and behavioral analysis approach" the behavior modeling enhances tracking accuracy while the tracking results enable accurate interpretation of behaviors.

1.6 Coded Aperture Imaging for Light-Field Capture

Another contribution of this dissertation is to the field of computational imaging. The current trend in computational imaging is to capture more optical information at the time of capture to allow greater post-capture image processing abilities. In this regard, we are interested in the capture of light-fields as opposed to traditional 2D images. Light fields characterizes the irradiance of each ray in space using a 4 dimensional twin plane parameterization (Levoy and Hanrahan [96] and Gortler et. al. [62]). By capturing a light field of the scene, all information content about the scene appearance can be obtained. Digital cameras, however, are able to sample only a 2-dimensional projection of this light-field, as sensors are limited to be 2-dimensional surfaces and are typically isotropic with respect to direction of incident rays.

In order to capture the information content in the entire light-field, it is necessary to modulate/transform it so that the information in the angular dimensions can be sampled by the sensor. Several optical elements perform this modulation in previously proposed capture devices. A straightforward way to sample angular dimensions is viewpoint sampling. This can achieved by using a dense array of cameras, one for each viewpoint as in [171]. Such dense camera arrays, however, are impractical for consumer applications since they introduce a host of synchronization and networking issues apart from their sheer bulk. In Chapter 5, we propose 'non-refractive' modulators and show that these modulators are actually a very powerful class of modulators that can be used to design many of the optical devices that were previously designed using precise refractive modulators like

microlens arrays. In particular, we show a design of a light-field camera that uses just a patterned mask inside a traditional camera. The pattern on the mask acts as a powerful 4D modulator that modulates the incoming light-field and enables multiplexing the 4D light-field onto the 2D sensor.

1.6.1 Related Work

Light Field Acquisition: Integral Photography [97] was first proposed almost a century ago to undo the directional integration of all rays arriving at one point on a film plane or sensor, and instead measure each incoming direction separately to estimate the entire 4D function. For a good survey of these first integral cameras and its variants, see [80, 103, 118]. The concept of the 4D light field as a representation of all rays of light in free-space was proposed by Levoy and Hanrahan [96] and Gortler et al [62]. While both created images from virtual viewpoints, Levoy and Hanrahan [96] also proposed computing images through a virtual aperture, but a practical method for computing such images was not demonstrated until the thorough study of 4D interpolation and filtering by Isaksen *et al.* [75]. Similar methods have also been called synthetic aperture photography in more recent research literature [95, 154].

To capture 4D radiance onto a 2D sensor, following two approaches are popular. The first approach uses an array of lenses to capture the scene from an orderly grid of viewpoints, and the image formed behind each lens provides an orderly grid of angular samples to provide a result similar to integral photography [78, 97]. Instead of fixed lens arrays, Wilburn *et al.* [171] perfected an optically equivalent configuration of individual digital cameras. Georgiev *et al.* [58] and Okano *et al.* [119] place an array of positive lenses (aided by prisms in [58]) in front of a

conventional camera. The second approach places a single large lens in front of an array of micro-lenses treating each sub-lens for spatial samples. These *plenoptic cameras* by Adelson *et al.* [2] and Ng *et al.* [113] form an image on the array of lenslets, each of which creates an image sampling the angular distribution of radiance at that point. This approach swaps the placement of spatial and angular samples on the image plane. Both these approaches trade spatial resolution for the ability to resolve angular differences. They require very precise alignment of microlenses with respect to sensor.

Our mask-based heterodyne light field camera is conceptually different from previous camera designs in two ways. First, it uses *non-refractive* optics, as opposed to refractive optics such as microlens array [113]. Secondly, while previous designs sample individual rays on the sensor, mask-based design samples *linear combination* of rays in Fourier space. Our approach also trades spatial resolution for angular resolution, but the 4D radiance is captured using information-preserving coding directly in the Fourier domain. Moreover, we retain the ability to obtain full resolution information for parts of the scene that were in-focus at capture time.

Coded Imaging: In astronomy, coded aperture imaging [142] is used to overcome the limitations of a pinhole camera. Modified Uniformly Redundant Arrays (MURA) [64] are used to code the light distribution of distant stars. A coded exposure camera [134] can preserve high spatial frequencies in a motion-blurred image and make the deblurring process well-posed. Other types of imaging modulators include mirrors [48], holograms [150], stack of light attenuating layers [180] and digital micro-mirror arrays [110]. Previous work involving lenses and coded masks is rather limited. Hiura & Matsuyama [69] placed a mask with four pin

holes in front of the main lens and estimate depth from defocus by capturing multiple images. However, we capture a single image and hence lack the ability of compute depth at every pixel from the information in defocus blur. Nayar & Mitsunaga [111] place an optical mask with spatially varying transmittance close to the sensor for high dynamic range imaging.

Wavefront Coding [40, 41, 155] is another technique to achieve extended *Depth of Field (DOF)* that use aspheric lenses to produce images with a depth-independent blur. While their results in producing extended depth of field images are compelling, their design cannot provide a light field. Our design provides greater flexibility in image formation since we just use a patterned mask apart from being able to recover the light field. Passive ranging through coded apertures has also been studied in the context of both wavefront coding [82] and traditional lens based system [46].

Several deblurring and deconvolution techniques have also been used to recover higher spatial frequency content. Such techniques include extended DOF images by refocusing a light field at multiple depths and applying the digital photomontage technique (Agarwala *et al.* [3]) and fusion of multiple blurred images ([66]).

1.7 Organization of the Thesis

- Chapter 2 introduces the problem of comparing shape sequences and presents parametric and non-parametric algorithms for comparing shape sequences. The presented algorithms are rigorously evaluated on publicly available gait based person identification datasets. Interesting observations about the role of shape and kinematics in gait based person identification are also made.

- Chapter 3 motivates the need to model execution rate variations in order to perform effective human activity recognition. A model to learn the systematic execution rate variations in a class specific manner and a Bayesian algorithm to perform activity recognition in the presence of such execution-rate variations are presented. A special case which leads to a fast dynamic programming based inference algorithm is also highlighted.

- Chapter 4 describes how accurate shape dynamical models may be used as effective priors for the problem of simultaneous tracking and behavior analysis. A system is presented where complex beavhiors are modeled as hierarchical markov motion models and these act as priors in a particle filter based tracking algorithm. These principles are then applied to the problem of tracking and analysing the behavior of bees in a hive.

- Chapter 5 describes a new theoretical framework for reversibly modulating 4D light fields using an attenuating mask in the optical path of a lens based camera. Based on this framework, a novel design to reconstruct the 4D light field from a 2D camera image without any additional refractive elements as required by previous light field cameras is proposed.

- Finally, Chapter 6 discusses the conclusions of this thesis and postulates future directions of study.

Chapter 2

Comparing Shape Sequences

In typical video processing tasks the input is a video of an object or a set of objects that deform or change their relative poses. The essential information conveyed by the video can be usually captured by analyzing the boundary (shape) of each object as it changes with time. The manner in which this shape change occurs provides clues about the nature of the object and sometimes even about the activity performed by the object. Consider the manner in which the shape of the lip changes when we speak. The manner in which the shape of the lip changes during speech provides significant information about the actual words that are being spoken. Consider the two words 'arrange' and 'ranger'. If we take discrete snapshots of the shape of the lip during each of these words we see that the two sets of snapshots will be identical(or almost identical) though the ordering of the discrete snapshots will be very different for these two utterances. Therefore any method that inherently does not learn/use the dynamics information of this shape change will declare that these two utterances are very close to each other while in reality these are very different words. Therefore, in cases such as this, where shape change is critical to recognition, it is important to consider the entire shape sequence, i.e.,

the shape sequence is more important than the individual shapes at discrete time instants. There are many such cases where the nature of shape changes of silhouette of a human provides information about the activity performed by the human. Consider the images shown in Fig:2.1. It is not very difficult to perceive the fact that these represent the silhouette of a walking human. Apart from providing information about the activity being performed, there are also several instances when the manner of shape changes provides valuable insights regarding the identity of the object. Even though the outline of the shape of both a lion and a cheetah are very similar (with four legs etc) especially in its profile view, the manner in which a lion and a cheetah move are so drastically different. The discrimination between two such classes is significantly improved if we take the manner of shape changes into account. Thus it is important to be able to learn the dynamics of shape changes or at the least to be able to compute meaningful distances between such shape sequences. We describe both parametric and non-parametric methods to compute meaningful distance measures between two such sequences of deforming shapes. The methods provided are generic and can be used to characterize the time evolution of any set of landmark points, not necessarily on the silhouette of the object.

2.0.1 Prior Work

The recent explosion in the area of shape discrimination and shape retrieval can be attributed to their effectiveness in object recognition and shape based image retrieval. Inspite of these recent developments there has been very few studies on the variation of object shape as a cue for object recognition and activity classification. Yezzi and Soatto [175] separate the overall motion from deformation in a sequence

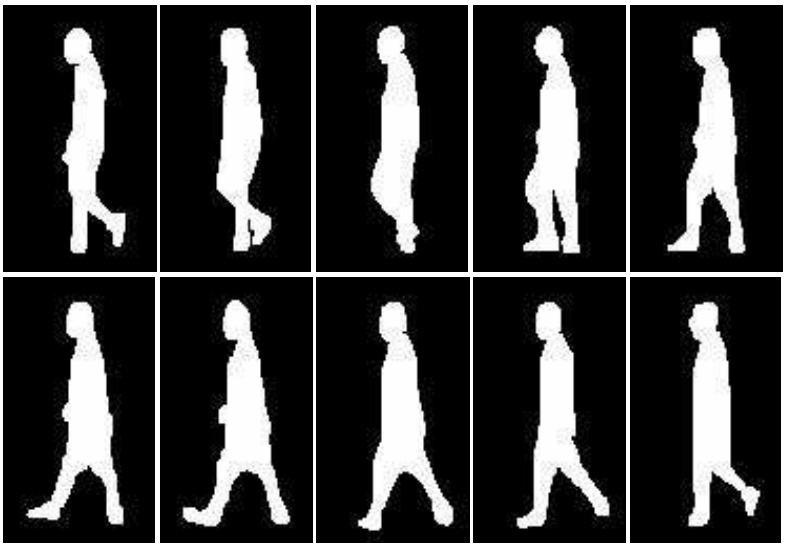

Figure 2.1: Sequence of shapes as a person walks frontoparallely

of shapes. They use the notion of shape average to differentiate global motion of a shape from the deformations of a shape. Maurel and Sapiro [104] propose a notion of dynamic averages for shape sequences using dynamic time warping for allignment. Vaswani et al. [158] used the dynamics of a configuration of interacting objects to perform activity classification. They apply the learned dynamics for the problem of detecting abnormal activities in a surveillance scenario. Recently, Liu and Ahuja [98] have proposed using autoregressive models on the Fourier descriptors for learning the dynamics of a 'dynamic shape'. They use this model for performing object recognition, synthesis and prediction.

2.1 Kendalls Shape Theory - Preliminaries

2.1.1 Definition of Shape

"Shape is all the geometric information that remains when location, scale and rotational effects are filtered out from the object" [43]. We use Kendall's statistical shape as the shape feature. [43] provides a description of the various tools in statistical shape analysis. Kendall's representation of shape describes the shape configuration of k landmark points in an m-dimensional space as a $k \times m$ matrix containing the coordinates of the landmarks. In our analysis we have a 2 dimensional space and therefore it is convenient to describe the shape vector as a k dimensional complex vector.

The binarized silhouette denoting the extent of the object in an image is obtained. A shape feature is extracted from this binarized silhouette. This feature vector must be invariant to translation and scaling since the objects identity should not depend on the distance of the object from the camera. So any feature vector that we obtain must be invariant to translation and scale. This yields the pre-shape of the object in each frame. Pre-shape is the geometric information that remains when location and scale effects are filtered out. Let the configuration of a set of k landmark points be given by a k-dimensional complex vector containing the position of the landmarks. Let us denote this configuration as X. Centered pre-shape is obtained by subtracting the mean from the configuration and then scaling to norm one. The centered pre-shape is given by

$$Z_c = \frac{CX}{\parallel CX \parallel}, \quad where \quad C = I_k - \frac{1}{k} 1_k 1_k^T, \tag{2.1}$$

where I_k is a k×k identity matrix and 1_k is a k dimensional vector of ones.

2.1.2 Distance between shapes

The pre-shape vector that is extracted by the method described above lies on a spherical manifold. Therefore a concept of distance between two shapes must include the non-Euclidean nature of the shape space. Several distance metrics have been defined in [43]. Consider two complex configurations X and Y with corresponding corresponding preshapes α and β. The full Procrustes distance between the configurations X and Y is defined as the Euclidean distance between the full Procrustes fit of α and β. Full Procrustes fit is chosen so as to minimize

$$d(Y, X) = \| \beta - \alpha s e^{j\theta} - (a + jb)1_k \|, \tag{2.2}$$

where s is a scale, θ is the rotation and $(a + jb)$ is the translation. Full Procrustes distance is the minimum Full Procrustes fit i.e.,

$$d_F(Y, X) = \inf_{s,\theta,a,b} d(Y, X). \tag{2.3}$$

We note that the preshapes are actually obtained after filtering out effects of translation and scale. Hence, the translation value that minimizes the full Procrustes fit is given by $(a + jb) = 0$, while the scale $s = |\alpha^* \beta|$ is very close to unity. The rotation angle θ that minimizes the Full Procrustes fit is given by $\theta = arg(|\alpha^* \beta|)$.

The partial Procrustes distance between configurations X and Y is obtained by matching their respective preshapes α and β as closely as possible over rotations, but not scale. So,

$$d_P(X, Y) = \inf_{\Gamma \epsilon SO(m)} \| \beta - \alpha\Gamma \| . \tag{2.4}$$

It is interesting to note that the optimal rotation θ is the same whether we compute the full Procrustes distance or the partial Procrustes distance. The Procrustes distance $\rho(X, Y)$ is the closest great circle distance between α and β on the preshape sphere. The minimization is done over all rotations. Thus ρ is the smallest

angle between complex vectors α and β over rotations of α and β. The three distance measures defined above are all trigonometrically related as

$$d_F(X, Y) = \sin \rho, \tag{2.5}$$

$$d_P(X, Y) = 2 \sin(\frac{\rho}{2}). \tag{2.6}$$

When the shapes are very close to each other there is very little difference between the various shape distances. In our work we have used the various shape distances to compare the similarity of two shape sequences and obtain recognition results using these similarity scores. Our experiments show that the choice of shape-distance does not alter recognition performance significantly for the problem of gait recognition since the shapes of a single individual lie very close to each other. We show the results corresponding to the partial Procrustes distance in all our plots.

2.1.3 The tangent space

The shape tangent space is a linearization of the spherical shape space around a particular pole. Usually the Procrustes mean shape of a set of similar shapes(Y_i) is chosen as the pole for the tangent space coordinates. The Procrustes mean shape(μ) is obtained by minimizing the sum of squares of full Procrustes distances from each shape Y_i to the mean shape, i.e.,

$$\mu = \arg \inf_{\mu} \Sigma d_F^2(Y_i, \mu). \tag{2.7}$$

The pre-shape formed by k points lie on a $k-1$ dimensional complex hypersphere of unit radius. If the various shapes in the data are close to each other then these points on the hypersphere will also lie close to each other. The Procrustes

mean of this dataset will also lie close to these points. Therefore the tangent space constructed with the Procrustes mean shape as the pole is an approximate linear space for this data. The Euclidean distance in this tangent space is a good approximation to the various Procrustes distances d_F, d_P and ρ in shape space in the vicinity of the pole. The advantage of the tangent space is that this space is Euclidean.

The Procrustes tangent coordinates of a preshape α is given by

$$v(\alpha, \mu) = \alpha\alpha^*\mu - \mu|\alpha^*\mu|^2. \tag{2.8}$$

where μ is the Procrustes mean shape of the data.

2.2 Comparison Of Shape Sequences

In this section we provide a method based on dynamic time warping to compute distances between shape sequences. We also provide methods based on autoregressive and autoregressive moving average models to learn the dynamics of these shape changes and use the distance measures between models as a measure of similarity between these shape sequences. The methods described here can be used generically for any landmark based description of shapes, not just to silhouettes.

2.2.1 Non-Parametric method for comparing shape sequences

Consider a situation where there are two shape sequences and we wish to compare how similar these two shape sequences are. We may not have any other specific information about these sequences and therefore any attempt at modeling these sequences is difficult. These shape sequences may be of differing length(number of frames) and therefore in order to compare these sequences we need to perform

time normalization(scaling). A linear time scaling would be inappropriate because in most scenarios this time scaling would be inherently non-linear. Dynamic time warping(DTW) which has been successfully used by the speech recognition [131] community is an ideal candidate for performing this non-linear time normalization. However, certain modifications to the original DTW are also necessary in order to account for the non-Euclidean structure of the shape space.

2.2.2 Dynamic time warping

Dynamic time warping (DTW) is a method for computing a non-linear time normalization between a template vector sequence and a test vector sequence. These two sequences could be of differing lengths. The algorithm which is based on dynamic programming computes the best non-linear time normalization of the test sequence in order to match the template sequence, by performing a search over the space of all allowed time normalizations. The space of all time normalizations allowed is cleverly constructed using certain temporal consistency constraints. We list the temporal consistency constraints that we have used in our implementation of the DTW below.

- End point constraints: The beginning and the end of each sequence is rigidly fixed. For example if the template sequence is of length N and the test sequence is of length M then only time normalizations that map the first frame of the template to the first frame of the test sequence and also map the Nth frame of the template sequence to the Mth frame of the test sequence are allowed.

- The warping function(mapping function between the test sequence time to the template sequence time) should be monotonically increasing. In other

words the sequence of 'events' in both the template and the test sequences should be the same.

- The warping function should be continuous.

Dynamic programming is used to efficiently compute the best warping function and the global warping error.

Pre-shape, as we have already discussed lies on a spherical manifold. The spherical nature of the shape-space must be taken into account in the implementation of the DTW algorithm. This implies that during the DTW computation the local distance measure used must take into account the non-Euclidean nature of the shape-space. Therefore, it is only meaningful to use the Procrustes shape distances described earlier. It is important to note that the Procrustes distance is not a distance metric since it is not commutative. Moreover, the nature of the definition of constraints make the DTW algorithm non-commutative even when we use a distance metric for the local feature error. If $A(t)$ and $B(t)$ are two shape sequences then, we define the distance between these two sequences $D(A(t), B(t))$ as

$$D(A(t), B(t)) = DTW(A(t), B(t)) + DTW(B(t), A(t)); \tag{2.9}$$

where $DTW(A(t), B(t)) = 1/T \sum_{t=1}^{T} d(A(f(t)), B(g(t)))$ (f and g being the optimal warping functions). Such a distance between shape sequences is commutative. The isolation property i.e., $D(A(t), B(t)) = 0$ iff $A(t) = B(t)$, is enforced by penalizing all non-diagonal transitions in the local error metric.

2.2.3 Parametric models for shape sequences

In several situations, it is very useful to model the shape deformations over time. If such a model could be learned either from the data or from the physics of the

actual scenario, then it would help significantly in problems such as identification and for synthesizing shape sequences. Liu and Ahuja [98] learn the nature of shape changes of a fire sequence. They also synthesize new sequences of fire using the model that they learned. This section describes work with very similar objectives. We describe both autoregressive(AR) and autoregressive and moving average(ARMA) models on tangent space projections of the shape. We describe methods to learn these models from sequences and compute distances between models in this parametric setting. Our approach for parametric modeling differs from that of [98] in two important ways. The shape feature on which we build parametric models preserves locality while the Fourier descriptors that they use is a global shape feature. Therefore our method can in principle capture the dynamics of shape sequences locally and is better suited for applications where different local neighborhoods of the shape exhibit different dynamics. We use parametric modeling for modeling human gait, a very specific example where different local neighborhoods(different parts of the body) exhibit different dynamics. Moreover, we also extend the parametric modeling from AR to the ARMA model. The advantage of the ARMA model is that it can be used to characterize systems with both poles and zeros while the AR model can be used to characterize systems with zeros only.

2.2.4 AR Model on tangent space

The AR model is a simple time-series model that has been used very successfully for prediction and modeling especially in speech. The probabilistic interpretation of the AR model is valid only when the space is Euclidean. Therefore, we build an AR model on the tangent space projections of the shape sequence. Once the AR

model is learned we can use this either for synthesis of a new shape sequence or for comparing shape sequences by computing distances between the model parameters.

The time series of the tangent space projections of the pre-shape vector of each shape is modeled as an AR process. Let, s_j, $j = 1, 2, ...M$ be the M such sequences of shapes. Let us denote the tangent space projection of the sequence of shape s_j by α_j. Now, the AR model on the tangent space projections is given by,

$$\underline{\alpha_j}(t) = A_j \underline{\alpha_j}(t-1) + w(t) \tag{2.10}$$

where, w is a zero mean white Gaussian noise process and A_j is the transition matrix corresponding to the j^th sequence. For convenience and simplicity A_j is assumed to be a diagonal matrix.

For all the sequences in the gallery, the transition matrices are obtained and stored. Given a probe sequence, the transition matrix for the probe sequence is computed. The distances between the corresponding transition matrices are added to obtain a measure of the distance between the models. If A and B (for $j = 1, 2, ...N$) represent the transition matrices for the two sequences, then the distance between the models is defined as $D(A, B)$

$$D(A, B) = ||A_j - B_j||_F, \tag{2.11}$$

where $||.||_F$ denotes the Frobenius norm. The model in the gallery that is closest to the model of the given probe is chosen as the correct identity.

2.2.5 ARMA Model

We pose the problem of learning the nature of a shape sequence as one of learning a dynamical model from shape observations. We also regard the problem of shape

sequence based recognition as one of computing the distances between the dynamical models thus learned. The dynamical model is a continuous state, discrete time model. Since the parameters of the models lie in a non-Euclidean space, the distance computations between the models is non-trivial. Let us assume that the time-series of tangent projections of shapes(about its mean as the pole) is given by $\alpha(t), t = 1, 2, , , , , \tau$. Then an ARMA model is defined as [23] [10]

$$\alpha(t) = Cx(t) + w(t); w(t) \sim N(0, R) \tag{2.12}$$

$$x(t+1) = Ax(t) + v(t); v(t) \sim N(0, Q). \tag{2.13}$$

Also, let the cross correlation between w and v be given by S. The parameters of the model are given by the transition matrix A and the state matrix C. We note that the choice of matrices A, C, R, Q, S is not unique. However, we can transform this model to the "innovation representation" [121] which is unique.

2.2.6 Learning the ARMA model

We use the tools from the system identification literature to estimate the model parameters.The estimation is closed form and therefore simple to implement. The algorithm is described in [121] and [144]. Given observations $\alpha(1), \alpha(2), ...\alpha(\tau)$, we have to learn the parameters of the innovation representation given by $\hat{A}, \hat{C}$ and $\hat{K}$($\hat{K}$:Kalman gain matrix of the innovation representation [121]). Note that in the innovation representation, the state covariance matrix $\lim_{t\to\infty} E[x(t)x^T(t)]$ is asymptotically diagonal. Let $[\alpha(1)\alpha(2)\alpha(3).....\alpha(\tau)] = U\Sigma V^T$ be the singular value decomposition of the data. Then

$$\hat{C}(\tau) = U \tag{2.14}$$

$$\hat{A} = \Sigma V^T D_1 V (V^T D_2 V)^{-1} \Sigma^{-1} \tag{2.15}$$

where $D_1 = [0\ 0; I_{\tau-1}\ 0]$ and $D_2 = [I_{\tau-1}\ 0; 0\ 0]$.

2.2.7 Distance between ARMA Models

Subspace angles [59] between two ARMA models are defined as the principal angles $(\theta_i, i = 1, 2, ...n)$ between the column spaces generated by the observability spaces of the two models extended with the observability matrices of the inverse models [31]. The subspace angles between two ARMA models ($[A_1, C_1, K_1]$ and $[A_2, C_2, K_2]$ can be computed by the method described in [31]. Using these subspace angles $\theta_i, i = 1, 2, ...n$, three distances, Martin distance(d_M), gap distance(d_g) and Frobenius distance(d_F) between the ARMA models are defined as follows:

$$d_M^2 = \ln \prod_{i=1}^{n} \frac{1}{\cos^2(\theta_i)}, \tag{2.16}$$

$$d_g = \sin \theta_{max}, \tag{2.17}$$

$$d_F^2 = 2 \sum_{i=1}^{n} \sin^2 \theta_i. \tag{2.18}$$

The various distance measures do not alter the results significantly. We show the results using the Frobenius distance(d_F^2).

2.3 Note on the limitations of Proposed Techniques

The parametric models AR and ARMA were both done on the tangent space of the shape manifold with the mean shape of the sequence being the pole of the tangent space. In problems like gait analysis, where the several shapes in the sequence lie close to each other, this would be sufficient. But to model sequences where the shapes vary drastically within a sequence, it might be necesssary to

develop tools to translate the tangent vectors appropriately so that modeling is performed on a tangent space that varies with time. Preliminary experiments in this direction indicate that performing such complex non-stationary modeling for a single activity like gait leads to over-fitting while for studying multiple activities this is significantly helpful.

The AR model for shape sequences due to its inherent simplicity might not be able to capture all the temporal structure present in activities such as gait. But, as is shown in [98], it can handle stochastic shape sequences with little or no spatial structure. In fact, [98] also used a similar AR model as a generative model for the synthesis of a fire boundary sequence. The ARMA model is better able to capture the structure in motion patterns such as gait since the "C" matrix encodes such structural details. The DTW algorithm can also handle such highly structured shape sequences such as gait, but is not directly interpretable as a generative model.

For the AR and ARMA models the shapes are initially projected to the tangent spaces of their respective mean shape. Models are fitted in these tangent spaces and their parameters are learnt. If the mean shapes for different sequences are different, then these parameters are modeling systems in two different subspaces. This fact must be borne in mind while computing distances between models. The ARMA model elegantly does this by invoking the theory of comparing models on different subspaces from system identification literature. Thus, it is able to handle modeling on different subspaces. (Note that the C matrix encodes the subspace and is used in the ARMA distance computation). The AR model does not account for modeling in different subspaces and therefore produces meaningful distance measures only when the two mean shapes are similar. The DTW method works

directly on the shape manifold and not on the tangent space. Therefore, the DTW is also general and does not suffer from the above-mentioned limitation of the AR model.

2.4 Experiments and Conclusions

We describe the various experiments we designed using the algorithms previously discussed in order to study gait-based human recognition. We also show an extension of the same analysis for the problem of activity recognition. The goals of the experiments were:

1. Show the efficacy of our algorithms in comparing shape sequences by applying it to the problem of automated gait recognition.

2. Study the role of shape and kinematics in automated gait recognition algorithms.

3. Make a similar study on the role of shape and kinematics for activity recognition.

Continuing our approach in [162] we use a purely shape based technique called the Stance Correlation to study the role of shape in automated gait recognition.

The algorithms for comparing shape sequences were applied on two standard databases. The USF database [129] consists of 71 people in the Gallery[1]. Various covariates like camera position, shoe type, surface and time were varied in a controlled manner to design a set of challenge experiments[2] [129]. The results are

[1]A more expanded version is available on which we haven't yet experimented.However we do not expect our conclusions to alter significantly.

[2]Challenge Experiments:Probes A-G in increasing order of difficulty.

evaluated using cumulative match scores[3](CMS) curves and the identification rate. The CMU database [32] consists of 25 people. Each of the 25 people perform four different activities(slow walk, fast walk, walking on an inclined surface and walking with a ball). For the CMU database we provide results for recognition both within an activity and across activities. We also provide some results on activity recognition on this dataset.

2.4.1 Feature Extraction

Given a binary image consisting of the silhouette of a person, we need to extract the shape from this binary image. This can be done either by uniform sampling along each row or by uniform arc-length sampling. In uniform sampling, landmark points are obtained by identifying the edges of the silhouette in each row of the image. In uniform arc length sampling, the silhouette is initially interpolated using critical landmark points. Uniform sampling on this interpolated silhouette provides us with the uniform arc-length sampling landmarks. Once the landmarks are obtained, the shape is extracted using the procedure described in 2.1. The procedure for obtaining shapes from the video sequence is graphically illustrated in Figure 2.2. Note that each frame of the video sequence maps to a point on the spherical(hyper-spherical) shape manifold.

2.4.2 Results on the USF Database

On the USF database we conducted experiments on recognition performance using these methods- Stance Correlation, DTW on shape space, Stance based AR(a slight modification of the AR model [162]) and ARMA model. Gait recognition

[3]Plot of percentage of recognition Vs rank.

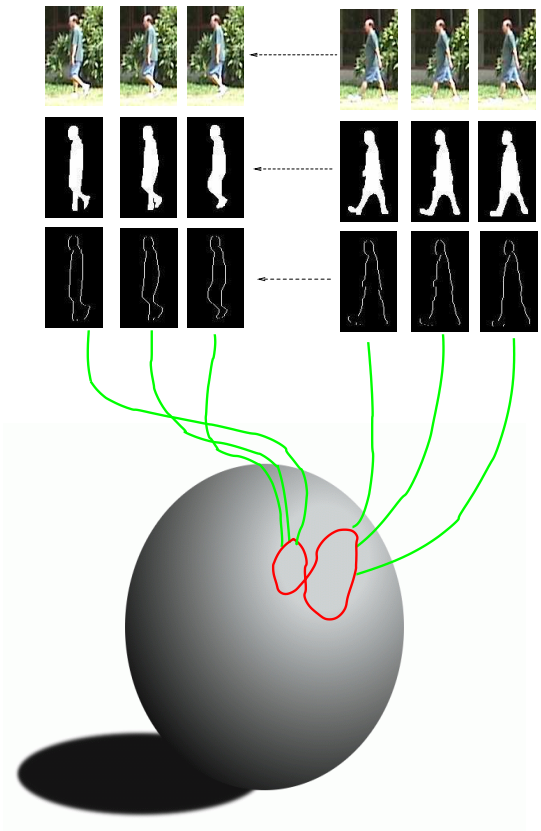

Figure 2.2: Graphical illustration of the sequence of shapes obtained during gait

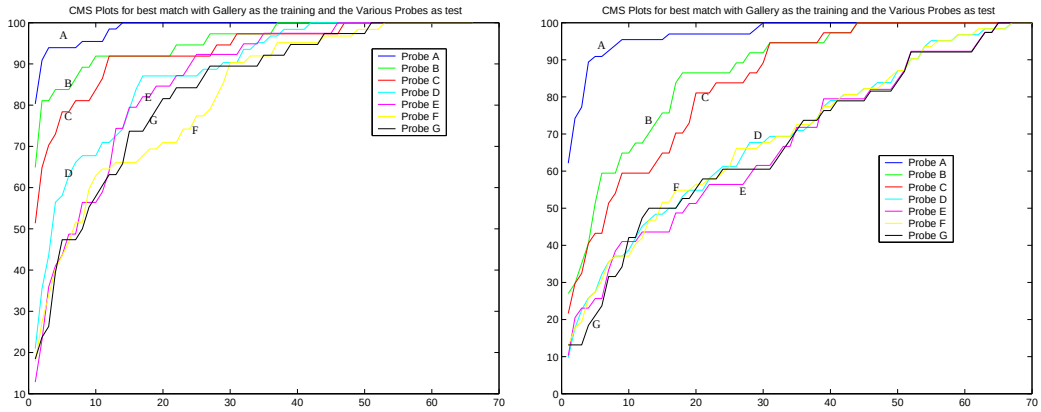

(a) (b)

Figure 2.3: Similarity matrix using(a)Dynamic Time Warping on shape space and (b)ARMA model on tangent space

experiments were designed for challenge experiments A-G. These experiments featured and tested the recognition performance against various covariates like camera angle, shoe type, surface change etc. Refer to [129] for a detailed description of the various experiments and the covariates in these experiments. Figure 2.3 shows the CMS curves for the challenge experiments A-G using the Dynamic time warping and the ARMA model. The recognition performance of the DTW based method is comparable to the state of art algorithms that have been tested on this data [85]. The performance of the ARMA model is lower since human gait is a very complex action and the ARMA model is unable to capture all these details.

In order to understand the significance of shape and kinematics in gait recognition, we ran the same experiments with other purely shape and purely dynamics based methods as described in [162]. Figure 2.4(a) shows the average CMS curves(average of the 7 Challenge experiments:Probes A-G) for the various shape and kinematics based methods.

The following conclusions are drawn from Figure 2.4(a):

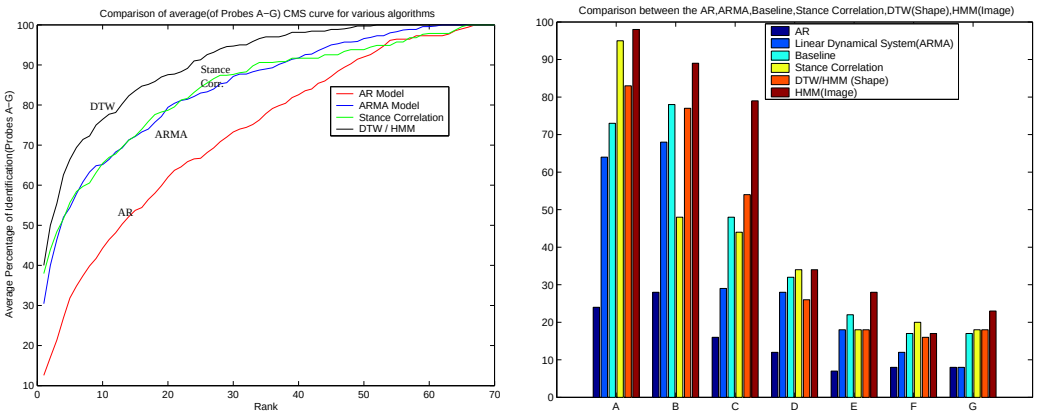

(a) (b)

Figure 2.4: (a)Average CMS curves(Percentage of Recognition Vs Rank) and (b)Bar Diagram comparing the identification rate

- The average CMS curve of the Stance Correlation method shows that shape without any kinematic cues provides recognition performance below baseline. The baseline algorithm is image correlation based and can be found in [129].
- The average CMS curve of the DTW method is better than that of Stance Correlation and close to baseline.
- The improvement in the average CMS curve in the DTW over that of the Stance Correlation method can be attributed to the presence of this implicit kinematics, because the algorithm tries to synchronize two warping paths.
- Both methods based on kinematics alone(Stance based AR and ARMA model) do not perform as well as the methods based on shape.
- The results support our belief that kinematics helps to boost recognition performance but is not sufficient as a stand-alone feature for person identification.
- The performance of the ARMA model is better than that of the Stance based AR model. This is because the observation matrix(C) encodes information about

the features in the image, in addition to the dynamics encoded in the transition matrix(A).

- Similar conclusions may be obtained by looking at the CMS curves for the 7 experiments(Probes A-G) separately. We have shown the average CMS curve for simplicity.

2.4.3 Results using Joint angles

In this section we describe experiments designed to verify the fact that our inference about the role of kinematics in gait recognition was not dependent on the feature that we chose for representation (Kendall's statistical shape). In order to test this, we performed some experiments on the actual physical parameters that are observable during gait i.e., the joint angles at the various joints of the human body. We used the manually segmented images provided in the USF dataset for these experiments. We inferred the angles (angle in the image plane) of eight joints (both shoulders, both Elbows, both Hips and both Knees) as the subjects walked frontoparallel to the camera. We used these angles (which are physically realizable parameters) as the features representing the kinematics of gait. We performed recognition experiments using the DTW directly on this feature. Figure 2.5(a) shows the CMS curves for three probes for which the manual segmented images were available. The recognition performance is comparable to purely kinematics based methods using our shape feature vector (refer to Figure 2.3(b)).

We also generated synthetic images of an individual walking using a truncated elliptic cone model for the human body and using the joint angles extracted from the manually segmented images. Figure 2.6 shows some sample images that were generated using this truncated elliptic cone model. We also performed recogni-

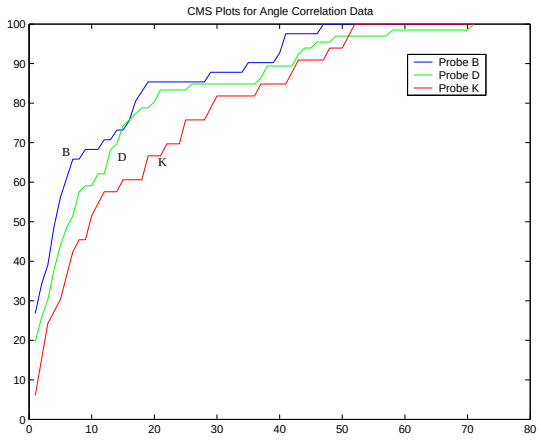

(a) DTW on joint angles

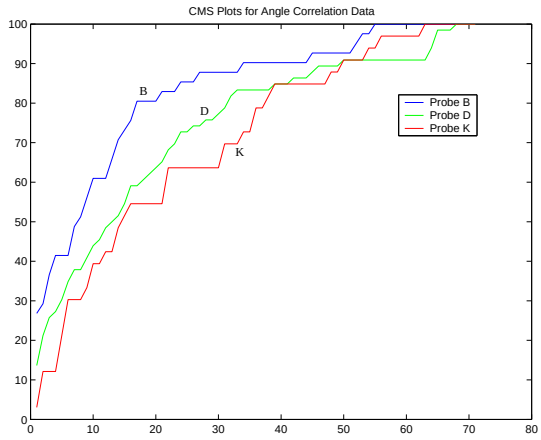

(b) Shape sequence DTW on simulated data

Figure 2.5: CMS curve using (a) DTW on joint angles and (b) Shape sequence DTW on simulated data

tion experiments on this simulated data using the DTW based shape sequence analysis method described in section 4.1. Figure 2.5(b) shows the CMS curves for this experiment. The results of these experiments are consistent with the experiments described earlier (2.3(b) and 2.5(a)), indicating that for the purposes of gait recognition, the amount of discriminability provided by the dynamics of the shape feature is similar to the discriminability provided by the dynamics of physical parameters like joint angles. This means that there is very little (if any) loss in using the dynamics of the shape feature instead of dynamics of the human body parts. Therefore, our inferences about the role of kinematics will most probably remain unaffected irrespective of the features used for representation.

2.4.4 Results on the CMU Dataset

The CMU dataset has 25 subjects performing four different activities- fast walk, slow walk, walking with a ball and walking on an inclined plane. We perform

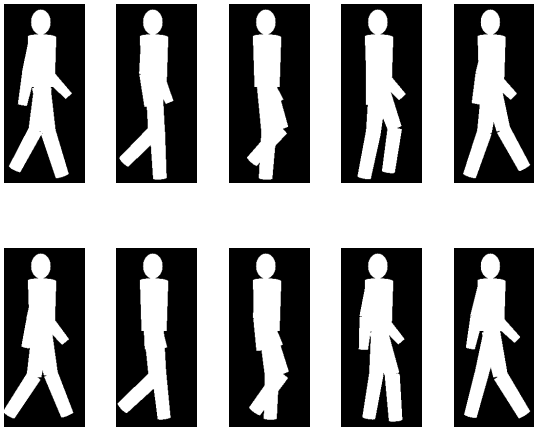

Figure 2.6: Sequence of silhouettes simulated using joint angles and truncated elliptic cone human body model

an experiment on the recognition performance(i.e., identification rate) using two methods - the Stance Correlation(pure shape) method and ARMA model. The results on the CMU dataset are shown in Table 1.

2.5 Conclusions and Future Work

We have proposed novel methods for comparing two stationary shape sequences and shown their applicability to problems like gait recognition and activity recognition. The non-parametric method, using DTW is applicable to situations where there is very little domain knowledge and therefore parametric modeling of shape sequences is difficult. We have also used parametric AR and ARMA models on the tangent space projections of a shape sequence. The ability of these methods to serve as pattern classifiers for sequences of shapes has been shown by applying them to the problem of gait and activity recognition. We are currently working on building complex parametric models that capture more details about the appearance and motion of objects and models that can handle non-stationary shape

Activity	Slow Walk	Fast Walk	Walk with Ball	Inclined plane
Slow Walk	100(100)	80(72)	48(64)	48
Fast Walk	84(75)	100(100)	48(60)	28
Walk with Ball	68(70)	48(50)	92(100)	12
Inclined plane	32	44	20	92

Table 2.1: Identification rates on the CMU Data: Numbers outside braces are obtained using Stance Correlation while those within the braces are obtained using the ARMA model.

sequences. We are also attempting to build models on the shape space instead of working with the tangent space projections. Moreover, our experiments on gait recognition lead us to make an interesting observation about the role of shape and kinematics in human movement analysis from video. The experiments on gait recognition indicate that body shape is a significantly more important cue than kinematics for automated recognition, but using the kinematics of human body improves the person identification capability of shape based recognition systems.

Chapter 3

Modeling Execution Rate Variations for Action Recognition

Pattern Recognition in videos is gaining momentum in recent years because of its applicability to several problems such as gait-based person identification, activity modeling and recognition, video-based face recognition etc. Pattern recognition in video streams is often a very challenging task because of the multitude of spatiotemporal changes that can occur in a video capturing the exact same event. Several algorithms and methods account for the spatial variations due to changes in lighting, pose and appearance of individual objects. Nevertheless, very little work has been done to account for the complex temporal variations that occur in videos. For example, in activity recognition, different instances of the same activity may consist of varying relative speeds at which the various actions are executed, in addition to other intra- and inter- person variabilities. Most existing algorithms for activity recognition are not very robust to intra- and inter-personal changes of the same activity, and are extremely sensitive to warping of the temporal axis due to variations in speed profile.

In this chapter, we study the variations due to execution rate in a systematic way. We model an action sequence as a composition of these two sources of variability - variability on the feature space and variability due to execution rate. By keeping the model on the feature space completely independent of the model on the space of execution rates, we are then able to exploit any of the above mentioned viewpoint invariant features in our method. Therefore, as more sophisticated features become available our model will be able to exploit the characteristics of those features while retaining the ability to deal with variations in execution rate. We explicitly model execution rates and derive a Baysian classification algorithm for action recognition. If the chosen features are viewpoint and anthropometry invariant, then the resulting algorithm becomes invariant to all the three significant modes of variations - viewpoint, anthropometry and execution rate. Moreover, since the model developed is general and not necessarily restricted to action recognition, we believe that similar models may be used for other applications which require rate-invariance.

Motivation: Consider the INRIA iXmas activity recognition dataset. Shown in Figure 3.1(L) is the distribution of the number of frames in different executions of the same activity for four distinct activities. Figure 3.1(L) clearly shows that for the same activity the rate of execution and consequently the number of frames during the execution varies significantly. Moreover, in most realistic scenarios this temporal warping might also be inherently non-linear making simple resampling methods ineffective. This implies that for uncontrolled scenarios the variations due to temporal warpings could be even more significant. Ignoring this temporal warping might lead to structural inconsistencies apart from providing poor recognition performance. The sequence of images shown in the first two rows of Figure

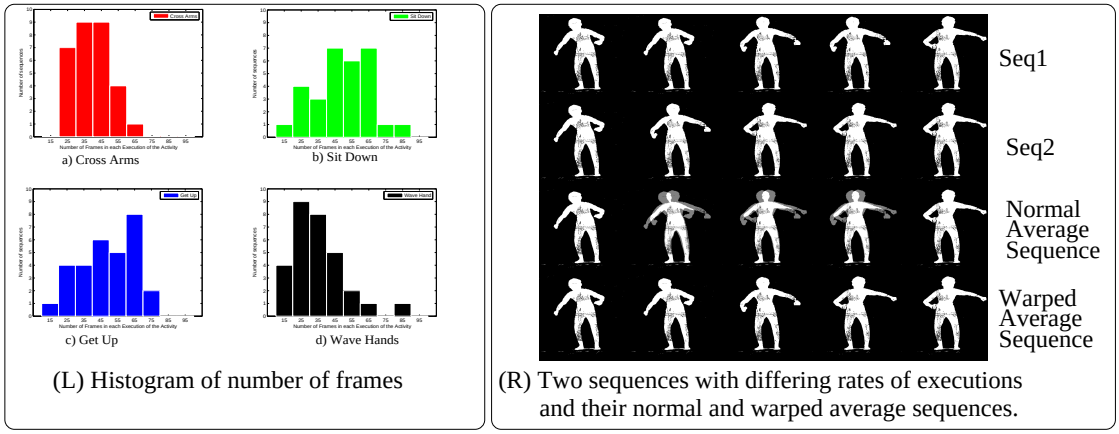

Figure 3.1: (L) Histogram of the number of frames in different executions of the same action in the INRIA iXmas dataset. The histograms for 4 different activities are shown. (a) Cross Arms (b) Sit Down (c) Get Up (d) Wave hands. (R) Row 1, Row 2: Two instances of the same activity. Row 3: A simple average sequence. Row 4:Average Sequence after accounting for time warps.

3.1(R) correspond to two different instances of the same individual performing the same activity. There is an obvious temporal warping between the two sequences. If this temporal warping is ignored, the distance between these two sequences will be large, leading to incorrect matching. Moreover, if we are looking for some statistical description of the activity like an average sequence, ignoring the temporal warping could lead to structural inconsistencies like the presence of four arms and two heads in the average sequence, shown in the third row of Figure 3.1(R). If we do account for temporal warping then such inconsistencies are avoided and the distance between the two sequences is rightly small. The fourth row shows a typical average sequence obtained by our method after accounting for time warping.

Why should the distribution of time-warps be class-specific? To answer this, let us consider the activity of 'jumping'. The subject may in principle speed up certain

portions of the activity relative to the others. But, during the actual moments the subject has no contact with the ground, the only external forces on the subject are those from gravitation and therefore, much as he/she might attempt to, he/she will not be able to change the execution speed during such times. There are thus physical, aesthetic and structural constraints that force different activities to have different warping functions. The constraints themselves vary with each activity and therefore the eventual probability distribution on warping functions varies from one activity to another.

3.0.1 Contributions of this chapter

- We propose a systematic generative model for activities that accounts for variations in speed profile of an activity. The model is composed of a *nominal activity trajectory* and a probability distribution on the *function space* of temporal warpings capturing the permissible activity-specific time warping transformations. We show how one can efficiently impose a Riemannian metric and perform exact and efficient statistical inference efficiently and correctly using the square-root density form of the time warp functions. We then derive a Bayesian solution for a rate-invariant classification of activities.

- We highlight a special case of this approach where we assume a uniform distribution on a convex subset of the warping functions and derive computationally efficient algorithms for learning and inference.

3.0.2 Outline of the chapter

We begin by providing a formal statement of the problem addressed in this chapter in Section 3.1. Section 3.2 describes the geometry of the space of time warps

and presents algorithms for computing geodesics, distances and prior probability distributions on this space. Section 3.3 describes how these tools may be used in order to learn the model parameters. Section 3.4 describes the special case of the model when the probability distribution on the space of time warpings is uniform. In Sections 3.5 and 3.6, we discuss how both the models developed earlier can be used in a Bayesian recognition framework in order to perform activity analysis, recognition and activity-based person identification. Finally, in Section 3.7, we present the conclusions and future research directions.

3.1 Problem Statement

Let $C_1, C_2, ..., C_M$ be M classes (in our case M different activity labels). Here we wish to tackle two tasks while accounting for time-warping - 1. Given several instances of an activity, we would like to build a model for that activity and 2. Given a test sequence, we would like to classify the sequence to one of the models in the database.

3.1.1 Feature for representation

Observations of an activity are typically obtained using video cameras and they are in the form of video frames. Raw videos are not appropriate features for representation. In principle, the feature chosen to describe the action units must have physical significance and one must be able to directly identify the relationship between the features extracted and the basic human pose. For the problem of activity recognition, 3-D joint angles would be ideal features. Unfortunately, estimating features like 3-D joint angles from images is extremely difficult and un-

reliable. So researchers have used several other features for describing the action units [133] [104] [137] [85]. Since the USF gait database consists of monocular video, we use the shape of the silhouette (along with the appropriate Procrustes distance) as a feature [162] for the gait-based person identification experiments. The INRIA iXmas dataset contains synchronized videos from multiple views and therefore allows us to compute and use the 3D Fourier based shape features described in [170]. We refer the interested reader to [43] [162] and [170] for details about the shape feature and the 3D circular FFT feature respectively.

For now let us assume that for each frame of the video, an appropriate feature has been extracted and that the video data has now been converted into a feature sequence given by $f^1, f^2, ...$, for frames $1, 2, ...$ respectively. We will use $\mathcal{F}$ to denote the feature space associated with the chosen feature.

3.1.2 Model for warping functions

Let γ be a diffeomorphism (A diffeomorphism is a smooth, invertible function with a smooth inverse.) from $[0, 1]$ to itself with $\gamma(0) = 0$ and $\gamma(1) = 1$. Also, let $\mathbf{\Gamma}$ be the set of all such functions. We will use elements of $\mathbf{\Gamma}$ to denote time warping functions. Our model for an activity consists of an average activity sequence given by $a : [0, 1] \rightarrow \mathcal{F}$, a parameterized trajectory on the feature space. Any time-warped realization of this activity is then obtained using:

$$r(t) = a(\gamma(t)), \quad \gamma \in \mathbf{\Gamma} \ . \tag{3.1}$$

We note in passing that $\mathbf{\Gamma}$ is a group with composition as the group operation and the function $\gamma(s) = s$ as the identity element. Equation 3.1 actually defines an action of $\mathbf{\Gamma}$ on $\mathcal{F}^{[0,1]}$, the space of all continuous activities. In our model, the variability associated with γ in each class will be modeled using a distribution P_γ

on $\mathbf{\Gamma}$. For the convenience of analysis and computation (refer Section 3.2), we prefer to work with $\psi = +\sqrt{\dot{\gamma}}$ instead of γ directly. There is a bijection between γ and ψ and the probability models on ψ directly relate to equivalent models on γ. Thus, we will introduce probability distributions P_ψ on the set of all ψs, for each activity class.

The parameters of this model are $a(t)$, the nominal activity trajectory, and P_ψ, the probability distribution on square-root representations of time warping functions. In general, the nominal activity trajectory $a(t)$ can also be chosen to be random. But, here, we restrict our analysis to cases where, the nominal activity trajectory $a(t)$ is deterministic but unknown. We will consider parametric forms of densities for P_ψ and reduce the problem of learning P_ψ to one of learning the parameters of the distribution P_ψ. In particular, we highlight (in Section 3.4) a special-case of a uniform distribution on the space of time warpings (called 'function space of an activity'). This particular special-case appeared as a preliminary conference paper [159].

Physical Significance of the Model: *The nominal activity trajectory*, $a(t)$ and the probability distribution on the space of time-warps, P_ψ together capture all the possible realizations of the activity and provide the description of the activity under different variabilities. In general, the nominal activity trajectories of two different activities will be vastly different. The nominal activity trajectory for 'walking' would consist of key postures like heel-strike, toe-off, mid-stance etc., while that of 'sit down' would consist of the following actions - bend knee, lower body, settle on chair and rest back on backrest. The distribution of activity-specific temporal warpings P_ψ, represents the space of all permissible time-warping transformations for each activity. By learning this space, we are able to 'interpo-

late' appropriately between training sequences. Suppose there is a test sequence that is within this space, but was not a part of the training sequences. Most template sequence based recognition techniques tend to misclassify such test sequences. Learning the function space of an activity provides our algorithm with the generalization power necessary to correctly classify such test sequences. Moreover, by learning this warping space formally, in a class specific manner, we also obtain better discriminative power than other heuristic techniques for handling time-warping. The model M=$\{a, P_\psi\}$ represents a *function space* of activities whose elements are composed of functions $a(\gamma(t)),\ \forall\ \gamma \in \mathbf{\Gamma}$.

3.1.3 Problems

Here, we state informal descriptions of the various problems we wish to tackle.

The Learning Problem

Given N labeled realizations $r_1, r_2, r_3, ...r_N$, of an activity, we would like to learn the model for this activity. This is equivalent to learning the nominal activity trajectory $a(t)$ and the distribution on the warping parameters given by P_ψ.

The Classification Problem

Suppose we have models for M different activities $\{a^i, P^i_\psi\}_{i=1}^M$. Given a test sequence $r(t)$, we would like to classify this test sequence as belonging to one of the M models.

Clustering Problem

Given several realizations from K different activities with no class labeling, we would like to cluster these sequences into K distinct clusters such that sequences within the same cluster are maximally similar while sequences in different clusters are dissimilar. Moreover, unlike traditional clustering algorithms this similarity is invariant to changes in exectution rate of the action since the model for each cluster is built to be rate-invariant.

3.2 Differential geometric tools on the space of time-warping functions

The model for a random observation of an activity class consists of $a(\gamma(t))$, where a is the average of that class and γ is a warping function. In order to classify activities at variable execution rates, we need to analyze the warping functions as random functions. However, the space of warping functions is not a vector space and that rules out the use of classical functional analysis for this task. One alternative is to utilize the differential geometry of this space, impose a Riemannian structure on it, and use appropriate tools to perform calculus and statistics of warping functions. In particular, we can compute distances between warping functions, estimate sample means for given warping functions, and impose parametric and non-parametric probability distributions on the space of warping functions.

The next question is: What Riemannian structure on the space of warping functions is suitable and convenient for activity recognition? The Fisher-Rao metric is often used for analyzing probability density functions. (The Cramer-Rao lower bound on estimation of parameters is derived using this metric.) One major

reason for its popularity is that it is invariant to arbitrary warpings of the functions involved. In other words, under this metric the distance between any two warping functions $\gamma_1(t)$ and $\gamma_2(t)$ is same as that between $\gamma_1(\gamma(t))$ and $\gamma_2(\gamma(t))$ for any arbitrary warping function $\gamma(t)$. This point is important in activity recognition because, as we will point out in Section 3.3.4, the representation of an activity model is not unique, i.e. there is no canonical choice of γ for representing activity models. The choice of Fisher-Rao metric implies that the resulting distances are same irrespective of the baseline time axis chosen to represent activity models.

The Fisher-Rao metric, when applied to different mathematical representations of γ, i.e. γ, $\dot{\gamma}$, $\log \dot{\gamma}$, or $\sqrt{\dot{\gamma}}$, takes different forms. Interestingly, in the case of $\psi \equiv \sqrt{\dot{\gamma}}$, this metric simplifies to the familiar and convenient $\mathbb{L}^2$ metric [9, 147]. Furthermore, the space of all warping functions, represented by their square-root density forms, under the Fisher-Rao metric, becomes a unit sphere. This is because

$$\|\psi\|^2 = \int_0^1 |\psi(t)|^2 dt = \int_0^1 |\dot{\gamma}(t)| dt = \gamma(1) - \gamma(0) = 1 \ .$$

For these two reasons – invariance to arbitrary time scalings and the spherical nature of the resulting space, we choose the square-root density form to represent and analyze variability associated with the warping functions.

Let the space of all square-root density forms be given by

$$\mathbf{\Psi} = \{\psi : [0,1] \to \mathbb{R} | \psi \geq 0, \int_0^1 \psi^2(t) dt = 1\} \ . \tag{3.2}$$

This is the positive orthant of a unit hypersphere in the Hilbert space of all square-integrable functions on $[0, 1]$. Let $T_\psi(\mathbf{\Psi})$ be the tangent space to $\mathbf{\Psi}$ at any given point ψ. Then, for any v_1 and v_2 in $T_\psi(\mathbf{\Psi})$, the Fisher-Rao metric is given by

$$\langle v_1, v_2 \rangle = \int_0^1 v_1(t) v_2(t) dt. \tag{3.3}$$

Since $\mathbf{\Psi}$ is a sphere, its geometry is well known and we can directly use known expressions for tools such as geodesics, exponential maps, and inverse exponential maps on $\mathbf{\Psi}$. Consequently, the algorithms for computing sample statistics, defining probability density functions, and generating inferences also become straightforward.

We begin by describing some elements of differential geometry of $\mathbf{\Psi}$.

3.2.1 Geometry of $\mathbf{\Psi}$

One way to quantify the differences between two warping functions is to compute the distance between their corresponding representations in $\mathbf{\Psi}$. This distance is given by the length of a geodesic, the shortest path connecting those two points in $\mathbf{\Psi}$. We know that the geodesics on a sphere are the great circles and the geodesic distance is simply the length of the shorter arc connecting the two points on a great circle. Given two warping functions γ_1 and γ_2, and their square-root density forms, ψ_1 and ψ_2 in $\mathbf{\Psi}$, the geodesic distance between them on $\mathbf{\Psi}$ is given by

$$d(\psi_1, \psi_2) = \cos^{-1}(\langle \psi_1, \psi_2 \rangle), \tag{3.4}$$

where $\langle \psi_1, \psi_2 \rangle = \int_0^1 \psi_1(t)\psi_2(t)dt$.

The geodesic path itself can also be computed rather simply. Take the radial projection of the chord joining points ψ_1 and ψ_2 onto the unit sphere results in the geodesic. The chord joining ψ_1 and ψ_2 is given by $(1-s)\psi_1 + s\psi_2$ where s is the parameter that identifies various points on this chord. The radial distance of a point on this chord is given by $s^2 + (1-s)^2 + 2s(1-s)(\langle \psi_1, \psi_2 \rangle)$. Therefore, we can analytically write the geodesic connecting ψ_1 and ψ_2 as: $X : [0,1] \to \mathbf{\Psi}$,

$$X(s) = \frac{(1-s)\psi_1 + s\psi_2}{s^2 + (1-s)^2 + 2s(1-s)(\langle \psi_1, \psi_2 \rangle)},$$

such that $X(0) = \psi_1$ and $X(1) = \psi_2$. Another way to specify a geodesic path in $\mathbf{\Psi}$ is by giving a starting point $\psi \in \mathbf{\Psi}$ and a starting direction $v \in T_\psi(\mathbf{\Psi})$:

$$X(s) = \cos(s\|v\|)\psi + \sin(s\|v\|)\frac{v}{\|v\|} \ , \tag{3.5}$$

where $\|v\| = \sqrt{\int_0^1 v(t)^2 dt}$.

One use of geodesics is to define and compute the exponential map from $T_{\psi_1}(\psi)$ to ψ. It is simply the value reached at $s = 1$ by a geodesic that starts from ψ in the direction v and moves at a constant speed. We can evaluate the exponential map using:

$$exp_\psi(v) = \cos(\|v\|)\psi + \sin(\|v\|)\frac{v}{\|v\|}. \tag{3.6}$$

Similarly the inverse of the exponential map $exp_{\psi_1}^{-1}(\psi_2) = v \in T_{\psi_1}(\psi)$ can also be computed analytically using

$$u = \psi_2 - \langle \psi_2, \psi_1 \rangle \psi_1 \tag{3.7}$$

$$v = \frac{u \cos^{-1}(\langle \psi_1, \psi_2 \rangle)}{\sqrt{\langle u, u \rangle}}. \tag{3.8}$$

3.2.2 Statistical Analysis on $\mathbf{\Psi}$

With the geometry of $\mathbf{\Psi}$ as specified above, let us derive some tools for statistical analysis of data. Given a number of observed warping functions, we will estimate the sample mean and covariance, use these estimates to define a "wrapped-Gaussian" density function and derive Bayesian classification algorithms using these distributions as priors.

To compute the sample means of elements of $\mathbf{\Psi}$, we will use the notion of Karcher mean [86] that has been used frequently for defining means on nonlinear manifolds. Suppose, we have n different square-root density forms, given by

$\psi_1, \psi_2, ...\psi_n$. Then, their Karcher mean $\bar{\psi}$ is defined as the element that minimizes the sum of squares of geodesic distances:

$$\bar{\psi} = \arg\min_{\psi \in \mathbf{\Psi}} \sum_{i=1}^{n} d(\psi, \psi_i)^2) \tag{3.9}$$

where, d is the geodesic distance defined in (3.4). Note that the Karcher mean may not be unique and can instead be a set of elements. A commonly used approach for finding a Karcher mean is to use the gradients and this is where the exponential map and its inverse are needed. The iterative update to the current value of mean is given by:

$$\bar{\psi} \rightarrow exp_{\bar{\psi}}(\epsilon v), \quad \text{where} \;\; v = \frac{1}{n} \sum_{i=1}^{n} exp_{\bar{\psi}}^{-1}(\psi_i) \tag{3.10}$$

and where ϵ is usually 0.5. The next step is to define and compute a sample covariance for the observed ψs. The key idea here is to use the fact that the tangent space $T_{\bar{\psi}}(\mathbf{\Psi})$ is a vector space. Using a finite-dimensional approximation, say $V \subset T_{\bar{\psi}}(\mathbf{\Psi})$, we can use the classical multivariate calculus for this purpose. In practice, we obtain a natural restriction when v is observed at a finite number, say T, of times leading to an observation $\{v(t_i)|i = 1, 2, \ldots, T\}$. With a slight abuse of notation, we will denote this vector by $v \in \mathbb{R}^T$. The resulting sample covariance matrix is given by: $\bar{\Sigma} = \frac{1}{n-1} \sum_{i=1}^{n} v_i v_i^T$, where each v_i is a T-dimensional sample of the function $exp_{\bar{\psi}}^{-1}\psi_i$. Note that by definition, the mean of v_is should be zero. In cases where the number of samples n is smaller than T, one can apply an additional dimension-reduction tool to work on a smaller space. For instance, we can use the singular value decomposition (SVD) of the sample covariance matrix $\bar{\Sigma}$ and retain only the top m significant singular values and the corresponding singular vectors. In such cases, the covariance matrix is indirectly stored using $\lambda_1, \lambda_2, ...\lambda_m$ singular values and their corresponding singular vectors $u_1, u_2, ...u_m$.

Next, we define a "wrapped-Gaussian" probability density on $\mathbf{\Psi}$. We say

"wrapped-Gaussian" because $\mathbf{\Psi}$ is a non-Euclidean space and it is not possible to define a Gaussian density here. We follow the tangent PCA (TPCA) approach [148] for defining probability densities on nonlinear manifolds. In this approach, one defines a Gaussian probability density on a tangent space of the manifold and then projects it onto the manifold using the exponential map. However, in our case we will need only the samples from the eventual density function and the explicit functional form of that projected density is not needed. In fact, we will apply one more transformation in taking the samples on $\mathbf{\Psi}$ to obtain samples on $\mathbf{\Gamma}$. For a mean μ and covariance Σ, we can define a normal density function $N(v|\mu, \Sigma)$ on the elements of $V \subset T_\mu(\mathbf{\Psi})$. In case the data is available in the form of prior samples, we can use the sample means and covariances to define this density on the space V. The exponential map: $\exp_{\bar{\psi}} : T_{\bar{\psi}}(\mathbf{\Psi}) \rightarrow \mathbf{\Psi}$ maps this density to the spherical space of square-root forms, and the mapping $\psi \mapsto \gamma(t) = \int_0^t |\psi(\tau)|^2 d\tau$ takes it further to the space of warping functions. The exponential map results in wrapping the Gaussian density on the tangent space onto the sphere and therefore the name *wrapped-Gaussian*. We will denote the resulting densities on $\mathbf{\Psi}$ and Γ by P_ψ and P_γ, respectively.

For a Bayesian classification of activities, as described later in this paper, we will need to estimate the posterior probability of different classes given the observed data. In this calculation, the warping function is considered a nuisance variable that needs to be integrated out. Using a Monte Carlo approach, we will generate samples from the prior on γ and use those samples to approximate the nuisance integral. Thus, we have a need to generate samples from the class-specific priors P_γ on Γ. This, in turn, requires sampling from the probability density P_ψ, which is accomplished as follows. Let $\bar{\psi}$ and $\bar{\Sigma}$ be the sample mean and the sample

covariance of the square-root forms observed in a particular class. Assume that the covariance is stored in the form of m singular values λ_is and corresponding singular vectors u_is. In such cases, a random sample from the model P_ψ is given as

$$\psi \sim exp_{\bar{\psi}}(v) \qquad \text{where} \quad v \sim \sum_{i=1}^{m} z_i \sqrt{\lambda_i} u_i \quad \text{and} \quad z_i \sim N(0,1) \tag{3.11}$$

This random sample can then be converted into a warping function using the partial integration $\psi \mapsto \gamma$ such that $\gamma(t) = \int_0^t |\psi(\tau)|^2 d\tau$.

Toy Example Consider the toy example shown in Figure 3.2. Figure 3.2(a) shows 30 sample time-warping functions from each of three different classes (color coded). The corresponding square-root density forms are shown in 3.2(b). For each class using the samples of the square-root density forms we can compute the Karcher mean and the covariance. The Karcher means are shown in 3.2(d). The mean time-warping functions for each class obtained by partially integrating the Karcher means are shown in 3.2(c). The model for each class of time-warping functions is encoded in the form of the corresponding Karcher means and covariances. Now one can generate random samples from this model as described above. Shown in 3.2(f) are sample square-root density forms generated using the model parameters for each class (i.e., the Karcher mean and covariances). As before the corresponding time-warping functions maybe computed via partial integration and are shown in 3.2(e).

3.2.3 Global Speed of activity

We have restricted our attention to time-warping functions from $[0, 1]$ to itself, i.e the functions that do not contract or dilate the full duration of the activity. We claim that this is not restrictive, since any other time-warping transformation can

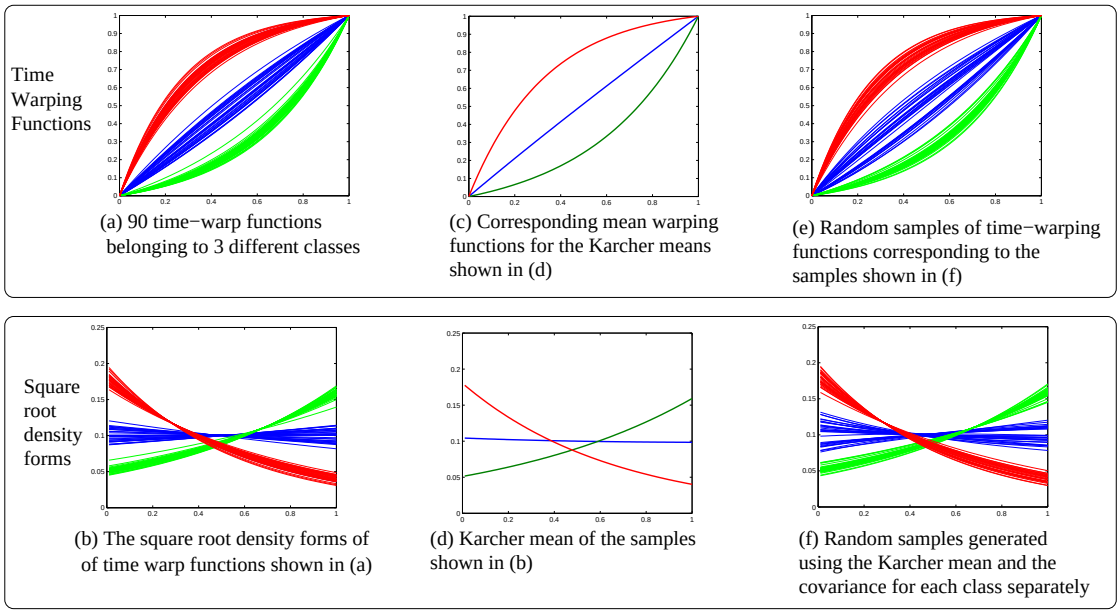

Figure 3.2: Figure is Color coded - Each color represents a different class (a) Random samples of time-warping functions belonging to 3 different classes (color coded) (b) Corresponding samples of square-root density forms (c) Mean time-warping function for each class computed by partial integration of the class-specific Karcher mean (d) Class specific Karcher mean computed using the samples shown in (b) (e) Random samples generated from the stored model (f) Random samples of ψ generated from the stored Karcher means and covariance.

be decomposed into two parts: a global linear scaling of the temporal axis and the non-linear time-warping functions that we have addressed so far. The effect of such a linear global temporal scaling is identical to the effect of changing the rate of sampling.

Let $a(t)$, for $0 \leq t \leq T_a$, be a vector valued function of time. Let $b(t)$, for $0 \leq t \leq T_b$, be a time-warped version of $a(t)$, with the warping function given by $w(t)$, i.e., $b(t) = a(w(t))$, $w(t) : [0, T_b] \rightarrow [0, T_a]$. Now $w(t)$ can be decomposed as $w(t) = T_a\gamma(t/T_b)$ where $\gamma : [0, 1] \rightarrow [0, 1]$ i.e., a global linear dilation (or contraction) and a non-linear warping γ. Without loss of generality we will use the word time-warping transformation to synonymously denote the non-linear time warping function given by γ. In all our experiments we have first identified the global temporal scaling factor by identifying the start and stop instants of each activity. The identification of the start and stop instants of each activity is also done automatically by template matching. Once the global temporal scaling factor is found, each realization of the activity is temporally dilated or contracted linearly so that the total duration of the activity is a constant for all realizations of the activity.

3.3 Learning and Classification Algorithms

Given N realizations $r_1, r_2, r_3, ...r_N$, of an activity, we need to learn the parameters of the model for this activity. This amounts to learning the nominal activity trajectory $a(t)$ and the probability distribution P_ψ.

3.3.1 Estimating P_ψ given $a(t)$

Let us assume that the nominal activity trajectory $a(t)$ is known. Now we need to estimate the parameters of the warping distribution which is given by P_ψ. In order to learn P_ψ, we first warp each of the observed realizations of the activity to the known nominal activity trajectory given by $a(t)$. This warping can be performed using the DTW algorithm. The DTW algorithm provides us with corresponding warping functions $\gamma_i(t)$ such that $\int_0^1 \|r_i(t) - a(\gamma_i(t))\|^2 dt$ is minimized. Then, we can compute ψ_is using $\psi_i = \sqrt{\dot{\gamma}_i}$.

Now, we have several samples $\psi_1, \psi_2, ...$ to estimate the distribution P_ψ. Assuming a "wrapped-Gaussian" distribution on $\mathbf{\Psi}$, this amounts to estimating the sample mean and the sample covariance of the observed ψ_is. As described in Section3.2.2, we can define and compute the Karcher mean of given ψ_is using the exponential and the inverse exponential maps. The covariance is obtained similarly by restricting to a T-dimensional approximation V of the vector space $T_{\bar{\psi}}(\mathbf{\Psi})$. Using SVD of observations in V, one ends up with the singular values $\lambda_1, \lambda_2, ...\lambda_m$ and their corresponding singular vectors $u_1, u_2, ...u_m$.

Thus, given the nominal activity trajectory $a(t)$, we can estimate the parameters of the warping distribution P_ψ, namely its Karcher mean $\bar{\psi}_K$ and its covariance stored indirectly using m singular values $\lambda_1, \lambda_2, ...\lambda_m$ and corresponding singular vectors $u_1, u_2, ...u_m$.

3.3.2 Estimating $a(t)$ assuming known warping functions

For the given observations $r_1, r_2, \ldots,$ of an activity, assume that the corresponding warping functions $\gamma_1, \gamma_2, \ldots,$ are also given. Then, we can estimate the nominal

or average activity trajectory $a(t)$ using

$$\bar{a}(t) = \frac{1}{N}\sum_{i=1}^{N} r_i(\gamma_i^{-1}(t)) \tag{3.12}$$

3.3.3 Iteratively estimating $a(t)$ and P_ψ

Given N realizations $r_1, r_2, r_3, ...r_N$, of the same activity, we would like to learn the parameters of the model for this activity. We do this by iteratively estimating P_ψ and refining our estimate of the nominal activity trajectory $\bar{a}(t)$ using the steps described in the previous two sections. We first initialize the nominal activity trajectory to one of the realizations say $a_{init}(t) = r_1(t)$. Then we estimate P_ψ using the method described in Section 3.3.1. We then refine the estimate of the nominal activity trajectory using the method described in Section 3.3.2. These two steps are iterated till convergence. In practice, we find that the iterations converge very quickly (within 4 or 5 iterations).

3.3.4 Uniqueness of the Model parameters

The model parameters given by $a(t)$ and $P_\psi \approx \{\bar{\psi_K}, \Sigma_\psi\}$ are not unique. Two different sets of model parameters $M_1 = \{a_1(t), P_{\psi_1}\}$ and $M_2 = \{a_2(t), P_{\psi_2}\}$, could lead to the same distribution on the observation space. That is, the two models may lead to the same distribution on the space of all activity realizations. This could happen if the corresponding nominal activity trajectory and the distribution on the space of warping transformations are related as

$$a_2(t) = a_1(\gamma(t)) \qquad \bar{\psi_1} = \sqrt{\dot{\bar{\gamma}_1}} \qquad \bar{\psi_2} = \sqrt{\dot{\bar{\gamma}_2}} \qquad \bar{\gamma_2}(t) = \bar{\gamma_1}(\bar{\gamma}^{-1}(t)) \qquad \Sigma_2 = \Sigma_1 \tag{3.13}$$

When the conditions listed in (3.13) are satisfied, we notice that $a_2(\bar{\gamma}_2(t)) = a_1(\bar{\gamma}_1(t))$, i.e., the mode of the activity trajectories is the same for both models.

Moreover, since the covariance matrices for the two models are identical ($\Sigma_1 = \Sigma_2$), this means that samples for either of these models will have identical distributions and would therefore be indistinguishable. In practice this means that there is an equivalence class of models such that any two models from the same equivalence class are indistinguishable. The conditions for belonging to the same equivalence class are those stated in (3.13). While performing classification and inference based on these model parameters it becomes essential to maintain uniqueness of model parameters. Therefore, once we learn the model parameters we always choose a single canonical representation for each equivalence class. Note that the choice of this canonical representation does not affect the performance of the algorithm at all as long as this choice is consistent. We choose the model with $\bar{\gamma}_K(t) = t$, such that the Karcher mean of the warping distribution corresponds to simple linear warping and the covariance matrix of the warping transformations encodes all the non-linearities in the warping distributions. The canonical model parameters are unique and can be directly used for classification and inference.

3.3.5 Generating activity samples from the model

The model for an activity is given by the nominal activity trajectory $a(t)$ and the distribution on warping transformations given by P_ψ. We can use this model to generate random samples from the model. We first generate random samples $\psi_1, \psi_2, ...\psi_M$ from the warping distribution P_ψ as described in Section 3.2.2. The corresponding time warp for each ψ is computed. Let $\gamma_1, \gamma_2, ...\gamma_M$ be the corresponding time warps. Then realizations from the model may be drawn as

$$r_j(t) = a(\gamma_j(t)) + w(t) \qquad \text{where} \qquad w \backsim N(0, \Sigma). \tag{3.14}$$

3.3.6 Classification Algorithm

Let us assume that we have K different models $M_1, M_2, ...M_K$ given by their appropriate nominal activity trajectories $a_1, a_2, ...a_K$ and corresponding P_ψ given by $P_\psi^1, P_\psi^2, ..., P_\psi^K$. Given a test sequence $r(t)$, we would like to classify $r(t)$ to one of the K possible classes. This classification task can be accomplished using MAP estimation, i.e.,

$$ID = \arg \max_{i=1,2,..K} P(M_i|r) = \arg_{i=1,2,..K} \max P(r|M_i)P(M_i). \tag{3.15}$$

The likelihood $P(r|M_i)$ can be computed as,

$$P(r|M_i) = \int_\psi P(r|M_i, \psi)P(\psi|M_i)d\psi \qquad \text{where} \qquad P(\psi|M_i) = P_\psi^i. \tag{3.16}$$

This integral can be estimated using Monte Carlo sampling methods. We draw N samples from the model M_i as described in Section 3.3.5. Using these samples we estimate the likelihood $P(r|M_i)$ as

$$P(r|M_i) = \frac{1}{N} \sum_{j=1}^{j=N} P(r|a_i, \psi_j) \qquad \text{where} \qquad \psi_j \backsim P(\psi) = P_\psi^i \tag{3.17}$$

In order to compute the summation described above, we need a model for computing the conditional likelihood $P(r|M_i, \psi_j)$. The conditional warp probability is inversely proportional to the distance between the warped nominal activity trajectory and the test sequence, i.e.,

$$P(r|M_i, \psi_j) = e^{-\alpha D(r, a_i(\gamma_j))} \qquad \text{where } D(r, a_i(\gamma_j)) = \int_0^1 (r(t) - a_i(\gamma_j(t)))^2 dt \tag{3.18}$$

and α is a suitably chosen constant. As the number of samples N increases the accuracy of the approximation improves. One can also improve the accuracy of the approximation by performing importance sampling [38]. Let us assume that

the proposal distribution from which the samples of the ψ are drawn is given by $G(\psi)$. Then we draw N samples of ψ from G and the integral is approximated as

$$P(r|M_i) = \frac{1}{N}\sum_{j=1}^{j=N} P(r|M_i,\psi_j)\frac{P(\psi_j|M_i)}{G(\psi_j)} \qquad \text{where} \qquad \psi_j \backsim G(\psi). \tag{3.19}$$

In practice, using importance sampling significantly improves the accuracy of the approximation when using a finite number of samples. The effectiveness of the importance sampling also critically depends upon the proposal distribution. The proposal distribution or the importance distribution should ideally be as close to the posterior distribution we wish to approximate. In practice, we first estimate the mode of this posterior by computing the best warping transformation between the nominal activity trajectory of the model ($a_i(t)$) and the test sequence ($r(t)$). We set the mean of the importance distribution to be this warping transformation while letting the covariance of the importance distribution to be the same as the covariance of the model. We have experimentally found that this choice of importance distribution enables us to effectively approximate the integrals using Monte Carlo methods with a reasonable number of random samples.

3.4 Function Space of Time-Warps

The model described in the previous sections represents an activity using a nominal activity trajectory $a(t)$ and a probability distribution on the space of time warpings P_ψ. There are two inherent difficulties in practical implementations of such a model inspite of its rigour. Firstly, since the model attemps to learn a probability distribution on the space of permissible time-warping functions, the algorithm for learning this P_ψ requires a reasonable number of sample realizations of each action. In the presence of very few samples, the learning algorithm might lead to

underfitting of the data. Moreover, as inference using this model is done using Monte Carlo methods, the algorithms for inference are computationally expensive.

Suppose we relax the assumption about learning the probability distribution of permissible time-warps and instead attempt to learn a subset in the time-warping space and assume that the probability distribution of time-warps is uniform within the learnt subset. Each activity can now be represented by using a nominal activity trajectory given by $a(t)$ and W, the set containing all the time warping transformations permissible for that activity. Each realization of an activity is given by a trajectory $r(t) = a(f(t))$ where $f \in W$. Such a model is a special case of learning P_ψ where, we assume that the probability distribution is uniform on a subset $W \in \Gamma$ in the space of time-warpings. The advantage of using such a model where the probability distribution is assumed uniform is that both the learning and the inference algorithms become simple dynamic programming problems when we constrain the set W to be a convex set.

3.4.1 Activity specific time-warping space (W)

Even though $\mathbf{\Gamma}$ represents the space of all plausible time-warping transformations, every individual activity may only be able to access a subset W of the candidate functions in $\mathbf{\Gamma}$ because of the physical constraints imposed on the actor and the activity. We can then model the activity using a uniform distribution on this subset W. Then learning the parameters of the uniform distribution boils down to learning this subset W. Below, we discuss and visualize some properties of this activity specific time warping space W.

1. W is a subset of $\mathbf{\Gamma}$, i.e., $W \subset \mathbf{\Gamma}$.

2. $\gamma(t) = t$ is a candidate function in W, i.e., $\gamma(t) = t \in W$. This represents no time warping.

3. It is reasonable to assume that W is convex, i.e., $\forall\ \gamma_1, \gamma_2 \in W$ and $\alpha \in (0, 1)$, $\gamma = \alpha\gamma_1 + (1 - \alpha)\gamma_2 \in W$. Since the derivative is a linear operator, this means that if the rate of execution of some action unit can be speeded up by factors α_1 and α_2 then it can also be speeded up by any factor β in between α_1 and α_2. This is not just reasonable but in fact desirable.

This implies that W can be bounded above and below by functions u, $l \in W$ such that

$$u(t) \geq t \geq l(t) \ \ \forall t \in (0, 1) \qquad \text{and} \qquad u \geq \gamma \geq l \ \ \forall \gamma \in W \tag{3.20}$$

where $\gamma_1 \geq \gamma_2 \Longrightarrow \gamma_1(t) \geq \gamma_2(t) \ \ \forall t \in (0, 1)$. So, we can now index any such convex space W by the functions u and l and call it W_{ul} and learning W is essentially the same as learning the upper and lower bounding functions u and l.

3.4.2 Symmetric representation of an Activity Model

As described for the "wrapped-Gaussian" distribution, the representation of the activity model given by $M_1 = \{a(t), W_{ul}\}$ is not unique. Let $u_{new}(t) = f^{-1}(u(t))$ and $l_{new}(t) = f^{-1}(l(t))$ and let f be a member function in W_{ul}. Consider the new model $M_2 = \{b(t), W_{u_{new}l_{new}}\} = \{a(f(t)), W_{u_{new}l_{new}}\}$. For every realization of the model M_1, i.e., $a(\gamma_1(t))$ there exists a corresponding realization of the model M_2 given by $b(f^{-1}(\gamma_1(t)))$. Therefore the two models M_1 and M_2 are equivalent. As before, we will resolve this ambiguity by specifying a synchronizing time such that the average of all the warping functions in W_s is the identity warping function. The *symmetric* representation of the model is such that $u_{new}(t) - t = t - l_{new}(t)$.

Therefore the activity specific warping space can be represented as $W_s = W_{u_{new}l_{new}}$ where $s(t) = u_{new}(t) - t = t - l_{new}(t)$, represents the extent of possible temporal warpings. This symmetric representation of the model is unique, i.e., if $M_1 = \{a_1(t), W_{s1}\}$ and $M_2 = \{a_2(t), W_{s2}\}$, then $M_1 = M_2 \Longleftrightarrow a_1 = a_2$ and $s_1 = s_2$.

Given a non-symmetric representation of the model, i.e., $M_1 = \{a(t), W_{ul}\}$, we still need to determine a time-warping function f such that upper and lower bounding functions of the new model are symmetric about the diagonal. This is achieved as

$$\begin{aligned} & u_{new}(t) - t && = t - l_{new}(t) \qquad (3.21) \\ & \text{(Substituting for } u_{new}(t) && \text{and applying the } u^{-1} \text{ operator)} \\ \Rightarrow \quad & f(t) = && \{2u^{-1}(t) - f^{-1}(l(u^{-1}(t)))\}^{-1} \end{aligned}$$

This implicit function equation can be solved by fixed point iterations as $f_{(i)}(t) = \{2u^{-1}(t) - f^{-1}_{(i-1)}(l(u^{-1}(t)))\}^{-1}$, where $f_{(i)}$ represents the approximation of f in the i^{th} iteration. We initialize the iteration with $f_{(0)}(t) = \frac{u(t)+l(t)}{2}$. We observe that it converges within very few iterations with such an initialization. Once we have obtained this symmetrizing time warp f then any non-symmetric model parameters $M_1 = \{a(t), W_{ul}\}$ can be transformed to its symmetric (unique) counterpart as $M = \{b(t), W_s\}$, where $b(t) = a(f(t))$ and $s(t) = u_{new}(t) - t = t - l_{new}(t) = f^{-1}(u(t)) - t$.

3.4.3 Learning Model Parameters

Learning the model parameters can be done as before by iterating between the two unknowns ($a(t)$ and P_γ). Learning the nominal activity trajectory $a(t)$ is done as

described in Section 3.3.2. The only difference between earlier and now is during the estimation of the parameters P_ψ. Earlier we computed the Karcher mean and the covariance of P_ψ for the wrapped-Gaussian distribution, here since the parameters of P_γ are given by the upper and lower bounding functions we need to estimate them. Given an estimate of the activity trajectory $a(t)$ and corresponding warping functions $\gamma_i(t)$ for each realization, the the upper and the lower bounding functions for the activity specific time-warping set can be estimated as

$$\hat{u}(t) = \max_{i=1,2,...N} \gamma_i(t),\ \forall t \in (0,1) \qquad \text{and} \qquad \hat{l}(t) = \min_{i=1,2,...N} \gamma_i(t),\ \forall t \in (0,1). \tag{3.22}$$

Since each γ_i is constrained to be monotonously increasing and the end points are fixed, it is easy to see that the estimates $\hat{u}(t)$ and $\hat{l}(t)$ also inherit these properties. Thus the estimated model $\hat{M}$ is given by $\hat{M} = \{\hat{b}(t), W_{ul}\}$. This model parameters correspond to the non-symmetric version of the model and can be easily transformed to the equivalent symmetric version of the model using the procedure described in Section 3.4.2.

3.4.4 Classification using the model

The primary advantage of using the uniform distribution on the space of time-warping functions instead of learning a class-specific probability density function is that the classification algorithm becomes computationally efficient. While classification in the general case is dependent on Monte-carlo methods, we show how a simple dynamic programming based algorithm will suffice for classification using the uniform distribution based model. Suppose we have M different activity models given by $M_i = \{a_i(t), W_{s_i}\}$ for $i = 1, ..M$. Given a test sequence $h(t)$, the activity recognition problem is one of identifying the model that generated the test

sequence $h(t)$. We do this in two steps. Firstly, assuming that the test sequence $h(t)$ is generated from the model M_i, we estimate the best warping transformation $\hat{f}_i$ from W_{s_i} that would warp a_i to h, i.e.,

$$\hat{f}_i = \min_{f \in W_{s_i}} dist(h(t), a_i(f(t))) \tag{3.23}$$

$$\hat{I} = \arg \min_{i=1,\ldots M} dist(h(t), a_i(\hat{f}_i(t))) \tag{3.24}$$

Activity recognition is performed by minimizing the warping error between the nominal activity trajectory and the test sequence. Note that the search of warping functions is performed only over the corresponding activity specific warping set. The above-mentioned intuitive idea for activity recognition can be easily implemented by a simple variation of the DTW. In the DTW algorithm, instead of arbitrarily limiting the warping function to lie within some window (typical choices are uniform window and parallelogram window), we replace the window constraints by the upper and lower bounds for the warping function that we have learnt for each model. Thus, the DTW algorithm with the window width being given by $u(t) = s(t) + t$ and $l(t) = t - s(t)$ computes the distance that is being minimized in (3.24).

$$\hat{I} = \min_{i=1,\ldots M} DTW(a_i, h, s) \tag{3.25}$$

where, $DTW(a_i, h, s)$ stands for the implementation of the DTW algorithm with the warping window constraints given by $u(t) = s(t) + t$ and $l(t) = t - s(t)$.

3.5 Experiments

We tested the algorithms on three different datasets - UMD Common Activities dataset, the INRIA iXmas dataset and the USF gait dataset. We used a warpped-Gaussian probability distribution for P_ψ with its parameters stored using a set of

tangent plane vectors u_ψ and their covariance matrix Σ_ψ. We denote the experimental results using this algorithm as P_{Gauss} in the results. We also implemented the uniform distribution on the space of time-warping functions using dynamic programming and performed maximum likelihood inference using this model. We denote the results using this method as P_{Unif} in the results.

3.5.1 Common Activities Dataset

We used the UMD common activities dataset [159], a dataset of common activities to perform preliminary experiments to validate our model. The dataset consists of 10 activities and 10 different instances of each activity. We partition the dataset into 10 disjoint sets each containing 1 instance of every activity. In order to test the recognition for each set, we first learn the model parameters from the remaining nine sets and then perform recognition for the test sequences. We repeat the process for each of the 10 sets. Thus we ensure that there is no overlap between the training set and the test sequences. Figure 3.3 shows the 10 X 100 similarity matrix for using the function space algorithm with the uniform distribution on the space of temporal warps. Each column corresponds to a different test sequence while each row corresponds to a different activity. The strongly block diagonal nature of the similarity matrix indicates that the recognition algorithm performs well. In fact, on this database we obtained 100% recognition using both our algorithms.

3.5.2 INRIA iXmas dataset

The INRIA multiple-camera multiple video database of the PERCEPTION group consists of 11 daily-live motions performed each 3 times by 10 actors. The actors freely change position and orientation. Every execution of the activity is done at

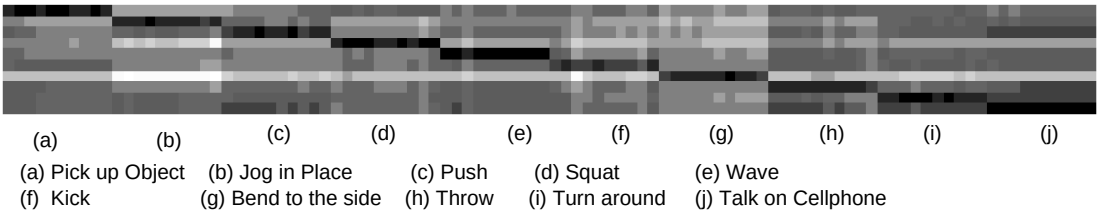

Figure 3.3: 10 X 100 Similarity matrix of 100 sequences and 10 different activities using the function space algorithm.

a different rate. For this dataset, we extract $16 \times 16 \times 16$ circular FFT features as described in [170]. Since the actors were free to perform the actions the rate at which these actions were performed varied significantly as was shown in Figure 3.1. So most approaches that cannot handle this vast temporal rate variations, instead model the entire segment as a single motion history volume [170]. Instead, we build a time series of the circular FFT features described in [170]. This allows us to learn the nature of the temporal rate changes between various executions of an action. Using these features, we performed a recognition experiment on the provided data similar to those done in [170]. For the recognition experiment, we used only one segment for each activity which best represented that activity as in [169]. The recognition results are summarized in table 5. We used $16 \times 16 \times 16$ circular FFT features in all our experiments here while the results reported in [170] used $32 \times 32 \times 32$ features. The confusion matrix showing confusion between the activities using both the wrapped-Gaussian and the dynamic programming based uniform distribution model are shown in Table 3.2. Note that uniform distribution based model described in Section 3.4 is significantly more computationally efficient compared to the Monte-Carlo based inference using the wrapped-Gaussian distribution on the tangent space of warp space.

	Activity	**PCA** [170]	**Mahalanobis** [170]	**LDA** [170]	**System Distance** [153]	P_{Unif} (This paper)	P_{Gauss} (This paper)
1	Check Watch	53.33	73.33	76.67	93.33	100	93.33
2	Cross Arms	23.33	86.67	100	100	100	100
3	Scratch Head	46.67	86.67	80	76.67	100	100
4	Sit Down	66.67	93.33	96.67	93.33	96.67	100
5	Get Up	83.33	93.33	93.33	86.67	96.67	100
6	Turn Around	80	96.67	96.67	100	100	100
7	Walk	90	100	100	100	100	100
8	Wave Hand	50	70	73.33	93.33	96.67	96.67
9	Punch	70	86.67	83.33	93.33	83.33	90
10	Kick	50	86.67	90	100	80	100
11	Pick Up	60	90	86.67	96.67	90	100
	Average	61.21	87.57	88.78	93.93	94.85	98.18

Table 3.1: Comparison of view invariant recognition of activities in the INRIA dataset using our approaches (P_{Unif} and P_{Gauss}) with the approaches proposed in [170] and [153].

Motifs	**1**	**2**	**3**	**4**	**5**	**6**	**7**	**8**	**9**	**10**	**11**
Sit Down	30(28)	0(0)	0(1)	0(1)	0(0)	0(0)	0(0)	0(0)	0(0)	0(0)	0(0)
Get Up	0(0)	30(30)	0(0)	0(0)	0(0)	0(0)	0(0)	0(0)	0(0)	0(0)	0(0)
Turn Around	0(0)	0(0)	30(30)	0(0)	0(0)	0(0)	0(0)	0(0)	0(0)	0(0)	0(0)
Check Watch	1(0)	0(0)	0(0)	29(30)	0(0)	0(0)	0(0)	0(0)	0(0)	0(0)	0(0)
Cross Arms	1(0)	0(0)	0(0)	0(0)	29(30)	0(0)	0(0)	0(0)	0(0)	0(0)	0(0)
Scratch Head	0(0)	0(0)	0(0)	0(0)	0(0)	30(30)	0(0)	0(0)	0(0)	0(0)	0(0)
Walk	0(0)	0(0)	0(0)	0(0)	0(0)	0(0)	30(30)	0(0)	0(0)	0(0)	0(0)
Wave Hand	1(1)	0(0)	0(0)	0(0)	0(0)	0(0)	0(0)	29(29)	0(0)	0(0)	0(0)
Punch	3(1)	0(1)	0(0)	0(0)	0(0)	0(0)	0(0)	1(1)	25(27)	0(0)	0(0)
Kick	5(0)	0(0)	0(0)	0(0)	1(0)	0(0)	0(0)	0(0)	0(0)	24(30)	0(0)
Pick Up	1(0)	0(0)	0(0)	0(0)	2(0)	0(0)	0(0)	0(0)	0(0)	0(0)	27(30)

Table 3.2: Confusion matrix using P_{Gauss}(outside parenthesis and P_{Unif} (inside paranthesis) on the INRIA dataset.

3.5.3 USF Gait Database

Note on gait-based person identification Since the model for learning the function space time-warpings is not explicitly dependent on the choice of features, one could potentially use the same model to learn individual specific function spaces in order to perform activity-based person identification. The only difference would be that we would choose a feature that is person-specific (e.g., silhouette). The nominal activity trajectory would be individual specific in this case. Various external conditions (like surface, shoe) induce systematic time-warping variations within the gait signatures of each individual. The function space of temporal warpings for each individual amounts to learning the class of person specific warping functions. By learning the function space of these variations we are able to account for the effects of such external conditions. This will allow the same basic approach to be applied for both action recognition and activity based person identification by the use of appropriate features.

In order to compare the performance of our algorithm with the current state of the art algorithms, we also performed a gait-based person identification experiment on the publicly available USF gait database [137]. The USF database consists of 71 people in the Gallery. Various covariates like camera position, shoe type, surface and time were varied in a controlled manner to design a set of challenge experiments [137]. We performed a round-robin recognition experiment in which one of the challenge sets was used as test while the other 7 were used as training examples. The process was repeated for each of the 7 challenge sets on which results have been reported. Table 3.3 shows the identification rates of our algorithm with a uniform distribution on the space of warps (P_{Unif}), our algorithm with a wrapped Gaussian distribution on the tangent space of warps with shape as a feature and

with binary image feature (P_{Gauss} and $P_{GaussIm}$). For comparison the table also shows the baseline algorithm [137], simple DTW on shape features [162] and the image-based HMM [85] algorithm on the USF dataset for the 7 probes A-G. Since most of these other algorithms could not account for the systematic variations in time-warping for each class the recognition experiment they performed was not round robin but rather used only one sample per class for learning. Therefore, to ensure a fair comparison, we also implemented a round-robin experiment using the linear warping (P_LW).

Table 3.3: Comparison of Identification rates on the USF dataset

Probe	Baseline	DTW Shape	HMM Shape	HMM Image	pHMM [101]	P_{LW}	P_{Unif}	P_{Gauss}	$P_{GaussIm}$
Avg.	42	42	41	50	65	51.5	59	59	64
A	79	81	80	96	85	68	70	78	82
B	66	74	72	86	89	51	68	68	78
C	56	52	56	74	72	51	81	82	76
D	29	29	22	32	57	53	40	50	48
E	24	20	20	28	66	46	64	51	54
F	30	19	20	17	46	50	37	42	56
G	10	19	19	21	41	42	53	40	55

The average performance of our algorithms P_{Unif} and P_{Gauss} are better than all the other algorithms that use the same feature, (DTW/HMM (Shape) [162] and Linear warping P_{LW}) and is also better than the baseline [137] and HMM [85] algorithms that use the image as a feature. The image based pHMM algorithm [101] outperforms our algorithm. One reason for this is that the image as a feature performs

better than shape as a feature for the USF dataset. But, it is a computationally very intensive feature (of the order of number of pixels) and consequently leads to algorithms that are very slow. Therefore, we prefer to use the shape as a feature. Inspite of this obvious handicap, the performance of our algorithm is comparable to the image based pHMM algorithm for many probes. The improvement in performance while using binary image as a feature is shown in the last column ($P_{GaussIm}$). The experimental results presented here clearly show that using multiple training samples per class and learning the distribution of their time warps makes significant improvement to gait recognition results. While most algorithms based on learning from a single sample led to overfitting and therefore performed much better when the gallery was similar to the probe (Probe A-C), they also performed very poorly when the gallery and the probes were significantly different. But, since our algorithm had significant generalization ability (becasue we learn the distribution of time warps) the performance of our algorithm did not suffer from overfitting and therefore did not drop as much when moving from probes A-C to Probles D-G.

3.6 Other applications

3.6.1 Clustering Activity Sequences

Algorithm for Clustering There are several scenarios where one requires a clustering algorithm to be rate-invariant. Under such scenarios it becomes reasonable to use the rate-invariant model for activities described above as the basis for clustering. When rate-invariance is not a desirable property traditional clustering algorithms such as K-nearest neighbour might be reasonable choices for clustering.

We performed clustering experiments on the UMD common activities dataset and the USF gait database using the fast and computationally efficient uniform distribution version of the algorithm denoted by P_{Unif}. The clustering algorithm, based on expectation maximization (EM) is very similar to the Lloyd-Max algorithm [79] and can be used to organize a database of sequences for efficient retrieval. Let us assume that we know the number of clusters, N and the cluster centers $c_1, c_2, ...c_N$. Then, each of the sequences in the database can be associated with one of N clusters. This can be done using a maximum-likelihood approach as described earlier in (3.25). This forms the Maximization step of the EM algorithm. The Expectation step of the algorithm involves recomputing the new cluster centers from cluster memberships evaluated during the Maximization step. We iterate these 2 steps until convergence. In all our experiments, we initialized the cluster centers randomly.

Clustering on Common Activities Dataset We performed a clustering experiment on the 100 activity sequences collected as a part of the Common Activities dataset. We chose the number of clusters N to be 10 since there were 10 different activities. If clustering were perfect, then the 100 activity sequences would be clustered into 10 different clusters, each cluster containing 10 sequences that correspond to that particular activity. But in reality, clustering would be imperfect and some of the 100 sequences would be misaligned in the wrong cluster. We repeated the clustering experiment several (about 50) times, with a random initialization of cluster centers during each trial. On an average, the algorithm converged in about 10 iterations and about 92% of the sequences were clustered correctly. Even during some adverse initializations the clustering performance was greater that 80%.

3.6.2 Organizing a Large Database of Activities

With the decreasing cost of storage, the size of activity databases is increasing rapidly. For example, the complete USF gait database [137] consists of about 122 classes and a total of more than 1000 sequences. As the size of the database increases, the number of 'distance' computations that must be performed on every query also increases linearly with the size of the database. This poses a significant bottleneck for practical activity recognition systems. We show that organizing the database of sequences using the clustering algorithm described in Section 3.6.1 decreases this computational burden significantly. The price paid is a small decrease in recognition performance. We organize the database of activities in the form of a dendrogram as shown in Figure 3.4. At each level of the dendrogram the number of branches (B) was set to 3. The number of levels to which the dendrogram is 'grown' determines the trade-off between computation and accuracy. As the number of levels is increased, the number of 'distance' computations that must be performed before finding the class membership of a given test sequence decreases. Therefore, the computational burden of the algorithm also decreases. But this might introduce a decrease in classification performance. When the dendrogram is fully grown (i.e., when each leaf of the dendrogram represents one activity), there will be $log_B N$, levels and therefore $Blog_B N$ 'distance computations'. Let us consider the USF database which consists of 122 subjects and a total of 1870 sequences. A nearest neighbour classifier on this database must perform 1870 distance computations in order to classify a new test sequence. But if we assume that we organize the database in the form of a 'fully grown dendrogram', with each leaf node representing each of the 122 individuals, then one would just have to perform about $Blog_B N = 3 * log_3 122 \approx 14$ 'distance computations'. This is a very

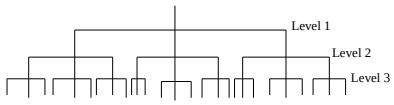

Figure 3.4: Dendrogram for organizing an activity database

significant computational saving.

We performed an experiment to evaluate the efficiency of organizing the database on a subset of the USF database as in Section 3.5.3. In our experiments, we grow the dendrogram upto 2 levels. We measure efficiency of organization (η) as a ratio of the recognition rate before and after organization.

$$\eta = 100 * \frac{\text{Identification rate after organization}}{\text{Identification rate before organization}} \tag{3.26}$$

The efficiency η is strongly related to clustering performance and it is reasonable to expect the efficiency η to increase with better clustering. Table 3.4 shows the efficiency of organization for the various probes in the USF dataset. On this data, the dendrogram organization of the database reduced the computational time by a factor of about 30. This means that the processing time for large databases will be reduced from the order of days to a matter of hours. For such significant reduction in processing time, the Table 3.4 shows that the decrease in recognition performance is not drastic.

Table 3.4: Efficiency of Organization on the USF dataset

Probe	A	B	C	D	E	F	G	Avg
η	76	81	84	100	82	100	95	89

3.7 Summary and conclusions

In this chapter, we addressed an important but often neglected problem in modeling activity, that of temporal warping of the activity trajectories. Our model for an activity describes each activity using a nominal activity trajectory and a probability distribution on the space of permissible temporal warpings. We discussed the case of a parameteric wrapped-Gaussian distribution on the tangent space of time-warps and derive Monte Carlo sampling-based Bayesian algorithm for classification. We then discussed the spacial case of a convex uniform distribution on the space of time-warps and show that this special case allows us to derive computationally efficient algorithms for a slight decrease in modeling efficieny and classification performance. Finally, we showed several experiments on publicly available action recognition and gait-based person identification datasets.

Chapter 4

Simultaneous Tracking and Behavior Analysis

Accurate shape dynamical models are not only efficient for the problem of recognition, but they also serve as effective priors that enable accurate tracking of subjects in video. In this chapter, we show how accurate shape dynamical models can be used for simultaneous tracking and behavior analysis. We apply these principles to the problem of tracking the position, orientation and the behavior of bees in a hive. We present a system that can be used to analyze the behavior of insects and, more broadly, provide a general framework for the representation and analysis of complex behaviors.

Behavioral research in the study of the organizational structure and communication forms in social insects like the ants and bees has received much attention in recent years [54] [145]. Such a study has provided some practical models for tasks like work organization, reliable distributed communication, navigation etc [112] [107]. Usually, when such an experiment to study these insects is setup, the insects in an observation hive are videotaped. The hours of video data are then

manually studied and hand-labeled. This task of manually labeling the video data takes up the bulk of the time and effort in such experiments. In this chapter, we discuss general methodologies for automatic labeling of such videos and provide an example by following the approach for analyzing the movement of bees in a bee hive. Contrary to traditional approaches that first track objects in video and then recognize behaviors using the extracted trajectories, we propose to simultaneously track and recognize behaviors. In such a joint approach, accurate modeling of behaviors act as priors for motion tracking and significantly enhances motion tracking while accurate and reliable motion tracking enables behavior analysis and recognition.

We present a system that can be used to analyze the behavior of insects and, more broadly, provide a general framework for the representation and analysis of complex behaviors. Such an automated system significantly speeds up the analysis of video data obtained from experiments and also reduces manual errors in the labeling of data. Moreover, parameters like the orientation of various body parts of the insects (which are of great interest to behavioral researchers) can be automatically extracted using such a framework. The system requires the technical input of a behavioral researcher (who would be the end user) regarding the type of behaviors that would be exhibited by the insect being studied.

The salient characteristics are the following:

- We suggest a joint tracking and behavior analysis instead of the traditional "track and then recognize" approach for activity analysis. The principles for simultaneous tracking and behavior analysis presented in this paper should be applicable in a wide range of scenarios like analyzing sports videos, activity monitoring, surveillance etc.

- We show how the method can be extended to tackle multiple behaviors using hierarchical Markov models to model various behaviors. We define instantaneous low level motion states like hover, turn, waggle etc., and model each of the dances as a Markov model over these low level motion states. Switching between behaviors (dances) is modeled as another Markov model over the discrete labels corresponding to the various dances.

- We also present methods for detecting and characterizing abnormal behaviors.

- In particular, we study the simultaneous tracking and analysis of bee dances in their hive. This is an appropriate setting in which to study the "track and recognize simultaneously" approach suggested by this paper since a) The extreme clutter and presence of several similar bees make traditional tracking in such videos extremely difficult and consequently most tracking algorithms suffer frequent missed tracks and b) The rich variety of structured behaviors that the bees exhibit enables a rigorous test of behavior modeling. We have modeled a few of the dances of the foraging bees and estimated the parameters of the waggle dance.

4.1 Bee Dances as a means of communication

When a worker honeybee returns to her nest after a visit to a nourishing food source, she performs a so-called 'dance', on the vertical face of the honeycomb, to inform her nest mates about the location of the food source [54]. This behavior serves to recruit additional workers to the location, thus enabling the colony to exploit the food source effectively. Bees perform essentially two types of dances,

in the context of communicating the location of food sites. When the site is very close to the nest (typically within a radius of 50 metres), the bee performs a so-called 'round dance'. This dance consists of a series of alternating left-hand and right-hand loops, as shown in Figure 4.1(a). It informs the nest mates that there is an attractive source of food located within a radius of about 50 m from the nest. When the site is at a considerable distance away from the nest (typically greater than 100 meters) the bee performs a different kind of dance, the so-called 'waggle dance', as shown in Figure 4.1(b). In this dance, the transition between one loop and the next is punctuated by a 'waggle phase' in which the bee waggles her abdomen from side to side whilst moving in a more-or-less straight line. Thus, the bee executes a left-hand loop, performs a waggle, executes a right-hand loop, performs a waggle, executes a left-hand loop, and so on. During the waggle phase, the abdomen is waved from side to side at an approximately constant frequency of about 12 Hz. The waggle phase contains valuable information about the location of the food source: The duration of the waggle phase (or, equivalently, the number of waggles in the phase) is roughly proportional to the bee's perceived distance of the food source: the longer the duration, the greater the distance. The orientation of the waggle axis (the average direction of the bee's long axis during the waggle phase) with respect to the vertically upward direction conveys information about the direction of the food source. The angle between the waggle axis and the vertically upward direction is equal to the azimuthal angle between the sun and the direction of the food source. Thus, the waggle dance is used to convey the position of the food source in a polar co-ordinate system (in terms of distance and direction), with the nest being regarded as the origin and the sun being used as a directional compass [54]. The 'attractiveness' of the food source is also conveyed

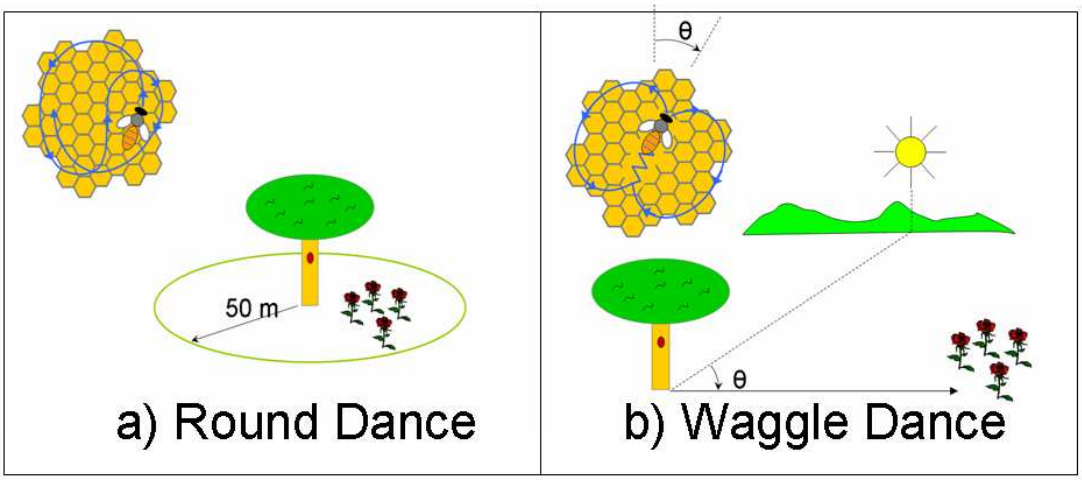

Figure 4.1: Illustration of the 'round dance', the 'waggle dance' and their meaning.

in the waggle dance: the greater the attractiveness, the greater is the number of loops that the bee performs in a given dance, and the shorter the duration of the return phase (the non-waggle period) of each loop. The waggle frequency of 12 Hz is remarkably constant from bee to bee and from hive to hive [54]. The attractiveness of a food source, however, may depend upon the specific foraging circumstances, such as the availability of other sources and their relative profitability, as well as an individual's knowledge and experience with the various sites. Thus, the number of dance loops and the duration of the return phase may vary from bee to bee, and from one day to the next in a given bee [54].

There are additional dances that bees use to communicate other kinds of information [54]. For example, there is the so-called 'jostling dance', where a returning bee runs rapidly through the nest, pushing nest mates aside, apparently signaling that she has just discovered an excellent food source; the 'tremble' dance [139], where a returning forager shakes her body from side to side, at the same time rotating her body axis by about 50 deg every second or so, is used by a returning

bee to inform her nest mates that there is too much nectar coming in, and she is consequently unable to unload her food to a food-storing bee [139]; the 'grooming dance' in which a standing bee raises her middle legs and shakes her body rapidly to and fro, beckoning other bees to assist her with her grooming activities; and the 'jerking dance', performed by a queen, consisting of up-and-down movements of the abdomen, usually preceding swarming or a nuptial flight. However, the pinnacle of communication in insects resides undoubtedly in the waggle dance. The surprisingly symbolic and abstract way in which this dance is used to convey information about the location of a food source has earned it the status of a 'language' [54].

4.1.1 Organization of the chapter

In Section 4.2, we discuss the shape model to track insects in videos and show how using the model helps in inferring parameters of interest about the motions exhibited by the insects. Section 4.3 discusses the issue of modeling behaviors, detecting and characterizing abnormal behaviors. Section 4.4 discusses the tracking algorithm. Detailed experimental results for the problem of tracking and analysing bee dances are provided in Section 4.5.

4.2 Anatomical/Shape Model

Modeling the anatomy of insects is very important for reliable tracking, because the structure of their body parts and their relative positions present some physical limits on their possible relative orientations. In spite of their great diversity, the anatomy of most insects is rather similar. All insects possess six legs. An insect body has a hard exoskeleton protecting a soft interior. The body is divided into

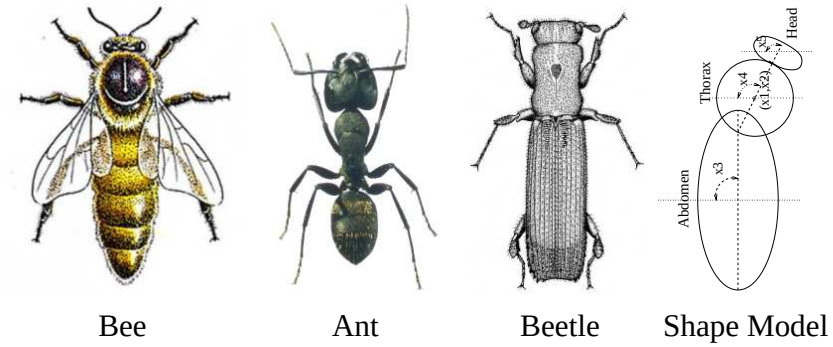

Figure 4.2: A Bee, an Ant, a Beetle and Shape Model

three main parts- the head, thorax and the abdomen. The abdomen is divided into several smaller segments. Figure 4.2 shows the image of a bee, an ant and a beetle. Though there are individual differences in their body structure, the three main parts of the body are evidently visible. Each of these three parts can be regarded as rigid body parts for the purposes of video based tracking. The interconnection between parts provide some physical limits for the relative movement of these parts. Most insects also move towards the direction of their head. Therefore, during specific movements such as turning, the orientation of the abdomen usually follows the orientation of the head and the thorax with some lag. Such interactions between body parts can be easily captured using a structural model for insects.

We model the bees with three ellipses, one for each body part. We neglect the effect of the wings and legs on the bees. Figure 4.2 shows the shape model of a bee. Note that the same shape model can be used to adequately model most other insects also. The dimensions of the various ellipses are fixed during initialization. Currently the initialization for the first frame is manual. It consists of clicking two points to indicate the enclosing rectangle for each ellipse. Automatic initialization is a challenging problem in itself and is outside the scope of our current work.

The location of the bee and its parts in any frame can be given by five parameters-

namely, the location of the center of the thorax(2 parameters), the orientation of the head, the orientation of the thorax and the orientation of the abdomen (refer Figure 4.2). Tracking the bee over a video essentially amounts to estimating these five model parameters($\mathbf{X} = [x_1\ x_2\ x_3\ x_4\ x_5]'$) for each frame. This 5−parameter model has a direct physical significance in terms of defining the location and the orientation of the various body parts in each frame. These physical parameters are of importance to behavioral researchers.

4.2.1 Limitations of the Anatomical Model

We have assumed that the actual sizes of these ellipses do not change with time. This would of course be the case as long as the bee remains at the same distance from the camera. Since the behaviors we study in our work (like the waggle dance) are performed on a vertical plane inside the beehive, and the optical axis of the video camera was perpendicular to this plane, the bees projected the same part sizes during the entire length of video captures. Nevertheless, it is very easy to incorporate the effect of distance from the camera in our shape model, by introducing a scale factor as one more parameter in our state space. Moreover, the bees are quite small and were far enough from the camera that perspective effects could be ignored. The spatial resolution with which the bees appear in the video also limit the accuracy with which the physical model parameters can be recovered. For example, when the spatial resolution of the video is low, we may not be able to recover the orientation of the body parts individually.

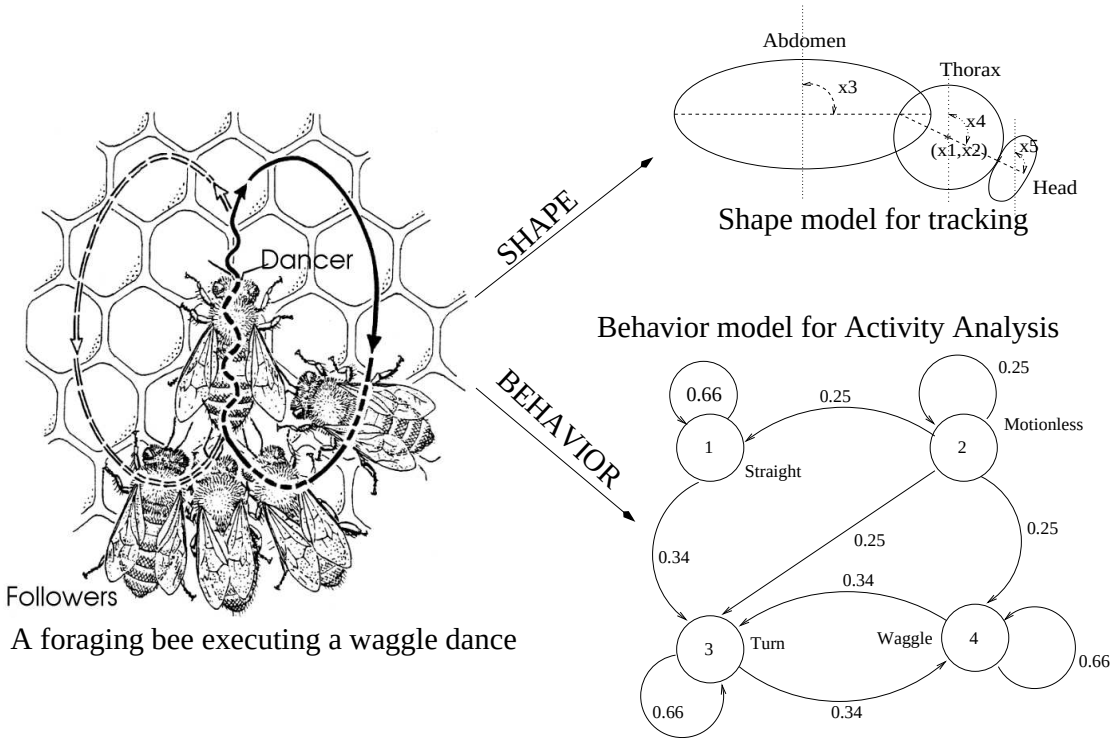

Figure 4.3: A Bee performing a waggle dance and the behavioral model for the Waggle dance

4.3 Behavior Model

Insects, especially social insects like bees and ants, exhibit rich behaviors as described in Section 4.1. Modeling such behaviors explicitly is helpful in accurate and robust tracking. Moreover, explicitly modeling such behaviors also leads to algorithms where position tracking and behavior analysis are tackled in a unified framework. Several algorithms use motion models (like constant velocity model, random walk model etc) for tracking [76] [89] [13] [179]. We propose the use of behavioral models for the problem of tracking insects. Such behavioral models have been used for certain other specific applications like human locomotion [22] [177] [126]. The difference between motion models and behavioral models is the range of time scales at which modeling is done. Motion models typically model the probability distribution (pdf) of the position in the next frame as a function of the position in the current frame. Instead, behavioral models capture the probability distribution of position over time as a function of the behavior that the tracked object is exhibiting. We believe that the use of behavioral models presents a significant layer of abstraction that enhances the variety and complexity of the motions that can be tracked automatically.

4.3.1 Deliberation of the Behavior model

The state space for tracking the position and body angles of the insect in each frame of the video sequence is determined by the choice of the shape model. In our specific case, this state space comprises of the x,y position of the center of the thorax and the orientation of the three body parts in each frame ($\mathbf{X} = [x_1\ x_2\ x_3\ x_4\ x_5]'$). A given behavior can be modeled as a dynamical model on this space. At one extreme one can attempt to learn a dynamical model like an autoregressive model or an

autoregressive and moving average (ARMA) model directly on this state space. A suitably and carefully selected model of this form might be able to capture large time scale interactions that are a characteristic of complex behaviors. But these models constructed directly on the position state space suffer from two significant handicaps. Firstly, to incorporate long range interactions these models would necessarily have a large number of parameters and learning all these parameters from limited data would be brittle. It would be nice to somehow learn a compact set of parameters that can capture such large time range interactions. Secondly, these models are opaque to the behavioral researcher who is continuously interacting with the system during the learning phase. Since the system does not replace the behavioral researcher but rather assists him by tracking and analyzing behaviors of bees that the researcher selects, it is very important for the model to be easily amenable to the intended user of the system.

One can achieve both these objectives by abstracting out local motions like turning, hovering, moving straight ahead etc, and modeling the behavior as a dynamical model on such local motions. Such a model would be simple and intuitive to the behavior researcher and the number of parameters required to model behaviors would be dependent only on the number of local motions modeled. When the need to specify and learn new behaviors arises, he/she would have to focus only on the dynamical model of the local motions, since the model for the local motions themselves would already be a part of system. *In short, the local motions act as some sort of a vocabulary that enables the end user to effectively interact with the system.*

4.3.2 Choice of Markov Model

As described in the previous section, we first define probability distributions for some basic motions such as moving straight ahead, turning, waggle and hovering at the same location. Once these descriptions have been learnt we define each behavior using an appropriate model on this space of possible local motions. Prior work [47] on analyzing the behaviors of bees has used Markov models to model the behaviors. That study reports promising results on recognizing behaviors using such Markov models. More recently, [116] used SLDS to model and analyze bee dances. They then noted that the models can be made more specific and accurate by incorporating a duration model within the framework of a linear dynamical system. They use this parametrized duration modeling with a switched linear dynamical system and show improved performance [117]. We could in principle choose any of these models for analyzing bee dances. Note that the tracking algorithm would be identical irrespective of the specific choice of model since it is based on particle filtering and therefore just requires that we be able to efficiently sample from these motion models. The various dances that the bees perform are very structured behaviors and consequently we need these models to have enough expressive power to capture these structures. Nevertheless, we also note that at this stage these models are acting as priors to the tracking algorithm and therefore if these models were very peaky/specific, then even a small change in the actual motion of the bees might cause a loss of track. Therefore, the model must also be fairly generic, in the sense that it must be able to continue tracking even if the insect deviates from the model. Taking these factors into account we used Markov models very similar to those used by [47] to model bee behaviors. We noticed that even such a simple Markov model significantly aided tracking performance

and enabled the tracker to continue to maintain track in several scenarios where the traditional tracking algorithms failed (see Section 4.5.4). Another significant advantage of choosing a simple Markov model to act as behavior priors rather than more sophisticated and specific models, is the fact that the very generality of the model makes the tracking algorithm fairly insensitive with respect to the initialization of the model parameters. In practice, we found that the tracking algorithm was fairly insensitive to the initialization of the model parameters and was quickly able to refine the corresponding model parameters within about 100-200 frames.

4.3.3 Mixture Markov Models for Behavior

Mixture models have been proposed and used successfully for tracking [77] [14]. Here, we advocate the use of Markovian mixture models in order to enable persistent tracking and behavior analysis. Firstly, basic motions are modeled creating a vocabulary of local motions. These basic motions are then regarded as states and behaviors are modeled as being Markovian on this motion state space. Once each specific behavior has been modeled as a Markov process, then our tracking system can simultaneously track the position and the behavior of insects in videos.

We model the probability distributions of location parameters $\mathbf{X}$ for certain basic motions($m_1 - m_4$). We model four different motions- 1) Moving straight ahead, 2) Turning, 3) Waggle, and 4) Motionless. The basic motions, straight, waggle and motionless are modeled using Gaussian pdfs (p_{m1}, p_{m3}, p_{m4}) while a mixture of two Gaussians (p_{m2}) is used for modeling the turning motion (to accommodate

the two possible turning directions).

$$p_{mi}(X_t/X_{t-1}) = N(X_{t-1} + \vec{\mu_{mi}}, \Sigma_{mi}); for\ i = 1, 3, 4. \quad (4.1)$$

$$p_{m2}(X_t/X_{t-1}) = 0.5N(X_{t-1} + \vec{\mu}_{m2}, \Sigma_{m2}) + 0.5N(X_{t-1} - \vec{\mu}_{m2}, \Sigma_{m2}) \quad (4.2)$$

Each behavior B_i is now modeled as a Markov process of order K_i on these motions, i.e.,

$$\mathbf{s}_t = \sum_{k=1}^{K_i} A^k_{B_i} \mathbf{s}_{t-k}; \quad (4.3)$$

where s_t is a vector whose j^{th} element is $P(\text{motion state} = m_j)$ and K_i is the model order for the i^{th} behavior B_i. The parameters of each behavior model are made of autoregressive parameters $A^k_{B_i}$ for $k = 1..K_i$. We discuss methods for learning the parameters of the behavior model later.

We have modeled three different behaviors - the waggle dance, the round dance and a stationary bee using a first order Markov model. For illustration, we discuss the manner in which the waggle dance is modeled. Figure 4.3 shows the trajectory followed by a bee during a single run of the waggle dance. It also shows some followers who follow the dancer but do not waggle. A typical Markov model for the waggle dance is also shown in Figure 4.3.

The trajectory of the bee can now be viewed as a realization from a random process following a mixture of behaviors. In addition, we assume that the behavior exhibited by the bee changes in a Markovian manner, i.e.,

$$B_t = T_B B_{t-1}; \quad (4.4)$$

where T_B is the transition probability matrix between behaviors. Note that T_B has a dominant diagonal. Estimating the trajectory and the specific behavior exhibited

by the bee at any instant is then a state inference problem. This can be solved using one of several techniques for estimating the state given the observations.

Thus the model consists of a 3 tier hierarchy. At the first level, the dynamics of local motions are characterized. These act as a vocabulary enabling the behavior researcher to easily interact with the system in order to add new behaviors, and analyze the output of the tracking algorithm without being bogged down by the particulars of the data capture. Behaviors that bees exhibit are modeled as Markovian on the space of local motions forming the second tier of the hierarchy. Finally, switching between behaviors is modeled as a diagonal dominant Markov model completing the model. The first two tiers of the hierarchy, dynamics and behavior may be collapsed into a single tier. But this would be disadvantageous since it would a) couple the specifics of data capture with the behavior models and b) also make it significantly more difficult for the behavior researcher (end user) to efficiently interact with the system.

4.3.4 Limitations and Implications of the choice of Behavior model

As described above, the choice of Markov model on a vocabulary of a set of low level motions was motivated primarily from two design considerations - a) ease of use for the end user b) generality of the model allowing the tracking algorithm to be robust to initialization parameters. But this choice also leads to certain limitations. For one, it might indeed be possible to collapse the entire three tier hierarchy of motion modeling into one large set of motion models all at the dynamics stage. But, such a model would suffer from significant disadvantages since the number of required parameters would significantly increase. Moreover, each new behavior must be

modeled from scratch, while if we maintained the hierarchy, then the vocabulary of local motions learnt at the lower tiers of the hierarchy can be used to simplify the learning problem for new behaviors. [50] provides a detailed characterization of the limitations and expressive power of such hierarchical Markov models while [91] describes a methodology to analyze such linear hybrid dynamical systems. The hierarchical model also assumes that the various tiers of the hierarchy are semi-independent and that the particular current motion state does not have a direct influence on the behavior in subsequent frames. This would not necessarily be true, since particular behaviors might have specific end patterns of motion. In future, we would like to study how one might introduce such state based transition characteristics into the behavior model, while retaining both the hierarchical nature of the model itself and keeping complexity of the model manageable.

4.3.5 Learning the parameters of the Model

Learning the behavior model is now equivalent to learning the autoregressive parameters $A^k_{B_i}$ for $k = 1..K_i$. for each behavior B_i and also learning the transition probability matrix between behaviors given by T_B. This step can either be supervised or unsupervised.

Unsupervised Learning/Clustering

In unsupervised learning we are provided only the sequence of motion states that are exhibited by the bee for frames 1 to N, i.e., we are provided with a time series $s_1, s_2, s_3, ..., s_N$, where each s_i is one of the motion states $m_1...m_4$. We are not provided with any annotation of the behaviors exhibited by the bee, i.e., we do not know the behavior exhibited by the bee in each of these frames. This is

essentially a clustering problem. A maximum likelihood approach to this clustering problem involves maximizing the probability of the state sequence given the model parameters.

$$\hat{Q} = \arg\max_{Q} P(s_{1:N}/Q); \tag{4.5}$$

where $Q = [A^k_{B_i}]^{i=1:B}_{k=1..K_i}$ represents the model parameters. Such an approach to learning the parameters of a mixture model for a "juggling sequence" was shown in [15]. They show how expectation-maximization(EM) can be combined with CONDENSATION to learn the parameters of a mixture model. But as they point out there is no guarantee that the clusters found will correspond to semantically meaningful behaviors. For our specific problem of interest, viz., tracking and annotating activities of insects we would like to learn models for specific behaviors like waggle dance. Therefore, we use a supervised method to learn the parameters of each behavior. Nevertheless, unsupervised learning is useful while attempting to learn anomalous behaviors and we will revisit this issue later.

Supervised Learning

Since it is important to maintain the semantic relationship between learnt models and actual behaviors exhibited by the bee, we resort to supervised learning of the model parameters. For a small training database of videos of bee dances, we obtain manual tracking and labeling of both the motion states and the behaviors exhibited, i.e., for a training database we first obtain the labeling over the three tiers of the hierarchy. For each frame j of the training video we have the position X^j, the motion state m^j and the behavior B^j.

Learning Dynamics: The first tier of the three tier model involves the local motion states like moving straight, turning, waggle and motionless. As described in

(4.1) and (4.2), each of these local motion states is modeled either using a Gaussian or using a mixture of Gaussians. The mean and the variance of the corresponding Normal distributions are directly learnt from the training as

$$\begin{aligned}
\hat{\mu}_{mi} &= E[(X^j - X^{j-1})|m^j = i] && (4.6)\\
&= \frac{1}{N_i} \sum_{j=1,2,...N}^{m^j=mi} (X^j - X^{j-1}) && (4.7)\\
\Sigma_{mi} &= E[(X^j - X^{j-1} - \mu_{mi})(X^j - X^{j-1} - \mu_{mi})^T] && (4.8)\\
&= \frac{\sum_{j=1,2,...N}^{m^j=mi} (X^j - X^{j-1} - \hat{\mu}_{mi})(X^j - X^{j-1} - \hat{\mu}_{mi})^T}{N_i - 1} && (4.9)
\end{aligned}$$

where, the summations are carried out only for the frames in which the annotated motion state for that frame is mi, and the total number of such frames is denoted by N_i. In the case of a mixture of Gaussians model (for turning), we use the EM algorithm to learn the model parameters. In practice, learning dynamics is the simplest of the three tiers of learning.

Learning Behavior: The second tier of the hierarchy involves the Markov model for each behavior. For the i^{th} behavior B_i we learn the model parameters using maximum likelihood estimation. As an example let us assume that the insect exhibited behavior B_i for frame 1 to N. In the training database, we have obtained a corresponding sequence of motion states $s_1, s_2, s_3, ..., s_N$ where s_j is one of the four possible motion states (straight,turn,waggle,motionless) exhibited in frame j. We can learn the model parameters of the Markov model for behavior B_i by

$$\hat{Q}_i = \arg\max_{Q_i} P(s_{1:N}/Q_i); \tag{4.10}$$

where $Q_i = [A^k_{B_i}]^{k=1..K_i}$ represents the model parameters for behavior B_i. In our current implementation, we have modeled behaviors for waggle dance, round dance and a stationary bee. We have used Markov models of order 1, so that we need to only estimate the transition probabilities between each motion state. These are

estimated as given below.

$$\hat{A}_{B_i}(l,k) = E(P(s_t = k/s_{t-1} = l)) \quad (4.11)$$

$$= \frac{N_{kl}}{N_l} \quad (4.12)$$

where, E is the expectation operator, N_l is the number of frames in which the annotated motion state was ml and N_{kl} is the number of times in which the annotated motion state mk appeared immediately after motion state ml. Note that since this step of the learning procedure concerns only a particular behavior B_i, only the frames whose annotated behavior is B_i are taken into account. Learning the model parameters of a particular behavior depends upon two factors -the inherent variability in the behavior and the amount of training data available for that particular behavior. Some behaviors have significant variability in their executions and learning model parameters for these behaviors could be unreliable. Moreover, some behaviors are uncommon and therefore, the amount of training data available for these behaviors might be too little to accurately learn the model parameters. Experiments to indicate the minimum number of frames one needs to observe a behavior before one can learn the model parameters are shown in Section 4.3.7.

Switching between behaviors The third tier of the model involves the switching between behaviors. The switching between behaviors is also modeled as being Markovian with the transition matrix denoted as T_B. The transition matrix T_B can be learned as,

$$\hat{T}_B(l,k) = E[B^j = k | B^{j-1} = l]. \quad (4.13)$$

Learning the switching model is the most challenging part of the learning phase. Firstly, within a given length of training data, there might be very few transitions

observed and therefore, sufficient data might not be available to learn the switching matrix T_B accurately. Secondly, there is really no particular ethological justification to model the transitions between behaviors using a Markov model, though in practice the model seems adequate. Therefore, once we learn the transition matrix T_B from the training data, we also ensure that every transition is possible, i.e., $T_B(l,k) \neq 0 \forall (l,k)$, by adding a small value ϵ to every element in the matrix and then normalizing the matrix so that it still represents a transition probability matrix (sum of each row = 1).

4.3.6 Discriminability among Behaviors

The disadvantage in using supervised learning is that since learning for each behavior is independent of others, there is no guarantee that the learnt models are sufficiently distinct for us to be able to distinguish among different behaviors. There is reason, however, to believe that this would be the case since in actual practice these behaviors are distinct enough. Nevertheless we need some quantitative measure to characterize the discriminability between models. This would be of great help especially when we have several behaviors.

Rabiner-Juang Distance

There are several measures for computing distances between Hidden Markov Models. In particular, one distance measure that is popular is the Rabiner-Juang distance [83]. But such a distance measure is based on the KL distance and therefore captures the distance between the asymptotic observation densities. However, in actual practice, we are always called upon to recognize the source model using observation or state sequences of finite length. In fact, in our specific scenario, we

need to re-estimate the behavior exhibited by the bee every few frames. Therefore, in such situations we need to know how long a state/observation sequence is required before we can disambiguate between two models.

Probability of N-Misclassification

Suppose we have D different Markov models $M_1..M_D$, M_i being of order K_i. We define the Probability of N-Misclassification for Model M_i as the probability that a state sequence of length N that is generated by model M_i is misclassified to some model M_j, $j \neq i$ using a maximum likelihood rule.

$$P_{M_i}(NMiscl) = 1 - \sum_{s_{1:N}} P(s_{1:N}/M_i) I(s_{1:N}, i) \tag{4.14}$$

where the summation is over all state sequences of length N and $I(s_{1:N}, i)$ is an indicator function which is 1 only when $P(s_{1:N}/M_i)$ is greater than $P(s_{1:N}/M_j)$ for all $j \neq i$. The number of terms in the summation is S^N where S is the number of states in the state space. Even for moderate sizes of S and N, this is difficult to compute. But the summation will be dominated by few of the most probable state sequences. So a tight lowerbound can be obtained by Monte Carlo methods of sampling. An approximation to Probability of N-Misclassification can also be obtained using Monte-Carlo sampling methods. This is done by generating K independent state sequences $Seq_1, Seq_2..Seq_K$ each of length N randomly using model M_i. For reasonably large K,

$$P_{M_i}(NMiscl) \approx 1 - 1/K \sum_{k=1,...K} I(Seq_k, i) \tag{4.15}$$

Figure 4.4 shows the Probability of N-Misclassification for the three modeled behaviors Waggle, Round and the Stationary bee for different values of N. We choose a window length $N = 25$ which provides us with sufficiently low misclassification

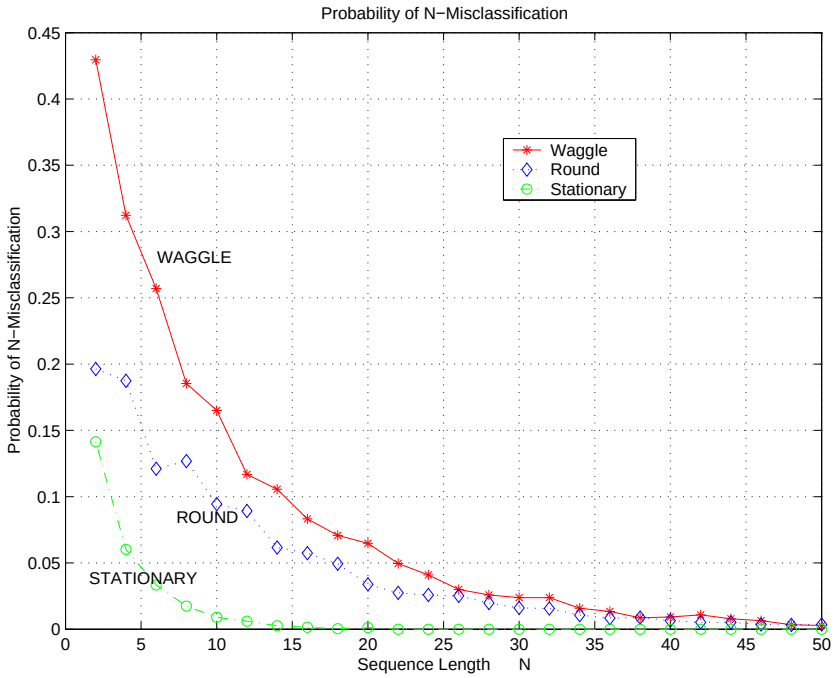

Figure 4.4: Probability of N-Misclassification

errors while being small enough compared to average length of behaviors so as to not smooth across behaviors.

4.3.7 Detecting/Modeling Anomalous Behavior

A change in behavior of the insect would result in the behavior model not being able to explain the observed motion of the insect. When this happens we need to be able to detect and characterize these abnormal behaviors so that the tracking algorithm is able to continue to maintain track. A change in behavior can either be slow or drastic. We use the observation likelihood and the ELL (Expected negative log-likelihood of the observation given the model parameters) as proposed in [157] [156] in order to detect drastic and slow changes in behavior.

Drastic Change: When there is a drastic change in the behavior of the insect,

this would cause the tracking algorithm to lose track. Once it loses track, the image within the shape model of the bee does not resemble the bee anymore. Therefore, the observation likelihood decreases rapidly. This can be used as a statistic to detect drastic changes in behavior. Once the anomalous behavior is detected, it would of course be left to the expert to manually identify and characterize the newly observed behavior.

Slow Change: When the change in system parameters is slow, i.e., the anomalous behavior is not drastic enough to cause the tracker to lose track, we use a statistic very closely related to the ELL proposed in [157] [156]. Let us assume that we have modeled behavior $M0$. Supposing the actual behavior exhibited by the insect is $M1$. We are required to decide whether the behavior exhibited is $M0$ or not with knowledge of the state sequence $x_{1:N}$ alone. Let Hypothesis $H0$ be that the behavior being exhibited is $M0$ while Hypothesis $H1$ be that the behavior exhibited is not $M0$, i.e.,$\overline{M0}$. The likelihood ratio test for such a hypothesis is given below. The state sequence $x_{1:N}$ was generated by model $\overline{M0}$ iff,

$$\frac{P(\overline{M0}/x_{1:N})}{P(M0/x_{1:N})} \geq \eta \qquad \eta > 0 \tag{4.16}$$

$$\Rightarrow \frac{1 - P(M0/x_{1:N})}{P(M0/x_{1:N})} \geq \eta \qquad \eta > 0 \tag{4.17}$$

$$\Rightarrow P(M0/x_{1:N}) \leq 1/(\eta + 1) \tag{4.18}$$

$$\Rightarrow P(x_{1:N}/M0)P(M0)/P(x_{1:N}) \leq 1/(\eta + 1) \tag{4.19}$$

$$\Rightarrow P(x_{1:N}/M0) \leq \beta \quad \beta > 0 \tag{4.20}$$

$$\Rightarrow D = -log(P(x_{1:N}/M0)) \geq T \quad T = -log(\beta) \tag{4.21}$$

where, D is the decision statistic and T is the decision threshold.

When the bee exhibits an anomalous behavior, then the likelihood that the state sequence observed was generated by the original model decreases as shown

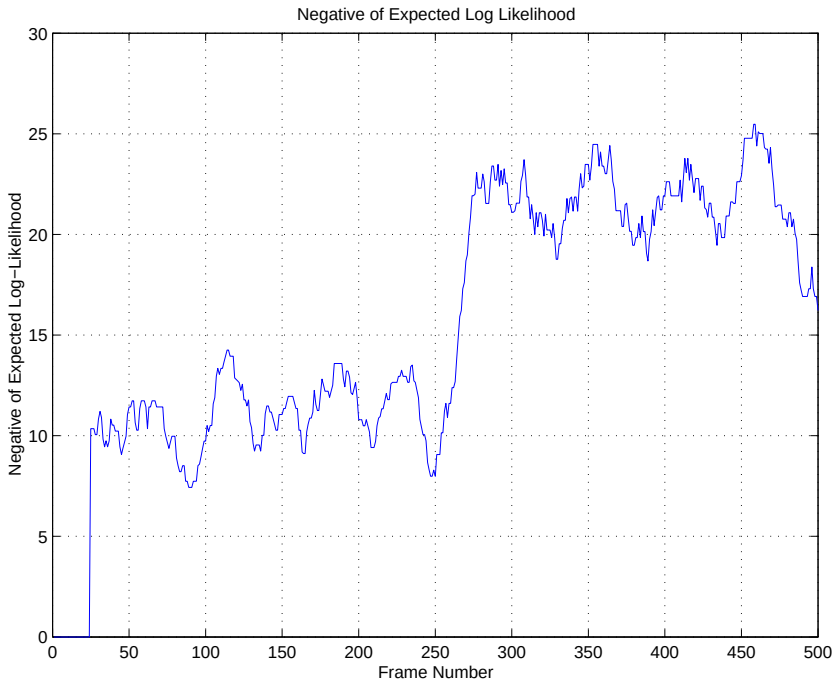

Figure 4.5: Abnormality Detection Statistic

above. Therefore, we can use D as a statistic to detect slow changes. When D increases beyond a certain threshold T we detect anomalous behavior. Once slow changes are detected, they can then be automatically modeled. This can be done by learning a mixture model for the observed state sequence using principles outlined in [15].

Since we did not have any real video sequence of an abnormal behavior we performed an experiment on synthetic data. We generated an artificial sequence of motion states for 500 frames. The first 250 frames correspond to the model learnt for the waggle dance. The succeeding 250 frames were from a Markov model of order 1, with transition probability matrix A. We computed the negative log-likelihood of the windowed state sequence, with a window length of 25. This statistic D is shown in figure 4.5. Changes in model parameters are clearly

visible at around frame 250 resulting in an increase in the negative log-likelihood (equivalent to an exponential decrease in the probability of the windowed sequence being generated from the waggle model). The anomalous behavior was automatically detected at frame 265. Moreover, we also used the next 150 frames to learn the parameters of the anomalous model(A). The estimated transition probability matrix($\hat{A}$) was very close to the actual model parameters.

$$A = \begin{pmatrix} .30 & .30 & .20 & .20 \\ .20 & .25 & .25 & .30 \\ .80 & .10 & .05 & .05 \\ .50 & .10 & .20 & .20 \end{pmatrix} \hat{A} = \begin{pmatrix} .30 & .22 & .23 & .25 \\ .30 & .18 & .22 & .30 \\ .78 & .13 & .04 & .05 \\ .47 & .06 & .28 & .19 \end{pmatrix}$$

4.4 Shape and Behavior Encoded Particle Filter

We address the tracking problem as a problem of estimating the state X_1^t given the image observations Y_1^t. Since both the state transition model and the observation model are non-linear, methods like the Kalman filter are inadequate.

The particle filter [61] [39] [76] provides a method for recursively estimating the posterior pdf $P(X_t/Y_1^t)$ as a set of N weighted particles $\{X_t^{(i)}, \pi_t^{(i)}\}_{i=1}^N$., from a collection of noisy observations $\mathbf{Y}_1^t$. The state parameters to be estimated are the position and orientation of the bee in the current frame ($\mathbf{X}$). The observation is the color image of each frame ($\mathbf{Y}_t$) from which the appearance of the bee ($\mathbf{Z}_t^{(i)}$) can be computed for each hypothesised position($\mathbf{X}_t^{(i)}$). The state transition and the observation models are given by,

$$\textit{State Transition Model: } X_t = F_B(X_{t-1}, N_t) \tag{4.22}$$

$$\textit{Observation Model: } Y_t = G(X_t, W_t) \tag{4.23}$$

where, N_t is the system noise and W_t is the observation noise. The state transition function F_B characterizes the state evolution for a certain behavior B. In usual tracking problems, the motion model is used to characterize the state transition function. In our current algorithm, the behavioral model described in Section 3.1 is used as the state transition function. Therefore, the state at time t, (X_t) depends upon the state at the previous frame (X_{t-1}), the behavioral model and the system noise. The observation function G models the appearance of the the bee (in the current frame) as a function of its current position(state X_t), and observation noise. Once such a description for state evolution has been made, the particle filter provides a method for representing and estimating the posterior pdf $P(X_t/Y_1^t)$ as a set of N weighted particles $\{X_t^{(i)}, \pi_t^{(i)}\}_{i=1}^N$. Then the state X_t can be estimated as the MAP estimate as given below,

$$\hat{X}_t^{MAP} = \arg\max_{X_t} \pi_t^{(i)} \tag{4.24}$$

The complete algorithm is given below

1. **Initialize** the tracker with a sample set according to a prior distribution $p(X_0)$.
2. **For** Frame $= 1, 2, ...$
   (a) **For** sample $i = 1, 2, 3, ...N$
      - **Resample** $X_{t-1} = \{\pi_{t-1}^{(i)}\}$
      - **Predict** the sample $X_t^{(i)}$ by sampling from $F_B(X_{t-1}^{(i)}, N_t)$ where F_B is a Markov model for the behavior B estimated in the previous frame.
      - **Compute Weights** for the particle using the likelihood model i.e., $\pi_t^{(i)} = p(Y_t/X_t^{(i)})$. This is done by first computing the predicted appearance of the bee using the function G and then evaluating its probability from the observation noise model.
   (b) **Normalize** the weights using $\pi_t^{(i)} = \pi_t^{(i)} / \sum_{i=1}^N \pi_t^{(i)}$ so that the particles represent a probability mass function.

(c) **Estimate** the MAP or MMSE estimate of the state X_t. using the particles and their weights.

(d) **Compute** the maximum likelihood estimate ($\hat{s}^t$)for the current motion state given the position and orientation in the current and previous frame.

(e) **Estimate** the behavior of the bee using a ML estimate from the various behavior models as $\hat{B} = \arg\max_j P(\hat{s}^t_{t-24}/B_j)$., where $B_j for j = 1, 2, ..$ indicate the behaviors modeled.

4.4.1 Prediction and Likelihood Model

In typical tracking applications it is customary to use motion models for prediction [76] [89] [13] [179]. We use behavioral models in addition to motion models. The use of such models for prediction improves tracking performance significantly.

Given the location of the bee in the current frame (X_t) and the image observation given by (Y_t), we first compute the appearance (Z_t) of the bee in the current frame (i.e., the color image of the three ellipse anatomical model of the bee). Therefore, given this appearance ($Z_t^{(i)}$) for each hypothesised position $X_t^{(i)}$, the weight for the i^{th} particle ($\pi_t^{(i)}$) is updated as

$$\pi_t^{(i)} = p(Y_t/X_t^{(i)}) = p(Z_t^{(i)}/X_t^{(i)}) \tag{4.25}$$

where, Y_t is the observation. Since the appearance of the bee changes drastically over the video sequence, we use an appearance model consisting of multiple color exemplars($A_1, A_2, .., A_5$). The RGB components of color are treated independently and identically. The appearance of the bee in any given frame is assumed to be Gaussian centered around one of these five exemplars, i.e.,

$$P(Z_t) = \frac{1}{5}\sum_{i=1}^{i=5} 0.2 \;\; N(Z; A_i, \Sigma_i) \tag{4.26}$$

where $N(Z; A_i, \Sigma_i)$ stands for the Normal distribution with mean A_i and covariance Σ_i. In practice, we modeled the covariance matrix as a diagonal matrix with equal elements on the diagonal, i.e., $\Sigma_i = \sigma I$, where I is the identity matrix. The mean observation intensities $A1 - A5$ are learnt by specifying the location of the bee in 5 arbitary frames of the video sequence. In practice, we also used 4 of these 5 exemplars from the training database, while the 5^th exemplar was estimated from the initialization provided in the first frame of the current video sequence. In either case the performance was similar. For extremely challenging sequences, with large variations in lighting the former method performed better than the latter.

4.4.2 Inference of Dynamics, Motion and Behavior

Inference on the three tier hierarchical model is performed using a greedy approach. The inference for the lower tiers is first performed independently and these estimates are then used in the inference for the next tier. Estimating the current position and orientation of the insect ($\hat{X}^t$) is performed using a particle filter with observation and state transition models as described in the previous section. Once the position and the orientation are estimated using the particle filter, we then use these estimates to infer about the current motion state. The maximum likelihood estimate for the current motion state given the position and orientation in the current and previous state is estimated as

$$\hat{s}^t_{ML} = \arg \max_{mi \; i=1,2,3...} P(\hat{X}^t - \hat{X}^{t-1} | s^t = mi) \tag{4.27}$$

Finally, we also need to estimate the behavior of the insect in the current frame. Once again, we assume that the inference for the lower tiers has been completed and based on the estimated motion states $\hat{s}^{1:t}$, we infer the maximum likelihood estimate for the current behavior. In order to perform this, we also need to decide

an appropriate window length W. From section 4.3.7, we see that a window length W of 25 is a good trade-off between recognition performance and smoothing across behavior transitions. Therefore, we do a maximum likelihood estimation for the behavior using a window length of 25 frames as

$$\hat{B} = \arg\max_j P(\hat{s}_{t-W+1}^t | B_j). \tag{4.28}$$

Since the behavior model B_j, is a simple Markov model of order 1 given by the transition matrix T_{B_j}, this maximum likelihood estimate is easily obtained as

$$\begin{aligned} \hat{B} &= \arg\max_j P(\hat{s}_{t-W+1}^t | T_{B_j}) && (4.29) \\ &= \arg\max_j \prod_{i=1,2,..W} T_{B_j}(\hat{s}_{t-i}, \hat{s}_{t+1-i}) && (4.30) \end{aligned}$$

4.5 Experimental Results

4.5.1 Experimental Methodology

For a training database of videos, manual tracking was performed, i.e., at each frame the position, motion and the behavior of the bee was manually labeled. Following the steps outlined in Section 4.3.5, the model for dynamics, behavior and the behavior transitions was learnt. During the test phase, for every test video sequence, the user first identifies the bee to be tracked and initializes the position of the bee by identifying four extreme points on the abdomen, thorax and head respectively. Then the tracking algorithm uses this initialization with a suitably chosen variance, as the prior distribution $p(X_0)$ and automatically tracks both the position and the behavior of the bee as described in Section 4.4. This is a significant difference in experimental methodology from most other previous work. In [47], they first obtain manually tracked data for the entire video sequence to be analysed.

Then the Markov model is used in order to classify the various behaviors. In other related work, like [116] and [117], for each test video sequence, the tracking is independently accomplished using a tracking algorithm [89], that has no knowledge of the behavior models. Once the entire video sequence is tracked, then analysis of the tracked data is performed using specific behavior models. The training phase for our algorithm is similar to those in [47], [116] and [117] in the sense that all these algorithms use some kind of labeled data to learn the model parameters for each behavior. But, our algorithm differs from all the others mentioned above in that the behavior model thus learnt is used as a prior for tracking, thus enhancing the tracking accuracy. Moreover, this also means that manual labeling is required only for the training sequences and not for any of the test videos.

4.5.2 Relation to Previous Work

Previous work in tracking and analyzing the behaviors of bees, have dealt either with the visual tracking problem [89] or with that of accurately modeling and analyzing the tracked trajectories of the insects [116] [117] [47]. This is the first study that tackles both tracking and behavior modeling in a closed loop manner. By closing the loop, and enabling the tracking algorithm to be aware of the behavior models, we have improved the tracking performance significantly. Experiments in the next section will demonstrate the improvement of the tracking performance for two video sequences that have drastic motions. Once the results of the tracking algorithm are available, one can in principle analyze the tracked trajectories using any appropriate behavior model - the hierarchical Markov model or the p-SLDS. In all the experiments reported in this paper, we have used the hierarchical Markov motion model to analyze the behavior of the bees.

4.5.3 Tracking dancing bees in a hive

We conducted tracking experiments on video sequences of bees in a hive. In all the experiments reported the training data and the test data were mutually exclusive. In the videos, the bees exhibited three behaviors- the waggle dance, the round dance and a stationary bee. In all our simulations we used 300 to 600 particles. The video sequences ranged between 50 frames to about 700 frames long. It is noteworthy that when a similar tracking algorithm without a behavioral model was used for tracking, it lost track within 30-40 frames (See Table 4.1 for details). With our behavior-based tracking algorithm, we were able to track the bees during the entire length of these videos. We were also able to extract parameters like the orientation of the various body parts during each frame over the entire video sequences. We used these parameters to automatically identify the behaviors. We also verified this estimate manually and found it to be robust and accurate.

Figure 4.6 shows the structural model of the tracked bee superimposed on the original image frame. In this particular video, the bee was exhibiting a waggle dance. The results are best viewed in color since the tracking algorithm had color images as observations. The figure shows the top five tracked particles (blue being the best particle and red being the fifth best particle). As is apparent from the sample frames the appearance of the dancer varies significantly within the video. These images display the ability of the tracker to maintain track even under extreme clutter and in the presence of several similar looking bees. Frames 30-34 show the bee executing a waggle dance. Notice that the abdomen of the bee waggles from one side to another.

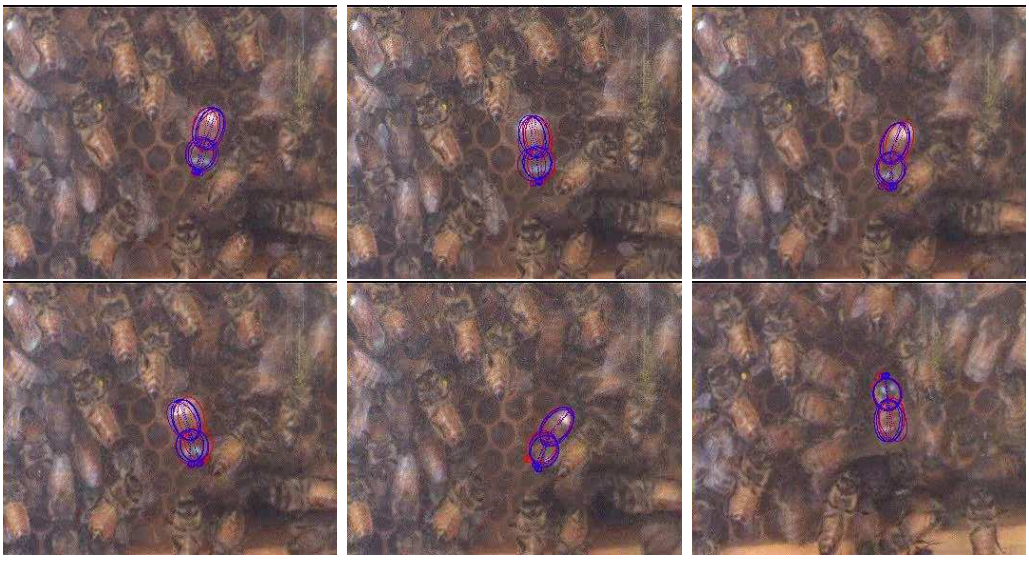

Figure 4.6: Sample Frames from a tracked sequence of a bee in a beehive. Images show the top 5 particles superimposed on each frame. Blue denotes the best particle while red denotes the fifth best particle. Frame Numbers row-wise from top left :30, 31, 32, 33, 34 and 90. Figure best viewed in color.

Occlusions

Figure 4.7 shows the ability of the behavior based tracker to maintain track during occlusions in two different video sequences. There is significant occlusion in frames 170, 172 and 187 of video sequence 1. In fact, in fame 172, occlusion forces the posterior pdf to become bimodal (another bee in close proximity). But we see that the track is regained when the bee emerges out of occlusion in frame 175. In frame 187, we see that the thorax and the head of the bee are occluded while the abdomen of the bee is visible. Therefore the estimate of the abdomen is very precise (all five particles shown indicate the same orientation of abdomen). Since the thorax is not visible we see that there is a high variance in the estimate of the orientation of the thorax and the head. Structural modeling has ensured that, in

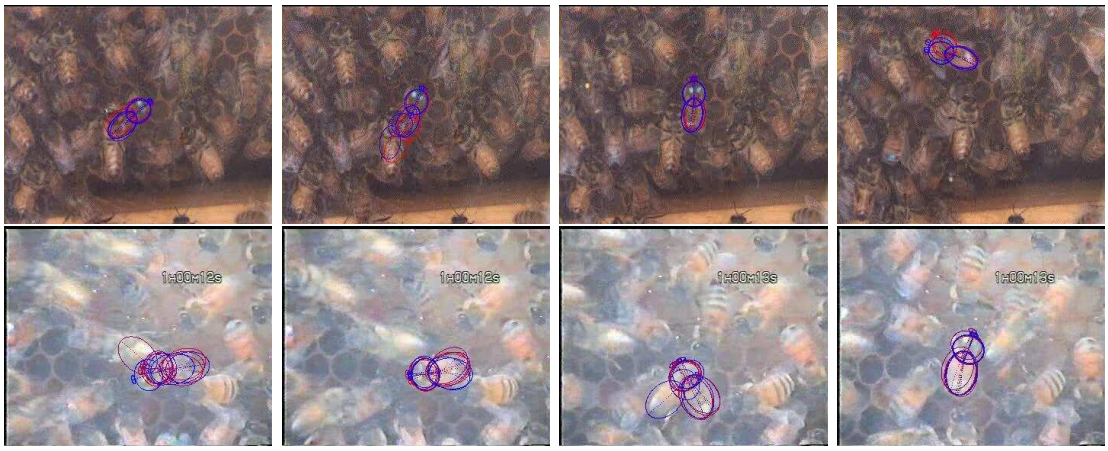

Figure 4.7: Ability of the behavior based tracker to maintain tracking during occlusions in two different video sequences. Images show the top 5 particles superimposed on each frame- Blue denotes the best particle and red denotes the fifth best particle. Row 1: Video 1- Frames 170, 172, 175 and 187 and Row 2: Video 2- Frames 122, 123, 129 and 134. Figure best viewed in color.

spite of the occlusion, only physically realizable orientations of the thorax and the head are maintained. In frame 122 of video sequence 2, we see that another bee completely occludes the bee being tracked. This creates confusion in the posterior distribution of the position and orientation. But, behavior modeling ensures that most particles still track the correct bee. Moreover, at the end of occlusion in frame 123, the track is regained. Frame 129 in video sequence 2, shows another case of severe occlusion. But, once again, we see that the tracker maintains track during occlusion and immediately after occlusion (Frame 134). Thus behavior modeling helps to maintain tracking under extreme clutter and severe occlusions.

Table 4.1: Comparison of our Behavior based tracking algorithm(BT) with Visual tracking (VT) [179] and the same visual tracking algorithm enhanced with our shape model (VT-S)

Video Name	Video 1			Video 2		
Total Frames	550			200		
Algorithm	VT	VT-S	BT	VT	VT-S	BT
Number of Particles	500	500	500	500	500	500
Successful Tracking	No	No	Yes	No	No	Yes
Number of Missed Tracks	14	10	0	5	5	0
Average No. of Frames Tracked	37	50	550	33	33	200

4.5.4 Importance of Shape and behavioral Model for Tracking

To quantify the importance of the shape and the behavioral model in the above-mentioned tracking experiments, we also implemented another recent and successful tracking algorithm also based on a particle-filter based inference. We implemented the visual tracking algorithm based on an adaptive appearance model described in [179]. We also implemented a minor variation of this algorithm by incorporating our shape model within their framework. In either case we spent a significant amount of time and effort in varying the parameters of the algorithm so

as to obtain the best possible tracking results with these algorithms. We compare the performance of our tracking algorithm to the two approaches mentioned above on two different video sequences in Table 4.1. Both these videos consisted of a hand-held camera held over the vertical face of the bee-hive. There were several bees within the field of view of each of these videos, but we were interested in tracking the dancing bees in both videos. So, we initialized the tracking algorithm on the dancers in all these experiments. Moreover, these video sequences were also specifically chosen since the bees exhibited drastic motion changes during the videos and the illumination and lighting remained fairly consistent during the course of these videos. This gives us a nice testbed to evaluate the performance of the shape and behavior model fairly independent of other challenges in tracking like illumination. The incorporation of the shape constraints improves the performance of the tracking algorithm showing that an anatomically correct model improves tracking performance. We declared that a tracking algorithm "Lost Track" when the distance between the estimated position of the bee and the actual position of the bee on the image was greater than half the length of the bee. We see that while the proposed tracking algorithm was able to successfully track the bee over the length of the entire video sequences, the other approaches implemented were not able to. The table also clearly shows that the behavior aided tracking algorithm that we propose significantly outperforms the adaptive appearance based tracking [179].

4.5.5 Comparison with Ground Truth

We validated a portion of the tracking result by comparing it with a "ground truth" track obtained using manual ("point and click") tracking by an experienced human observer. We find that the tracking result obtained using the proposed

method is very close to manual tracking. The mean differences between manual and automated tracking using our method are given in Table 4.2. The positional differences are small compared the average length of the bee, which is about 80 pixels (from front of head to tip of abdomen).

Table 4.2: Comparison of our tracking algorithm with Ground Truth

	Average positional difference between Ground Truth and our algorithm
Center of Abdomen	4.5 pixels
Abdomen Orientation	0.20 radians (11.5 deg)
Center of Thorax	3.5 pixels
Thorax orientation	0.15 radians (8.6 deg)

4.5.6 Modes of failure

Even in the presence of the improved behavior model based tracking algorithm, there are some extremely challenging video sequences, where the improved tracking algorithm resulted in some missed tracks. The primary modes of failure are

- Illunination: We are interested in studying and analyzing bee dances. Bee dances are typically performed in the dark environment of the bee-hive. Since the bees typically prefer to dance only in minimal lighting, some of the videos end up being quite dark. Moreover, there are also significant illumination changes depending upon the exact position of the dancer on the

bee hive. These illumination changes posed the most significant challenge for the tracking algorithm and most of the tracking failures can be attributed to illumination based challenges in tracking. Even in such videos, the tracking algorithm with the behavior and anatomical model, outperforms the adaptive appearance based tracking algorithm [179]. Recently, a lot of research effort has been invested in studying and developing appearance models that are either robust or invariant to illumination changes [52] [173]. Augmenting the appearance model with illumination invariant appearance models might reduce some of the errors caused due to illumination changes. Since the focus of this work was on behavior modeling, we did not systematically analyze the effect of incorporating such illumination invariant appearance models in our algorithm.

- Occlusions: Another reason for some of the observed tracking failures, is occlusions. The bee hive is full of several bees which are very similar in appearance. Sometimes, the dancing bee disappears below other bees and then reappears after a few frames. As described in Section 4.5.3, when the dancing bee is occluded for a relatively small number of frames, the algorithm is able to regain track when the bee emerges out of occlusions (refer Figure 4.7). But in some videos, the dancing bee remains occluded for over 30 frames or more. during such cases of extreme occlusions, the tracking algorithm is unable to regain track. During such cases of extreme occlusions, the only reasonable way to regain track would be to design an initialization algorithm that can potentially discover dancing bees in a hive. This would be an extremely challenging task, considering the complex nature of motions in a bee hive and the fact that there are several moving bees in every frame of the

video. In practice, it might be a good idea to perform manual reinitialization in such videos.

4.5.7 Estimating Parameters of the Waggle Dance

Foraging honeybees communicate the distance, direction and the attractiveness of the food source through the waggle dance. The details of the waggle dance were discussed in detail in Section 4.1. The duration of the waggle portion of the dance and the orientation of the waggle axis are some of the parameters of interest while analyzing the bee dances. The duration of the waggle portion of the dance may be estimated by carefully filtering the orientation of the thorax and the abdomen of a honeybee as it moves around in its hive. Moreover, the orientation of the waggle axis can also be estimated from the orientation of the thorax during the periods of waggle.

Figure 4.8 shows the estimated orientation of the abdomen and the thorax in a video sequence of around 600 frames. The orientation is measured with respect to the vertically upward direction in each image frame and a clockwise rotation would increase the angle of orientation while an anticlockwise rotation would decrease the angle of orientation.

The waggle dance is characterized by the central waggling portion which is immediately followed by a turn, a straight run another turn and a return to the waggling section as shown in Figure 4.3. After every alternate waggling section the direction of the turning is reversed. This is clearly seen in the orientation of both abdomen and the thorax. The sudden change in slope (from positive to negative or vice-versa) of the angle of orientation denotes the reversal of turning direction. During the waggle portion of the dance, the bee moves its abdomen from one side

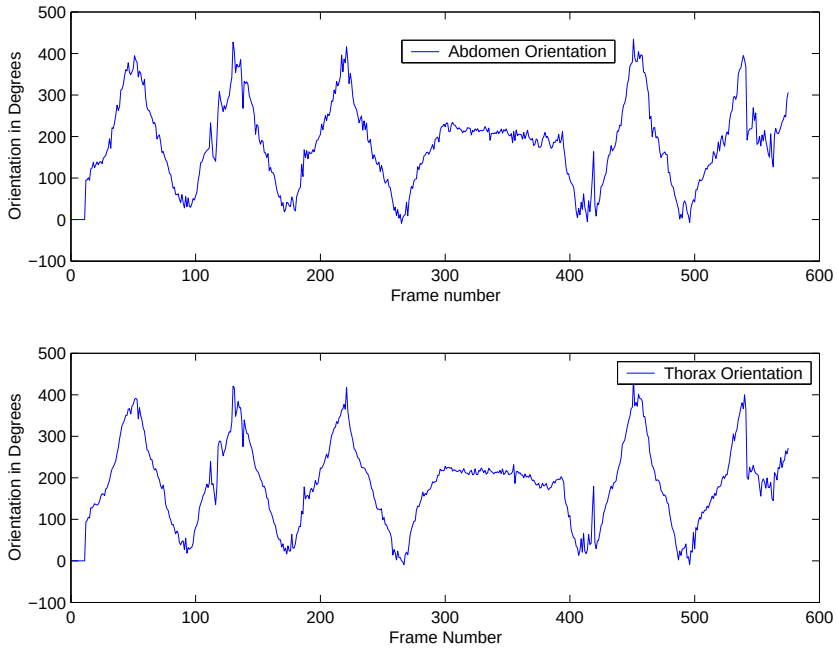

Figure 4.8: The orientation of the Abdomen and the Thorax of a bee in a video sequence of about 600 frames

to another while continuing to move forward slowly. The large local variation in the orientation of the abdomen just before every reversal of direction shows the waggling nature of the abdomen. Moreover, the average angle of the thorax during the waggle segments denotes the direction of the waggle axis.

In order to estimate the parameters of the waggle dance, we use some heuristics described below. During the waggling portion of the dance, the bee moves its abdomen from one side to another in the direction transverse to the direction of motion. The average absolute motion of the center of the abdomen about an axis transverse to the axis of motion is used as a waggle detection statistic. When this statistic is large then the probability of waggle during that particular frame is large.

Table 4.3: Comparison of Waggle Detection with hand labeling by expert

	Automated Labeling (Frame Numbers)	Expert Labeling (Frame Numbers)
Waggle 1	46 - 55	46 - 56
Waggle 2	88 - 95	89 - 97
Waggle 3	127 - 141	127 - 140
Waggle 4	171 - 180	171 - 181
Waggle 5	210 - 222	211 - 222
Waggle 6	255 - 274	257 - 274
Waggle 7	406 - 424	407 - 423
Waggle 8	444 - 461	444 - 461
Waggle 9	486 - 502	486 - 502
Waggle 10	532 - 543	534 - 544

Moreover, we also recognize that the waggle portion of the dance is followed by a change in the direction of turning. Therefore, only those frames that are followed by a change in direction of turning and have a high 'waggle detection statistic' are labeled as waggle frames. Once the frames in which the bee waggles are estimated, it is then relatively straightforward to estimate the waggle axis. The waggle axis is estimated as the average orientation of the thorax during a single waggle run. Table 4.3 shows the frames that were detected as waggle frames automatically. We also hand-labeled the same video sequence by an expert. The Table also shows the frames that were labeled as 'waggle' by the expert. There were a total of 138 frames that were labeled as 'waggle' by the expert. Of these 138 frames, 133 frames were correctly labeled automatically using the procedure described above.

4.6 Conclusions and Future Work

We proposed a method using behavioral models to reliably track the position/orientation and the behavior of an insect and applied it to the problem of tracking bees in a hive. We also discussed issues in learning models, discriminating between behaviors and detecting and modeling abnormal behaviors. Specifically, for the waggle dance, we also proposed and used some simple statistical measures to estimate the parameters of interest in a waggle dance. The modeling methodology is quite generic and can be used to model activities of humans by using appropriate features. We are working to extend the behavior model by modeling interactions among insects. We are also looking to extend the method to problems like analyzing human activities.

Chapter 5

Coded Aperture Photography for Light-Field Capture

In this chapter, we describe a theoretical framework for reversibly modulating 4D light fields using an attenuating mask in the optical path of a lens based camera. Based on this framework, we present a novel design to reconstruct the 4D light field from a 2D camera image without any additional refractive elements as required by previous light field cameras. The patterned mask attenuates light rays inside the camera instead of bending them, and the attenuation recoverably encodes the rays on the 2D sensor. Our mask-equipped camera focuses just as a traditional camera to capture conventional 2D photos at full sensor resolution, but the raw pixel values also hold a modulated 4D light field. The light field can be recovered by rearranging the tiles of the 2D Fourier transform of sensor values into 4D planes, and computing the inverse Fourier transform. In addition, one can also recover the full resolution image information for the in-focus parts of the scene.

5.1 Introduction

The trend in computational photography is to capture more optical information at the time of capture to allow greater post-capture image processing abilities. The pioneering work of Ng *et al.* [113] has shown a hand-held plenoptic camera where the user can adjust focus and aperture settings after the picture has been taken. The key idea is to capture the entire 4D light field entering via the lens and incident on the camera sensor. In a conventional camera, the sensed 2D image is a 2D projection of the 4D light field [114] and it is not possible to recover the entire 4D light field. Using a clever arrangement of optical elements, it is possible to re-bin the 4D rays and capture them using a 2D sensor [58, 113]. These lens arrays perform the optical implementation of the two plane parameterization of the light field [62, 96].

Eventually, advances in computational photography may free us from nearly all of the adjustments, settings, and hard choices a photographer must make before "taking the picture". Recent publications explain ways to change long-standing photographic procedures so that we can re-light, re-color [5, 45, 128], re-expose, re-position, re-arrange [3], re-time [134], and gently re-animate our captured visual experiences long after the time of capture itself. We are particularly interested in how conventional single-lens film-like cameras might better capture what we want to see when we press the camera's shutter release.

For example, inspired by Adelson's early plenoptic camera [2], Ng *et al.* [113] and Georgiev *et al.* [58] both developed a hand-held SLR camera that gathers a fully 4D light field in a single shutter-click. 'Re-binning' sensor data from these cameras can approximate the output of a conventional 2D camera, but it also allows users to modify their focussing distances, change the depth of focus (aperture), and

make mild viewpoint changes. This adjustability comes at a high cost in image resolution, however. Each camera uses clever sets of lens elements to arrange the 4D set of rays that enter the camera into an interleaved set of 'sub-images' on the sensor, and both apply the 2-plane parameterization introduced with lightfields and lumigraphs [62, 96]. The number of interleaved images divides the resolution of each; Ng's 16Mpixel camera achieves fine angular resolution (14x14) but modest spatial resolution (320x240), while Georgiev *et al.* chose lower angular resolution and higher spatial resolution. This tradeoff is difficult to modify for either camera design, because it would require precise replacements for lens arrays.

However, optical re-binning of rays forces a fixed and permanent tradeoff between spatial and angular resolution via the array of lenses. In this chapter, we describe novel hybrid imaging/light field camera designs that are much more easily adjustable; users change a single attenuating mask rather than arrays of lenses. We call this *Dappled Photography*, as the mask shadows the incoming light and dapples the sensor. We exploit the fact that light rays can be linearly combined: rather than sense each 4D ray on its own pixel sensor, our design allows sensing linearly independent weighted sums of rays, rays combined in a coded fashion that can be separated by later decoding. Our mapping from 4D ray space to a 2D sensor array exploits *heterodyning* methods [49] that are best described in the frequency domain. By exploiting the modulation and convolution theorems [120] in the frequency domain, we derive simple attenuating mask elements that can be placed in the camera's optical path to achieve Fourier domain re-mapping. No additional lenses are necessary, and we can compute decoded rays as needed in software.

The mask-encoded 2D/4D hybrid camera provide: (a) 4D light field at low spatial resolution, in addition to a full resolution 2D image of the parts of the

scene that were in focus at capture time; and (b) full resolution digital refocusing for layered Lambertian scenes.

5.1.1 Contributions

We present a set of techniques to encode and manipulate useful portions of a 4D light field.

- We derive a 4D Fourier domain description of the effect of placing an attenuating mask at any position within a conventional 2D camera.
- We identify a new class of 4D cameras that re-map the Fourier transform of 4D ray space onto 2D sensors. Previous 4D cameras used 2D lens arrays to project 4D ray-space itself rather than it's Fourier transform.
- We achieve this frequency domain re-mapping using a single transmissive mask, and our method does not require additional optical elements such as lens arrays.

Heterodyne Light Field Camera: This design is based on the modulation theorem in the 4D frequency domain. We capture the light field using a 4D version of the method known as 'heterodyning' in radio. We create spectral tiles of the light field in the 4D frequency domain by placing high-frequency sinusoidal pattern *between* the sensor and the lens of the camera. To recover the 4D light field, we take the Fourier transform of the 2D sensed signal, re-assemble the 2D tiles into a 4D stack of planes, and take the inverse Fourier transform. Unlike previous 4D cameras that rely on lens arrays, this hybrid imaging/light field design does not force resolution tradeoffs for in-focus parts of the scene. The mask does not bend

rays as they travel from scene to sensor, but only attenuates them in a fine, shadow-like pattern. If we compensate for this shadowing, we retain a full-resolution 2D image of the parts of the scene that were in focus, as well as the lower-resolution 4D light field we recover by Fourier-domain decoding. A prototype for this design is shown in Figure 5.1.

5.1.2 Benefits and Limitations

Mask-based hybrid imaging/light field cameras offer several advantages over previous methods. An attenuating mask is far simpler and less costly than lenses or lens arrays, and avoid errors such as spherical, chromatic aberration, coma, and mis-alignment. Simpler mounts and flexible masks may allow camera designs that offer user-selectable masks; photographers could then select any desired tradeoff in angle vs. spatial resolution. The design of Ng *et al.* [113] matches main-lens aperture (f-stop) to the micro-lens array near the detector to avoid gaps or overlaps in their coverage of the image sensor; mask-only designs avoid these concerns. Our mask based designs also impose limitations. Masks absorb roughly 50% of usable light that enters the lens.

5.2 Basics

The Plenoptic function [1] is a 5D function (ignoring wavelength, polarization, and time) that represents the radiance in every direction (θ, ϕ), at every point (x, y, z) in free space. This function is redundant in a space free of occluders, and reduces to a 4D function called the light field [96] [62]. This light-field is a 4D quantity that completely characterizes light transport in a space free of occluding

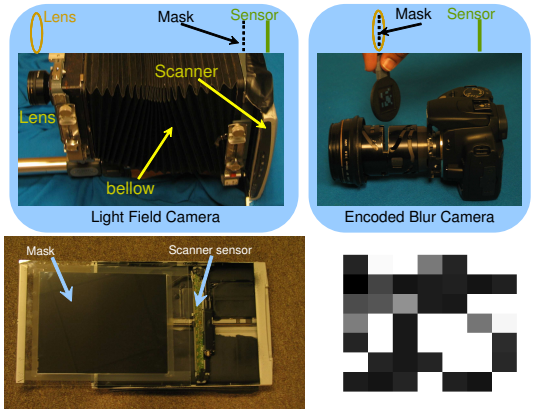

Figure 5.1: Prototype camera designs. (Top Left) Heterodyne light field camera holds a narrowband 2D cosine mask (shown in bottom left) near the view camera's line-scan sensor. (Top Right) Encoded blur camera holds a coarse broadband mask (shown in bottom right) in the lens aperture.

objects. A popular light field parameterization is the two-plane parameterization. Two parallel planes separated by a finite distance describe all the rays between them. This 4D parameterization, $L(u;v;s;t)$, is frequently used to describe and understand image formation in cameras and image based rendering techniques.

For visualization purposes, we consider a 2D light field space (LS), with one spatial dimension x and one angular dimension θ and a 1D detector as shown in Figure 5.2. We denote variables by lower case letters and their corresponding Fourier domain representations by upper case letters. Let $l(x,\theta)$ denote the 2D light field parameterized by the twin plane parameterization as shown in Figure 5.2. The θ-plane is chosen to be the plane of the main lens (or the aperture stop for cameras composed of multiple lens) of the camera. For the case of planar Lambertian object, we assume that the x-plane coincides with the object plane.

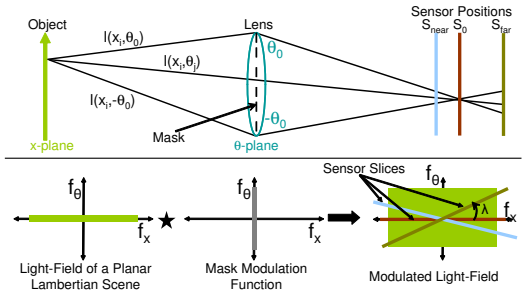

Figure 5.2: (Top) In ray-space, focused scene rays from a scene point converge through lens and mask to a point on sensor. Out of focus rays imprint mask pattern on the sensor image. (Bottom) In Fourier domain. Lambertian scenes lack θ variation & form a horizontal spectrum. Mask placed at the aperture lacks x variation & forms a vertical spectrum. The spectrum of the modulated light field is a convolution of two spectrums. A focused sensor measures a horizontal spectral slice that tilts when out-of-focus.

5.2.1 Effects of Optical Elements on the Light Field

We now discuss the effect of various optical elements such as lens, aperture and sensor to the 2D light field in frequency domain, which we refer as *Fourier domain light field space* (FLS). The (x, θ) space is referred to as the primal domain.

Sensor: The image formed on a 1D sensor is a 1D projection of the 2D light field entering the camera, which also corresponds to a slice of the light field in Fourier domain. For different focus settings, the obtained images correspond to slices at different angles/trajectories [114].

Lens: A thin lens shifts the x-plane of the light field to the conjugate plane according to the thin-lens equation. The lens also inverts the x-plane of the light field.

Aperture: The aperture of a camera acts as a limiter, allowing only the light rays that pass through the aperture to enter the camera. The light field l after

passing through the aperture is given by

$$l_a(x,\theta) = l(x,\theta)a(x,\theta), \tag{5.1}$$

where $a(x,\theta)$ is the aperture modulation function given by $a(x,\theta) = \texttt{rect}(\frac{\theta}{2\theta_0})$, and $2\theta_0$ is the size of the aperture. From (5.1), the Fourier transform of the light field after the aperture is given by

$$L_A(f_x, f_\theta) = L(f_x, f_\theta) \otimes A(f_x, f_\theta), \tag{5.2}$$

where $\otimes$ denotes convolution. L and A are the Fourier transforms of the light field (before the aperture) and the aperture modulation function respectively. Since $a(x,\theta)$ is a `rect` function,

$$A(f_x, f_\theta) = 2a_0\texttt{sinc}(2a_0 f_\theta). \tag{5.3}$$

5.2.2 FLS and Information Content in the Light Field

A light field is a 4D representation of the light rays in the free-space. A 2D sensor can only sample a 2D slice of this light field. Depending on the scene, the information content in the light field is concentrated in different parts of the light field.

Planar Lambertian Object

Let us assume that the scene being imaged consists of a planar Lambertian object at the focus plane. Since there are no angular variations in the irradiance of rays from a Lambertian object, the information content of its light field is restricted to be along the f_x axis (Figure 5.2). Thus, $L(f_x, f_\theta) = 0, \forall f_\theta \neq 0$. Since $L(f_x, f_\theta)$ is independent of f_θ and $A(f_x, f_\theta)$ is independent of f_x, from (5.2) and (5.3) we

obtain,

$$\begin{aligned} L_A(f_x, f_\theta) &= L(f_x, f_\theta) \otimes A(f_x, f_\theta), && (5.4) \\ &= L(f_x, 0)A(0, f_\theta), && (5.5) \\ &= 2a_0 L(f_x, 0)\texttt{sinc}(2a_0 f_\theta). && (5.6) \end{aligned}$$

The sensed image is a slice of this modulated light field. When the sensor is in focus, all rays from a scene point converge to a sensor pixel. Thus, the in-focus image corresponds to a slice of $L_A(f_x, f_\theta)$ along f_x ($f_\theta = 0$). Let $y(s)$ and $Y(f_s)$ denotes the sensor observation and its Fourier transform respectively. For an in-focus sensor

$$Y(f_s) = L_A(f_s, 0) = 2a_0 L(f_s, 0). \tag{5.7}$$

Thus, no information is lost when the Lambertian plane is in focus.

When the sensor is out of focus, the sensor image is a slanted slice of the modulated light field as shown in Figure 5.2, where the slant angle λ depends on the degree of mis-focus. Thus,

$$\begin{aligned} Y(f_s) &= L_A(f_s \cos\lambda, f_s \sin\lambda), \\ &= 2a_0 L(f_s \cos\lambda, 0)\texttt{sinc}(2a_0 f_s \sin\lambda) \end{aligned} \tag{5.8}$$

Thus, for out of focus setting, the light field gets attenuated by the frequency transform of the aperture modulation function, which is a sinc function for an open aperture. This explains the attenuation of the high spatial frequencies in the captured signal when the scene is out of focus. Thus, we need to modify the aperture so that the resulting aperture modulation function has a *broadband* frequency response, ensuring that high spatial frequencies are preserved in out of focus images.

Incidentally, for a pinhole camera, the aperture function is a Dirac delta function and the aperture modulation function is broadband in f_θ. This explains why the images captured via a pinhole camera are always in-focus. However, a pinhole camera suffers from severe loss of light, reducing the signal to noise ratio (SNR) of the image.

Bandlimited Light Fields

For general scenes, we assume that the light field is bandlimited to f_{x0} and $f_{\theta 0}$ as shown in Figure 5.4: $L(f_x, f_\theta) = 0 \quad \forall |f_x| \geq f_{x0}, |f_\theta| \geq f_{\theta 0}$. A traditional camera can only take a 2D slice of the 4D light field. To recover the entire information content of the light field, we need to modulate the incoming light field so as to redistribute the energy from the 4D FLS to the 2D sensor.

5.3 Heterodyne Light Field Camera

In this section, we show that the required modulation can be achieved in frequency domain by the use of an appropriately chosen 2D mask placed at an appropriate position between the lens and the sensor. Although a mask is only a 2D modulator, in tandem with the lens, it can achieve the desired 4D modulation. We believe that this is the first design of a single-snapshot light field camera that does not use any additional lenses or other refractive elements.

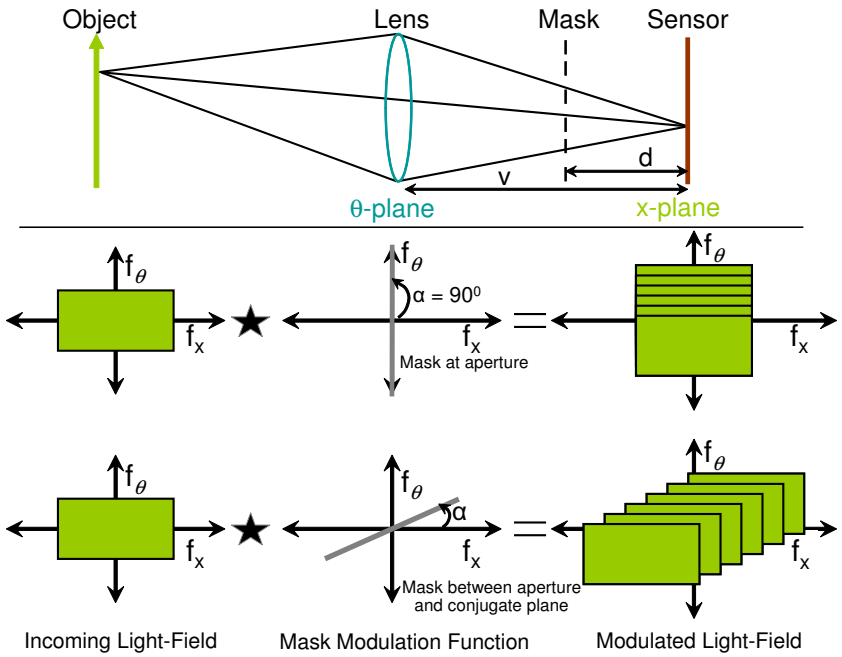

Figure 5.3: Heterodyne light field camera. (Top) In ray-space, the cosine mask at d casts soft shadows on the sensor. (Bottom) In Fourier domain, scene spectrum (green on left), convolved with mask spectrum (center) made of impulses creates offset spectral tiles (right). Mask spectral impulses are horizontal at $d = 0$, vertical at $d = v$, or tilted.

5.3.1 Modulation Theorem and its Implications

According to the modulation theorem [120], when a baseband signal $s(x)$ is multiplied by a cosine of frequency f_0, it results in copies of the signal at that frequency.

$$\mathfrak{F}[\cos(2\pi f_0 x)s(x)](f_x) = \frac{1}{2}(F(f_x - f_0) + F(f_x + f_0)), \tag{5.9}$$

where $\mathfrak{F}[s(x)](f_x) = F(f_x)$ denotes the Fourier transform of $s(x)$. This principle has been widely used in telecommunications and radio systems. The baseband signal is modulated using a *carrier* signal of much higher frequency so that it can be transmitted over long distances without significant loss of energy. The receiver demodulate the received signal to recover the baseband signal. In essence, what

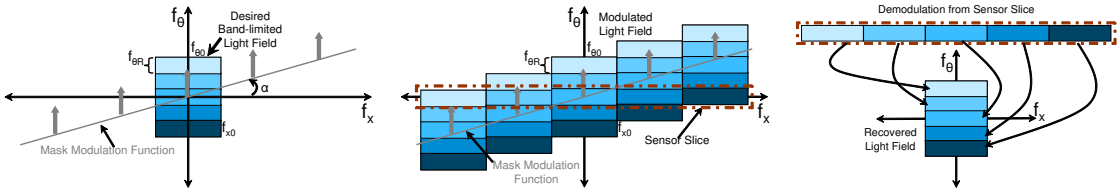

Figure 5.4: Spectral slicing in heterodyne light field camera. (Left) In Fourier domain, the sensor measures the spectrum only along the horizontal axis ($f_\theta = 0$). Without a mask, sensor can't capture the entire 2D light field spectrum (in blue). Mask spectrum (gray) forms an impulse train tilted by the angle α. (Middle) By the modulation theorem, the sensor light field and mask spectra convolve to form spectral replicas, placing light field spectral slices along sensor's broad $f_\theta = 0$ plane. (Right) To re-assemble the light field spectrum, translate segments of sensor spectra back to their original f_x, f_θ locations.

we wish to achieve is very similar. We would like to modulate the information in the angular variations of the light field (f_θ frequencies) to higher frequencies in f_x so that the high resolution 1D sensor may be able to sense this information.

Figure 5.4 shows a bandlimited light field in frequency domain. For simplicity, let us assume the x plane to be the conjugate plane, so that the sensor image corresponds to a slice along f_x (horizontal slice). Now consider a modulator whose frequency response is composed of impulses arranged on a slanted line as shown in Figure 5.4. If the light field is modulated by such a modulator, each of these impulses will create a spectral replica of the light field at its center frequency. Therefore, the result of this convolution will be several spectral replicas of the light field along the slanted line. The elegance of this specific modulation is that the horizontal slice (dashed box) of the modulated light field spectrum now captures all the information in the original light field. Note that the angle α is designed

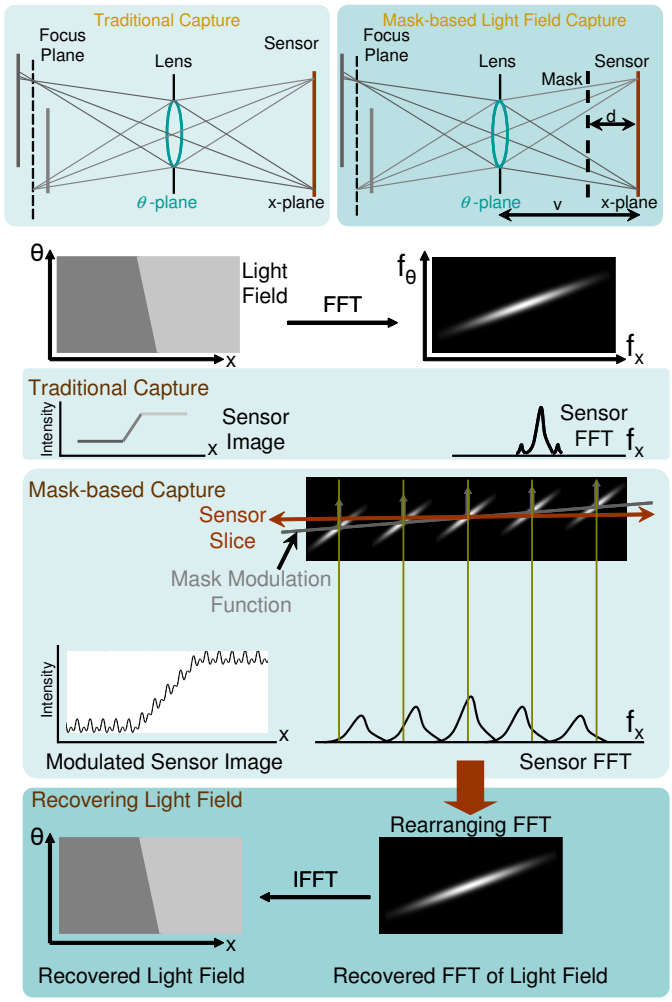

Figure 5.5: Ray space and Fourier domain illustration of light field capture. The flatland scene consists of a dark background planar object occluded by a light foreground planar object. In absence of a mask, the sensor only captures a slice of the Fourier transform of the light field. In presence of the mask, the light field gets modulated. This enables the sensor to capture information in the angular dimensions of the light field. The light field can be obtained by rearranging the 1D sensor Fourier transform into 2D and computing the inverse Fourier transform.

based upon the required frequency resolution in θ and x, and the bandwidth of the incoming light field.

Heterodyne receivers in telecommunications demodulate the incoming signal to recover the baseband signal. In our case, demodulation must also redistribute the energy in the sensed 1D signal to the 2D light field space. The process of demodulation consists of rearranging the frequency response of the sensor to recover the bandlimited light field as shown in Figure 5.4.

5.3.2 Mask based Heterodyning

Now we show that the required modulation can be achieved by placing a suitably chosen attenuating mask in the optical path of a conventional camera.

Masks as Light Field Modulators: A mask is essentially a special 1D code c(y) (2D for 4D light field) placed in the optical path. In flatland, although the mask is 1D, its modulation function is 2D (Figure 5.3). The mask affects the light field differently depending on where it is placed. If the mask is placed at the aperture stop (θ plane), then the effect of mask is to multiply the aperture modulation function by the mask modulation function. The mask modulation function $m(x, \theta)$ is then given by $m(x, \theta) = c(y = \theta)$, i.e., the modulation function is independent of x. Intuitively, when placed at the θ-plane, the mask affects all rays at an angle θ in similar way, independent of the scene point from which they are originating.

If the mask is placed at the conjugate plane, it attenuates all rays (independent of θ) for same x equally. This is because at the conjugate plane, all rays originating from a point on the plane of focus converge to a single point. Thus, the mask modulation function changes to $m(x, \theta) = c(y = x)$.

Thus, we see that the modulation function corresponding to placing the *same* code at the aperture and the conjugate plane are related by a rotation of 90° in the

2D light field space. Moreover, as the 1D code is moved from the aperture plane to the plane of the sensor, the resulting mask modulation function gets rotated in 2D as shown in Figure 5.3.

Let v be the distance between the aperture and the conjugate plane. If the mask $c(y)$ is placed at a distance d from the conjugate plane, the mask modulation function is given by

$$M(f_x, f_\theta) = \mu^2 C(\mu\sqrt{f_x^2 + f_\theta^2})\delta(f_\theta \cos\alpha - f_x \sin\alpha), \tag{5.10}$$

where C denotes the Fourier transform of the 1D mask and $\mu = 1/\sqrt{(d/v)^2 + (1 - (d/v))^2}$. The angle α is given by

$$\alpha = \arctan(d/(v - d)) \tag{5.11}$$

In other words, the mask modulation function has all its energy concentrated on a *line* in the 2D FLS space. The angle α of this line with respect to the f_x axis depends upon the position of the mask. When the mask is placed at the conjugate plane ($d = 0$), the angle α is equal to 0. As the mask moves away from the conjugate plane towards the aperture, this angle increases to 90° at the aperture plane as shown in Figure 5.3,

Optimal Mask Position: In order to capture the 2D light field, we need the modulation function $M(f_x, f_\theta)$ to be a series of impulses at an angle α given by

$$\alpha = \arctan \frac{f_{\theta R}}{2f_{x0}}, \tag{5.12}$$

where f_{x0} is the bandwidth of the light field along the f_x axis and $f_{\theta R}$ represents the desired frequency resolution along the f_θ axis. For example, in Figure 5.4, the frequency resolution has been depicted as being equal to $f_{\theta R} = (2/5)f_{\theta 0}$, where $f_{\theta 0}$ is the bandwidth of the light field along the f_θ axis. Thus, for capturing a light field of a given bandwidth, the physical position of the mask can be calculated

from (5.12) and (5.11). In practice, since the spatial resolution is much larger than the angular resolution, α is very small, and therefore the mask needs to be placed close to the sensor.

Optimal Mask Pattern: To achieve $M(f_x, f_\theta)$ as a set of 1D impulses on a slanted 2D line, the Fourier transform $C(f)$ of the 1D mask should be a set of impulses. Let $2p + 1$ be the number of impulses in $M(f_x, f_\theta)$. The Fourier transform of the 1D mask is then given by

$$C(f) = \sum_{k=-p}^{k=p} \delta(f - kf_0), \tag{5.13}$$

where f_0 denotes the fundamental frequency and is given by $f_0 = \mu\sqrt{4{f_{x0}}^2 + {f_{\theta R}}^2}$. From Figure 5.4, $(2p + 1)f_{\theta R} = 2f_{\theta 0}$. The bandwidth in f_θ is discretized by $f_{\theta R}$. Hence, the number of angular samples obtained in the light field will be equal to $\frac{2f_\theta}{f_{\theta R}} = 2p+1$. Since the Fourier transform of the optimal mask is a set of symmetric Dirac delta functions (along with DC), this implies that the physical mask is a sum of set of *cosines* of a given fundamental frequency f_0 and its harmonics. The number of required harmonics is in fact p, which depends upon the band-width of the light field in the f_θ axis and the desired frequency resolution $f_{\theta R}$.

Solving for 2D Light Field: To recover the 2D light field from the 1D sensor image, we compute the Fourier transform of the sensor image, *reshape* the 1D Fourier transform into 2D as shown in Figure 5.4 and compute the inverse Fourier transform. Thus,

$$l(x, \theta) = \texttt{IFT}(\texttt{reshape}(\texttt{FT}(y(s)))), \tag{5.14}$$

where `FT` and `IFT` represent the Fourier and inverse Fourier transforms respectively, and $y(s)$ is the observed sensor image. Figure 5.5 shows a simple example of light

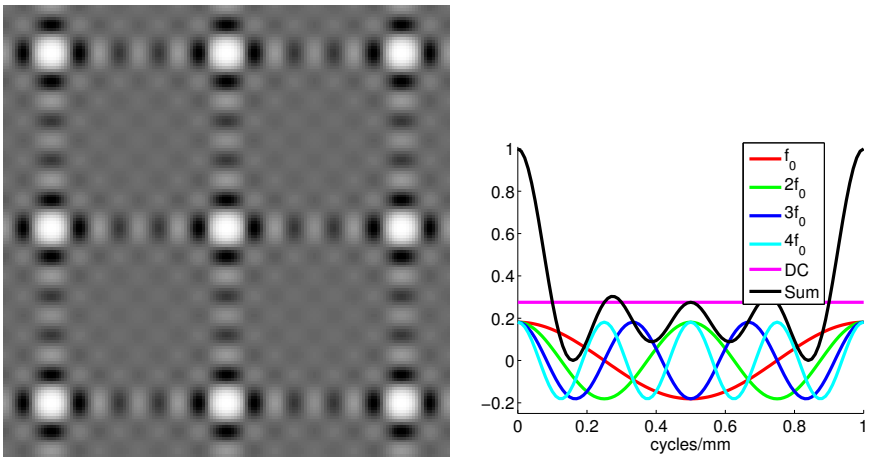

Figure 5.6: (Left) Zoom in of a part of the cosine mask with four harmonics. (Right) Plot of 1D scan line of mask (black), as sum of four harmonics and a constant term.

field capture where the scene consists of a dark background plane occluded by a light foreground plane.

5.3.3 Note on 4D Light Field Capture

Even though the analysis and the construction of mask-based heterodyning for light field capture was elucidated for 2D light fields, the procedure remains identical for capturing 4D light fields with 2D sensors. The extension to the 4D case is straightforward. In case of a 4D light field, the information content in the 4D light field is heterodyned to the 2D sensor space by the use of a 2D mask placed between the aperture and the sensor. The Fourier transform of the 2D mask would contain a set of impulses on a 2D plane.

$$C(f_1, f_2) = \sum_{k_1=-p_1}^{k_1=p_1} \sum_{k_2=-p_2}^{k_2=p_2} \delta(f_1 - k_1 f_0^x, f_2 - k_2 f_0^y). \tag{5.15}$$

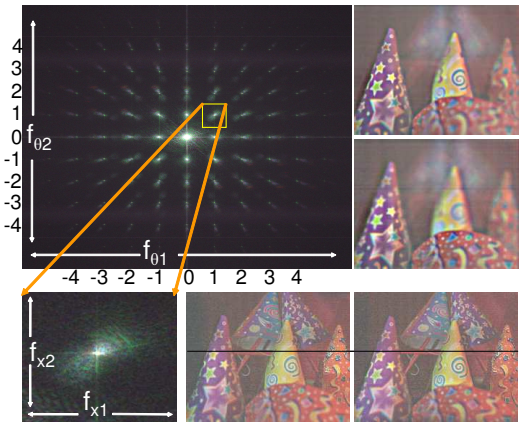

Figure 5.7: (Top Left) Magnitude of the 2D Fourier transform of the captured photo shown in Figure 5.8. θ_1, θ_2 denote angular dimensions and x_1, x_2 denote spatial dimensions of the 4D light field. The Fourier transform has 81 spectral tiles corresponding to 9×9 angular resolution. (Bottom Left) A tile of the Fourier transform of the 4D light field corresponding to $f_{\theta 1} = 1, f_{\theta 2} = 1$. (Top Right) Refocused images. (Bottom Right) Two out of 81 views. Note that for each view, the entire scene is in focus. The horizontal line depicts the small parallax between the views, being tangent to the white circle on the purple cone in the right image but not in the left image.

Since negative values in the mask cannot be realized as required, we need to boost the DC component of $C(f_1, f_2)$ so as to make the mask positive throughout. Figure 5.6 shows a part of the 2D cosine mask we used for experiments, along with the plot of one of its scanline. This 2D mask consists of four harmonics in both dimensions ($p_1 = 4, p_2 = 4$) with fundamental frequencies f_0^x and f_0^y being equal to 1 cycle/mm. This allows an angular resolution of 9×9 in the 4D light field. Figure 5.7 shows the magnitude of the Fourier transform of the captured photo of the cones (as shown in Figure 5.8). The Fourier transform clearly shows 9×9 spectral tiles created due to the modulation by the mask. These spectral tiles

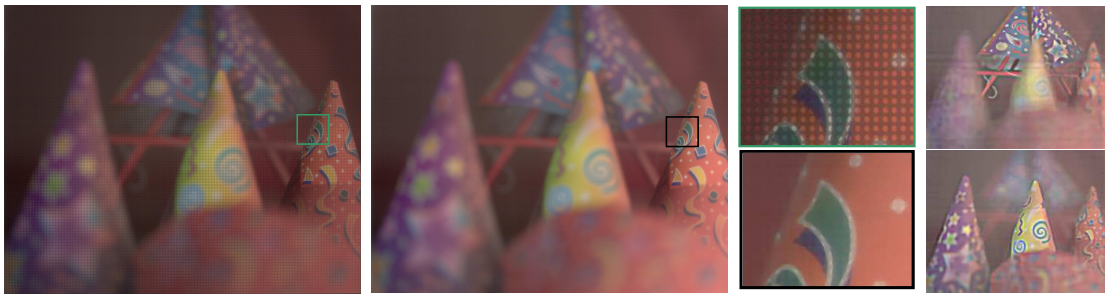

Figure 5.8: Our heterodyne light field camera provides 4D light field and full-resolution focused image simultaneously. (First Column) Raw sensor image. (Second Column) Scene parts which are in-focus can be recovered at full resolution. (Third Column) Inset shows fine-scale light field encoding (top) and the corresponding part of the recovered full resolution image (bottom). (Last Column) Far focused and near focused images obtained from the light field.

encode the information about the angular variation in the incident light field. To recover the 4D light field, demodulation involves *reshaping* of the sensor Fourier transform in 4D. Let $t_1 = 2p_1 + 1$ and $t_2 = 2p_2 + 1$ be the number of angular samples in the light field and let the captured 2D sensor image be $N \times N$ pixels. We first compute the 2D FFT of the sensor image. Then we rearrange $t_1 \times t_2$ tiles of the 2D Fourier transform into 4D planes to obtain a $(N/t_1) \times (N/t_2) \times t_1 \times t_2$ 4D Fourier transform. Inverse FFT of this 4D Fourier transform gives the 4D light field. In Figure 5.8, using a $1629 * 2052$ pixel image captured with a cosine mask having four harmonics, we obtain a light field with 9×9 angular resolution and 181×228 spatial resolution.

5.3.4 Formal Derivation for Mask based Heterodyning

This analysis is done for a 1D mask placed in front of a 1D sensor to capture a 2D light field. Let v be the total distance between the aperture and the sensor

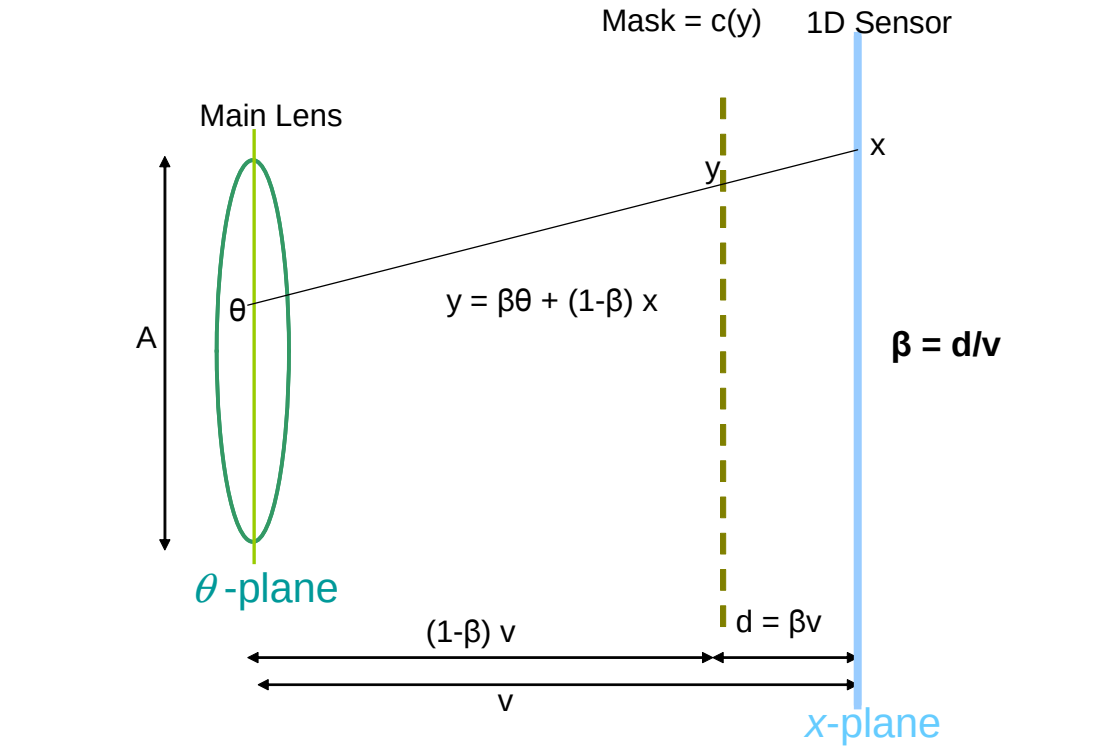

Figure 5.9: Schematic showing a 1D code place in front of a 1D sensor to capture a 2D light field. The light field is parameterized as twin-plane, with the x plane aligned with the sensor and the θ plane aligned with the aperture.

and d be the distance between the mask and the sensor. Define $\beta = \frac{d}{v}$. From Figure 5.3.4, if we place the 1D code $c(y)$ at a distance d from the sensor, the resulting 2D light field gets attenuated by the 2D mask $m(x, \theta)$ given by

$$m(x, \theta) = c(\beta\theta + (1 - \beta)x). \tag{5.16}$$

As we will derive below, the Fourier transform of the mask lies on a line in the 2D Fourier light field space.

Let $C(f_y)$ be the 1D Fourier transform of $c(y)$

$$C(f_y) = \int_{-\inf}^{\inf} c(y) \exp(-j2\pi f_y y) dy \tag{5.17}$$

and let $M(f_x, f_\theta)$ be the 2D Fourier transform of $m(x, \theta)$:

$$M(f_x, f_\theta) = \int_{-\inf}^{\inf} \int_{-\inf}^{\inf} m(x, \theta) \exp(-j2\pi f_x x) \exp(-j2\pi f_\theta \theta) dx d\theta. \tag{5.18}$$

We wish to find the expression of $M(f_x, f_\theta)$ in terms of $C(y)$. Let

$$y = \beta\theta + (1 - \beta)x \tag{5.19}$$

Use auxiliary variable

$$z = (1 - \beta)\theta - \beta x \tag{5.20}$$

Define

$$\mu = \frac{1}{\sqrt{\beta^2 + (1 - \beta)^2}} \tag{5.21}$$

Then

$$\theta = \mu^2(\beta y + (1 - \beta)z) \tag{5.22}$$

$$x = \mu^2((1 - \beta)y - \beta z) \tag{5.23}$$

Jacobian

$$J = \det \begin{bmatrix} \frac{\partial \theta}{\partial y} & \frac{\partial \theta}{\partial z} \\ \frac{\partial x}{\partial y} & \frac{\partial x}{\partial z} \end{bmatrix} \tag{5.24}$$

$$J = \mu^2 \tag{5.25}$$

By change of variables, we have

$$M(f_x, f_\theta) = J \int_{-\inf}^{\inf} \int_{-\inf}^{\inf} c(y) \exp(-j2\pi f_y y) \exp(-j2\pi f_z z) dy dz \tag{5.26}$$

Substituting x and θ from (5.22) and (5.23) in (5.18), and comparing common terms, we get

$$f_y = \mu^2(f_x(1-\beta) + f_\theta \beta) \tag{5.27}$$

$$f_z = \mu^2(-f_x\beta + f_\theta(1-\beta)) \tag{5.28}$$

Integrating out z term will give a δ term. Thus

$$M(f_x, f_\theta) = JC(f_y)\delta(f_z) \tag{5.29}$$

Now substitute $\tan\alpha = \frac{\beta}{1-\beta}$ Then $\sin\alpha = \mu\beta$ and $\cos\alpha = \mu(1-\beta)$

Substituting in equation for f_y, we get

$$f_y = \mu(f_x \cos\alpha + f_\theta \sin\alpha) \tag{5.30}$$

Simplifying $\delta(f_z)$, we get

$$\delta(f_z) = \delta(f_\theta \cos\alpha - f_x \sin\alpha) \tag{5.31}$$

Finally

$$M(f_x, f_\theta) = \mu^2 C(\mu(f_x \cos\alpha + f_\theta \sin\alpha))\delta(f_\theta \cos\alpha - f_x \sin\alpha) \tag{5.32}$$

The δ function constraints the 2D Fourier transform of mask to lie along a line given by $f_\theta \cos\alpha - f_x \sin\alpha = 0$ Using this constraint the above equation can be simplified to

$$M(f_x, f_\theta) = \mu^2 C(\mu\sqrt{f_x^2 + f_\theta^2})\delta(f_\theta \cos\alpha - f_x \sin\alpha). \tag{5.33}$$

Thus,

$$\tan\alpha = \frac{\beta}{1-\beta} = \frac{d}{v-d}. \tag{5.34}$$

and

$$\mu = \frac{1}{\sqrt{\beta^2 + (1-\beta)^2}} = \frac{1}{\sqrt{(d/v)^2 + (1-(d/v))^2}} \tag{5.35}$$

Practical Design

In a practical design, first α is calculated using the frequency resolution in θ, $f_{\theta R}$ and the bandlimit f_{x0} of the light field in the spatial dimension. $f_{\theta R}$ is relate to the size of the aperture A. $f_{\theta R} = 1/A$.

$$\tan\alpha = \frac{f_{\theta R}}{2f_{x0}} \tag{5.36}$$

Once we know α and the total distance between the sensor and the aperture v, we can find d using (5.34). The fundamental frequency can be obtained using (5.33) by substituting $f_x = 2f_{x0}$ and $f_\theta = f_{\theta R}$

$$f_0 = \mu\sqrt{4f_{x0}^2 + f_{\theta R}^2} \tag{5.37}$$

In practice, μ is close to 1 and α is $\approx 4-5$ degrees.

5.3.5 Aliasing

Traditionally, undersampling results in masquerading of higher frequencies as lower frequencies in the *same* channel and leads to visually obtrusive artifacts like ghosting. In heterodyne light field camera, when the band-limit assumption is not valid in the spatial dimension, the energy in the higher *spatial* frequencies of the light field masquerade as energy in the lower *angular* dimensions. No purely spatial frequency leaks to other purely spatial frequency. Thus, we do not see familiar jaggies, moire-like low-frequency additions and/or blocky-ness in our results. The effect of aliasing is discussed in detail in [163], where using the statistics of natural images, it is shown that the energy in the aliasing components is small. To further combat the effects of aliasing, we post-filter the recovered light field using a Kaiser-Bessel filter with a filter width of 1.5 [114].

5.3.6 Light Field based Digital Refocusing

Refocused images can be obtained from the recovered Fourier transform of the light field by taking appropriate slices [114]. Figure 5.8 and Figure 5.7 shows refocused cone images. The depth variation for this experiment is quite large. Notice that the orange cone in the far right was in focus at the time of capture and we are able to refocus on all other cones within the field of view. Figure 5.11 shows the performance of digital refocusing with varying amounts of blur on the standard ISO-12233 resolution chart. Using the light field, we were able to significantly enhance the DOF. It is also straightforward to synthesize novel views from the recovered light field. Two such views generated from the recovered light field are also shown in the bottom right part of Figure 5.7. The horizontal line on the images depicts small vertical parallax between the two views. Digital refocusing

Figure 5.10: Our heterodyne light field camera can be used to refocus on complex scene elements such as the semi-transparent glass sheet in front of the picture of the girl. (Left) Raw sensor image. (Middle) Full resolution image of the focused parts of the scene can be obtained as described in Section 5.3.7. (Right) Low resolution refocused image obtained from the light field. Note that the text on the glass sheet is clear and sharp in the refocused image.

based on recovered light fields allow us to refocus even in the case of complicated scenes such as the one shown in Figure 5.10. In this example, a poster of the girl in the back is occluded by a glass sheet in front. Notice that the text 'Mask based Light Field' written on the glass sheet is completely blurred in the captured photo. By computing the light field, we can digitally refocus on the glass sheet bringing the text in focus.

5.3.7 Recovering High Resolution Image for Scene Parts in Focus

Our heterodyne light field camera has an added advantage that we can recover high resolution information for the *in-focus* Lambertian parts of the scene. Consider a scene point that is in sharp focus. All rays from this scene point reach the *same* sensor pixel but are attenuated differently due to the mask. Therefore, the sensor pixel value is the product of the scene irradiance and the average value of the mask within the cone of rays reaching that pixel. This attenuation $\gamma(x, y)$ varies from

pixel to pixel and can either be computed analytically or recovered by capturing a single calibration image of a uniform intensity Lambertian scene. We can recover the high resolution image $I(x, y)$ of the scene points in focus as

$$I(x, y) = s(x, y)/\gamma(x, y), \tag{5.38}$$

where $s(x, y)$ is the captured sensor image. Parts of the scene that were not in focus at the capture time will have a spatially varying blur in $I(x, y)$. We use the image of a uniform intensity Lambertian light box as γ.

In Figure 5.8, zoomed in image region shows the attenuation of the sensor image due to the cosine mask. The recovered high resolution picture is also shown in Figure 5.8 and the inset shows the fine details recovered in the parts of the image that were in focus. Figure 5.11 shows the recovered high resolution picture of a resolution chart that was in focus during capture. This ability to obtain high resolution images of parts of the scene along with the 4D light field makes our approach different from previous light field cameras.

5.4 Non Rectangular Band-Limits for Light-Field

The design in [160] was optimized assuming that the shape of the band-limit was rectangular as shown in Figure 5.4. But in real-world scenarios, the incident light field spectrum has specific shape characteristics that are heavily dependent upon the depth of objects in the scene [26, 44]. We show how to optimize the mask so as to match the shape of the band-limit in the frequency domain. Usually, the spatial resolution of light field is reduced by a factor equal to the number of angular samples in captured light field. However, by optimizing the mask, better spatial resolution can be achieved as shown below. For illustration, we assume 2D light

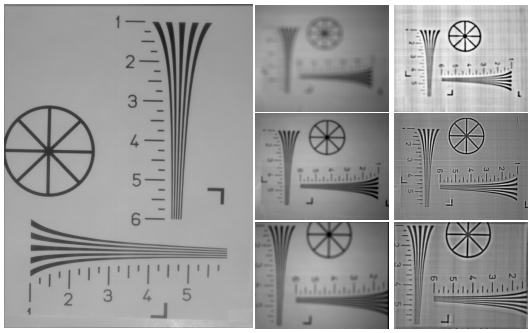

Figure 5.11: Analysis of the refocusing ability of the heterodyne light field camera. (Left) If the resolution chart is in focus, one can obtain a full resolution 2D image as described in Section 5.3.7, along with the 4D light field. (Middle) We capture out of focus chart images for three different focus settings. (Right) For each setting, we compute the 4D light field and obtain the low resolution refocused image. Note that large amount of defocus blur can be handled.

fields captured by 1D sensor, but it easily extends to 4D light fields captured by 2D sensor.

Let us assume that the band-limit light field is shaped as shown in Figure 5.12(a), with reducing spatial bandwidth as the angular frequency increases. Let the band-limits be given by (f_{x0}, f_{x1}, f_{x2}) corresponding to the angular frequencies $(f_\theta = 0, f_\theta = f_{\theta R}, f_\theta = 2f_{\theta R})$ as shown in Figure 5.12. Now consider a ray modulation function given by

$$R(f_x, f_\theta, :) = \sum_{i=-p}^{i=p} \delta(f_x - f_i, f_\theta - f_i \tan(\alpha), :), \tag{5.39}$$

where $f_i = 0, \quad i = 0$ and $f_i = f_{x0} + 2\sum_{j=1}^{j=i-1} f_{xj} + f_{x_i}, \forall i > 0$. This ray modulation function will lead to a series of *unequally* placed impulses and corresponding spectral copies of the light field as shown in Figure 5.12. The sensor image (red box) is a slice of the modulated light field (from Fourier Slice Theorem [114]). Note that the modulation function is now optimized so that the spectral copies are

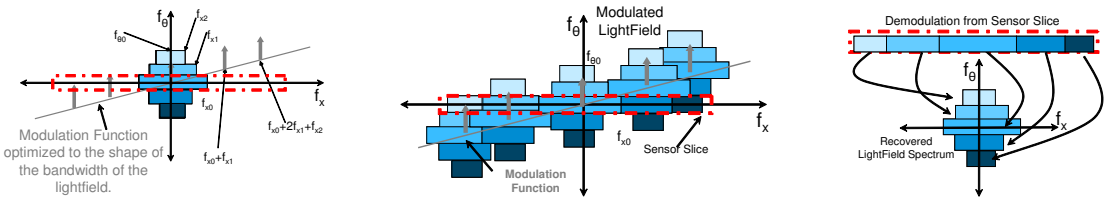

Figure 5.12: Optimal sampling of light fields. (Left) The bandlimit of the light field is not rectangular as in [160]. (Middle) The light field is modulated with cosines of appropriate frequencies (non-harmonics) so that the spectral replicas abut tightly on the sensor slice and there is no wastage of sensor pixels. Note that the spectral replicas could overlap in other parts of the spectrum which are not captured by the sensor. (Right) Demodulation involves reshaping the sensor Fourier transform as before accounting for unequal spectrum width in different angular samples.

tightly abut on the sensor without any gaps. If we have used a mask with impulses equally placed, it would have resulted in gaps on sensor slice corresponding to no information in the light field. Moreover, if the depth range of the scene is known apriori, this leads to a specific shape of the light field band-limit [26, 44] and one can potentially use this information to optimally sample the light field.

5.5 Implementation and Analysis

Heterodyne Light Field Camera: We build a large format camera using a flatbed scanner (Canon CanoScan LiDE 70) similar to [168,174] and place a 8×10 inch^2 mask behind the scanner glass surface. The mask was printed at a resolution of 80 dots/mm using Kodak LVT continuous tone film recorder (BowHaus Inc.). The scanner itself was then placed on the back of a large format view camera fitted with a 210 mm f/5.6 Nikkor-W lens as shown in Figure 5.1. In practice, the motion

of the scanner sensor is not smooth leading to pattern noise (horizontal/vertical lines) in the captured photo. This may lead to some artifacts in the recovered light fields. However, many of these issues will disappear with a finer mask placed inside a conventional digital camera. Calibration involves accounting for the in-plane rotation and shift of the mask with respect to the sensor which manifest as search for the rotation angle of the captured 2D image and the phase shift of the Fourier transform. Since the computation of the light field and refocusing is done in Fourier domain, computational burden is low.

Failure Cases: The heterodyne light field camera assumes a bandlimited light field. When this assumption is not true, it leads to aliasing artifacts in the recovered light field. To recover larger angular resolution in the light field, the 2D cosine mask needs to be moved away from the sensor, which might result in diffraction.

5.6 Applications of captured Light-Fields

In this section, we show two examples of captured light-field using the implementation described. Firstly, we printed a 2D sum of cosines mask with frequencies of $5, 10, 15, 20$ cycles/mm allowing us to obtain $2 \times 4 + 1 = 9$ angular samples in the light field with spatial resolution of 240×180 (Results shown in Figure 5.13). We also printed another 2D sum of cosines mask with frequencies of $8, 16, 24$ cycles/mm allowing us to obtain $2 \times 3 + 1 = 7$ angular samples in the light field with spatial resolution of 340×250 (Results shown in Figure 5.14).

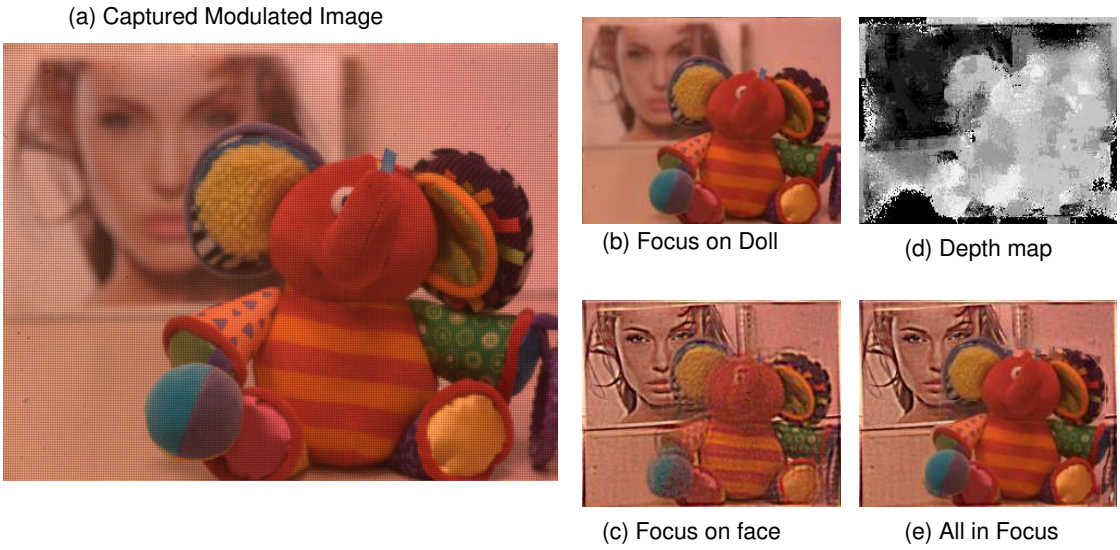

Figure 5.13: (a) Captured Modulated Image (b) Low Resolution Refocussed Image - Focus on Doll (c) Low Resolution Refocussed Image - Focus on face (d) Raw Depth labels quantized to 10 depth levels. (e) All in focus image.

5.6.1 Depth from Focus

Once we have captured the light field, images focused at any depth can be obtained by taking appropriate slices from the Fourier transform of the captured light field [114]. Figure 5.13(a) and 5.14(a) show the captured images of two scenes with significant texture and depth variations. Figures 5.13(b,c) and 5.14(b,c,d) show different refocused images for each dataset. We can extract depth from refocussed images since scene points that are not in focus are blurred while scene points in focus are sharp in the refocused images. So for a given pixel 'p', if we study a small region around the pixel, then, this region will be sharp in the refocused image at the correct depth while it will be blurred at all other depths. We use the variance of the neighborhood around each pixel as a measure of sharpness. Each pixel is assigned the depth corresponding to the refocused image in which the variance of its neighborhood is maximum. Such an assignment (10 depth levels) is shown in

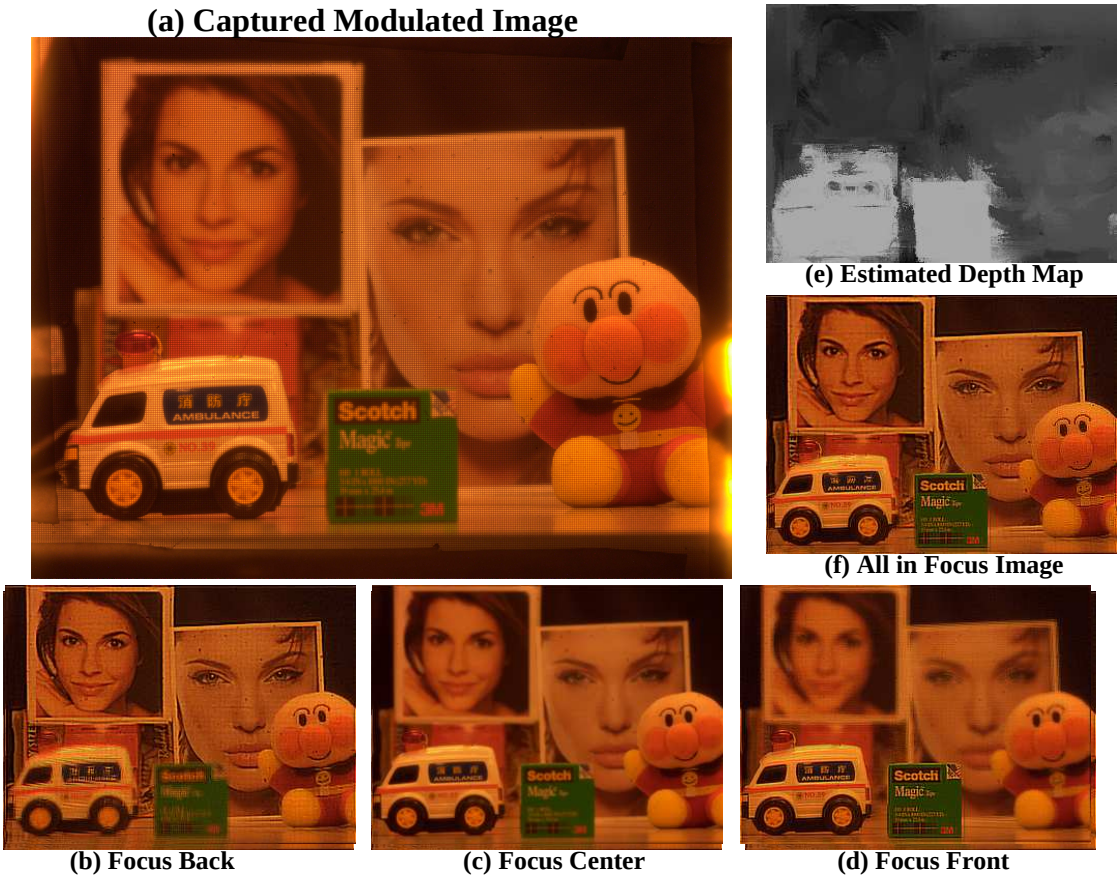

Figure 5.14: (a) Captured Modulated Image (b) Refocussed Image - Focus on back poster (c) Refocussed Image - Focus on doll (d) Refocussed Image - Focus on front Scotch box (e) Raw Depth labels quantized to 10 depth levels. (e) All in focus image.

5.13(d) and 5.14(e).

5.6.2 All Focus Image

We can also obtain the all-in-focus image just as is obtained in [114] from the estimated depth map and the corresponding refocussed images. For each pixel we choose the intensity from the refocused image corresponding to its estimated depth resulting in an all-in-focus images as shown in Figure 5.13(e) and Figure 5.14(f). Supplementary materials include Matlab code and input images as well as videos showing digital refocusing.

5.6.3 3D Texture mapped model

We can also obtain a 3D texture mapped estimate of the scene, since we have the depth estimates and the corresponding irradiance(intensity) estimates. This allows us to recover a 3D texture mapped surface corresponding to the scene by appropriately combining the depth and irradiance estimates to create a 3D texture mapped surface. We can also synthesize novel views from the estimated 3D texture mapped model.

5.7 Discussion

Future Directions: To capture the light field, we need to use masks that match the resolution of the sensor. It is already possible to print RGB Bayer mosaics at pixel resolution. This is ideal for the future trend of digital cameras where pixels are becoming smaller to achieve higher resolution. Such high resolution masks will support heterodyning as well as Bayer mosaic operations in a single mask. Our

current masks are effectively 2D in a 4D space, but in the future one may use masks that are angle and location dependent like a hologram to achieve a complete 4D effect. We hope our work in broadband and cosine masks will also stimulate more ideas in mask functions including colored and polarized masks to estimate scene properties.

Our broadband coding can be pushed in higher dimension, for example, by coding both in time [134] and space. The benefit of masks compared to lenses is the lack of wavelength dependent focusing and chromatic aberrations. This fact is commonly used in astronomy. Hence, masks can be ideal for hyper-spectral imaging. Shallow depth of field is a serious barrier in medical and scientific microscopy. The facility to refocus while maintaining full resolution will be a great benefit. In combination with confocal coded aperture illumination one maybe able to capture digitally refocused images in a fewer incremental steps of the focal planes.

Conclusions: We showed that two different kinds of coded masks placed inside a conventional camera will each allow us to make a different kind of computational improvement to the camera's pictures. First, if we place a fine, narrowband mask slightly above the sensor plane, then we can computationally recover the 4D light field that enters the main camera lens. The mask preserves our camera's ability to capture the focused part of the image at the full resolution of the sensor, in the same exposure used to capture the 4D light field. Second, if we place a coarse, broadband mask at the lens aperture, we can computationally refocus an out of focus image at full resolution. As this refocusing relies on deconvolution, we can correct the focusing for images that require constant or piecewise-planar focusing. These and other masks are not magical: mask reduces sensor illumination by ≈ 1 f-stop and refocusing exacerbates noise. However, high-quality masks may be less

demanding than lens arrays to mount, align, or arrange in interchangeable sets and they avoid optical errors such as radial error, spherical and chromatic aberration, and coma. We believe that masks offer a promising new avenue for computational methods to substantially improve digital photography.

Appendix: Source Code

```
% Source Code for Computing 4D Light-Field from Captured 2D Photo
% Mask contains Cosines with 4 Harmonics leading to 9X9 Angular Samples

m = 2133; n=1719 % Size of Captured Image
nAngles = 9; cAngles = (nAngles+1)/2;  % Number of Angular Samples
F1Y = 237;  F1X = 191;  %Cosine Frequency in Pixels from Calibration Image
phi1 = 300;  phi2 = 150; % PhaseShift due to Mask In-Plane Transltn wrt Sensor
F12X = floor(F1X/2); F12Y = floor(F1Y/2);

%Compute Spectral Tile Centers, Peak Strengths and Phase
for i=1:nAngles ;  for j=1:nAngles
   CentY(i,j) = (m+1)/2 + (i-cAngles)*F1Y;CentX(i,j)  = (n+1)/2  + (j-cAngles)*F1X;
   Mat(i,j) = exp(sqrt(-1)*((phi1*pi/180)*(i-cAngles) + (phi2*pi/180)*(j-cAngles)));
end;  end
Mat(cAngles,cAngles) = Mat(cAngles,cAngles) * 20;

f = fftshift(fft2(imread('InputCones.png'))); %Read Photo and Perform 2D FFT

%Rearrange Tiles of 2D FFT into 4D Planes to obtain FFT of 4D Light-Field
for i = 1: nAngles; for j = 1: nAngles
        FFT_LF(:,:,i,j) =  f(CentY(i,j)-F12Y:CentY(i,j)+F12Y,...
                           CentX(i,j)-F12X:CentX(i,j)+F12X)/Mat(i,j);
end; end

LF    =    ifftn(ifftnshift(FFT_LF)); %Compute Light-Field by 4D Inverse FFT
```

Chapter 6

Discussions and Future Directions

The first part of this dissertation studied the problem of characterizing, learning and classifying dynamic patterns that appear in video. Specific attention was paid to apllications such as gait based person identification, activity recognition, comparing shape sequences, simultaneous tracking and behavior analysis. It was shown that solutions to these issues may be posed as a problem in inferring and mathematically characterizing the nature of the dynamics of the relevant patterns in video. Some of the areas for future work are listed below.

6.1 Comparing ShapeSequences

6.1.1 Shape descriptor for Comparing Shape Sequences

We used Kendall's statistical shape as the shape feature for comparing shape sequences. Kendall's statistical shape is a sparse descriptor of the shape. We could, in theory choose a denser shape descriptor like the shape context [7] which has been proven to be more resilient to noise. But, such a dense descriptor also intro-

duces significant and non-trivial relationships between the individual components of the descriptor. This usually makes learning the dynamics very difficult. Since the emphasis of this proposal is on modeling the dynamics in shape sequences, we restricted ourselves to the treatment of dynamics in Kendall's statistical shape. We could look at models for comparing shape sequences that are based on more complex shape descriptors like the shape context. It is expected that using such complex and robust shape descriptors will improve the performance of these algorithms significantly while also making the learning and the inference tasks more complex.

6.1.2 View-Invariance

The models developed for comparing shape sequences in this dissertation have not incorporated the important property of view invariance that is usually highly desirable in several computer vision applications. Incorporating view invariance into these models is an important avenue for future research. One way to make these models view-invariant is to use features that are themselves view invariant. Once the feature chosen is view-invariant, then all the algorithms described in the previous sections in turn become view invariant. Another way to incorporate view-invariance is to build these models for a discrete set of views separately. Once we have a model for each activity in every possible view, then the inference algorithms could be suitably modified to incorporate view-invariance. But, this would require a huge amount of data to learn the model for each activity, since the learning algorithm must learn the activity from every possible viewpoint. Which of these two approaches turn out to be more efficient would depend upon the application being considered. For applications in far field surveillance and activity analysis,

where the number of discrete views required is small, learning a model for each of these discrete viewpoints might be a viable alternative. For applications in near field activity analysis, where the number of discrete views one must account for is large, the best alternative might be to choose appropriate view invariant features.

6.2 Action Analysis and Recognition

6.2.1 Noise Sensitivity of the Activity Model

The noise sensitivity of the learning algorithm for simultaneous inference of the nominal activity trajectory and the activity specific time warping space has not been studied in detail. It would be interesting to study and analyse the sensitivity of the learning algorithm to noise in the data. Noise in the data could be of two forms. There could be observation noise because of the characteristics of the imaging sensors and the limited resolution offered by these sensors. There could also be labelling noise because of incorrect labelling of activity sequences. Robust techniques to detect incorrect labelling need to be developed so that the inference process is robust to outliers. Moreover, studying the noise sensitivity of the learning algorithm will also enable us to improve the learning algorithm. This issue is related to modeling the distribution of time-warping transformations and we are looking at algorithms that are able to tackle both these issues simultaneously.

6.2.2 Spatial Alignment of Activities

Another issue of concern is the spatial alignment of sequences. There is significant variety in the spatial alignment within an activity. For example the action of sitting might be accompanied by the two legs being very close to each other or further

apart as is the preference of the individual. Since the activity model proposed corrects only the temporal misalignments in the execution of an activity, in its current form it is not adequate to reliably tackle spatial alignment preferences of an individual. In the current model, small spatial misalignments are tackled as temporal misalignments. We are addressing the larger spatial misalignments, using a mixture of models, where each mixture represents one type of spatial alignment preference. It might also be possible to simultaneously perform both spatial and temporal alignments, though this would be at the cost of significant computational expense. The method would, in principle, be very similar to the clustering of activity sequences described earlier. The various sequences of an activity would be clustered into several different clusters each cluster representing one particular spatial alignment preference.

6.3 Clustering and Indexing of Action Videos

The focus of this dissertation has been on the problem of recognition or classification with respect to activity analysis. Another allied problem is the problem of automatic activity baased video clustering or indexing which has applications in several domains such as surveillance, traffic monitoring and multimedia entertainment. This problem is gaining in importance because of the ever increasing role of videos in our everyday lives with applications ranging from broadcast news, entertainment, scientific research, security and surveillance. There has been significant research into indexing of multimedia data such as news clips, sports videos etc according to their content. Applications for automatic discovery of activity patterns are numerous. For example, security and surveillance videos typically have repetitive activities. If the typical activities can be clustered, then several

problems such as unusual activity detection, efficient indexing and retrieval can be addressed. In applications of video forensics, instead of expecting an analyst to sift through the voluminous data, we ask - can 'clusters' of activities be presented that embody the essential characteristics of the videos.

6.3.1 An Approach we are exploring

Given a continuous video stream, if we knew what activities occur in it, we can discover the boundaries between them and if we were given the boundaries, the individual activities could be learnt as well. For unsupervised video clustering, we need to solve the segmentation and model estimation problems simultaneously. We use coherent patterns of motion to discover individual segment boundaries and the transitions between segments are used to learn activity models. Each individual segment is modeled using a linear dynamical system. Each activity then consists of a specific sequence of dynamical systems.

The entire video is first segmented in short coherent patterns. The entire set of segments is assumed to be derived from an underlying vocabulary. This vocabulary is learnt using unsupervised clustering of the segments. Once the vocabulary is learnt, we then learn grammatical rules from the video to discover longer activities. In our case, the grammatical rules are simple sequences of segment labels.

We augment the traditional dynamical systems model in important ways. We derive methods to incorporate view and rate invariance into these models so that similar actions are clustered together irrespective of the viewpoint or the rate of execution of the activity. We also derive algorithms to learn the model parameters from a video stream and demonstrate how a single video sequence may be clustered into different clusters where each cluster represents an activity. We show here

some preliminary results using our approach on a dataset of skating videos. We performed a clustering and retrieval experiment on the figure skating dataset. This data is very challenging since it is unconstrained and involves rapid motion of both the skater and real-world motion of the camera including pan, tilt and zoom.

We built color models of the foreground and background using normalized color histograms. The color histograms are used to segment the background and foreground pixels. Median filtering followed by connected component analysis is performed to reject small isolated blobs. From the segmented results, we fit a bounding box to the foreground pixels by estimating the 2D mean and second order moments along x and y directions.We perform temporal smoothing of the bounding box parameters to remove jitter effects. The final feature is a rescaled binary image of the pixels inside the bounding box.

Clustering Experiment: Most figure skating videos consist of a few established elements or moves such as jumps, spins, lifts and turns. A typical performance by skater or pair of skaters includes several of these elements each performed several times. Due to the complex body postures involved it is a challenge even for humans to identify clear boundaries between atomic actions. It was difficult even for us to semantically define temporal boundaries of an activity, let alone define a metric for temporal segmentation. Thus, this makes it very difficult to break the video into temporally consistent segments. Instead of performing explicit segmentation, we build models for fixed length subsequences using sliding windows. The results of a temporal segmentation algorithm that can split such a complex video into meaningful segments, can be easily plugged in. We use 20 frame long overlapping windows for building models of the video. Also, most of the interesting activities such as sitting spins, standing spins, leaps etc are usually

few and far between. Further, due to the subsequence approach, there will necessarily be several segments that do not contain any meaningful action. As a simple example, a subsequence that contains the transition from a spin to a jump will not fit into either of these action-clusters. To discover the interesting activities, we first need to remove these outlier segments. First, we cluster all the available subsequences into a fixed number of clusters (say 10). Then, from each cluster we remove the outliers using a simple criterion of average distance to the cluster. Then, we recluster the remaining segments. We show some sample sequences in the obtained clusters in figures 14 18. We observe that Clusters 1 - 4 correspond dominantly to Sitting Spins, Standing Spins, Camel Spins and Spirals respectively (in a spiral the skater glides on one foot while raising the free leg above hip level). Cluster 5 on the other hand seems to capture the rest of the uninteresting actions.

6.4 Computaional Imaging

6.4.1 Coded Aperture Imaging for Glare Aware Photography

Glare arises due to multiple scattering of light inside the cameras body and lens optics and reduces image contrast. While previous approaches have analyzed glare in 2D image space, we have begun analysing glare as a 4D ray-space phenomenon. By statistically analyzing the ray-space inside a camera, we can classify and remove glare artifacts. In ray-space, glare behaves as high frequency noise and can be reduced by outlier rejection. While such analysis can be performed by capturing the light field inside the camera, it results in the loss of spatial resolution. Unlike light field cameras, we do not need to reversibly encode the spatial structure of

Figure 6.1: Shown above are a few sequences from Cluster1. Each row shows contiguous frames of a sequence. We see that this cluster dominantly corresponds to 'Sitting Spins'. Image best viewed in color. Please see http://www.umiacs.umd.edu/~pturaga/VideoClustering.html for video results.

Figure 6.2: Shown above are a few sequences from Cluster2. Each row shows contiguous frames of a sequence. Notice that this cluster dominantly corresponds to 'Standing Spins'. Image best viewed in color. Please see http://www.umiacs.umd.edu/∼pturaga/VideoClustering.html for video results.

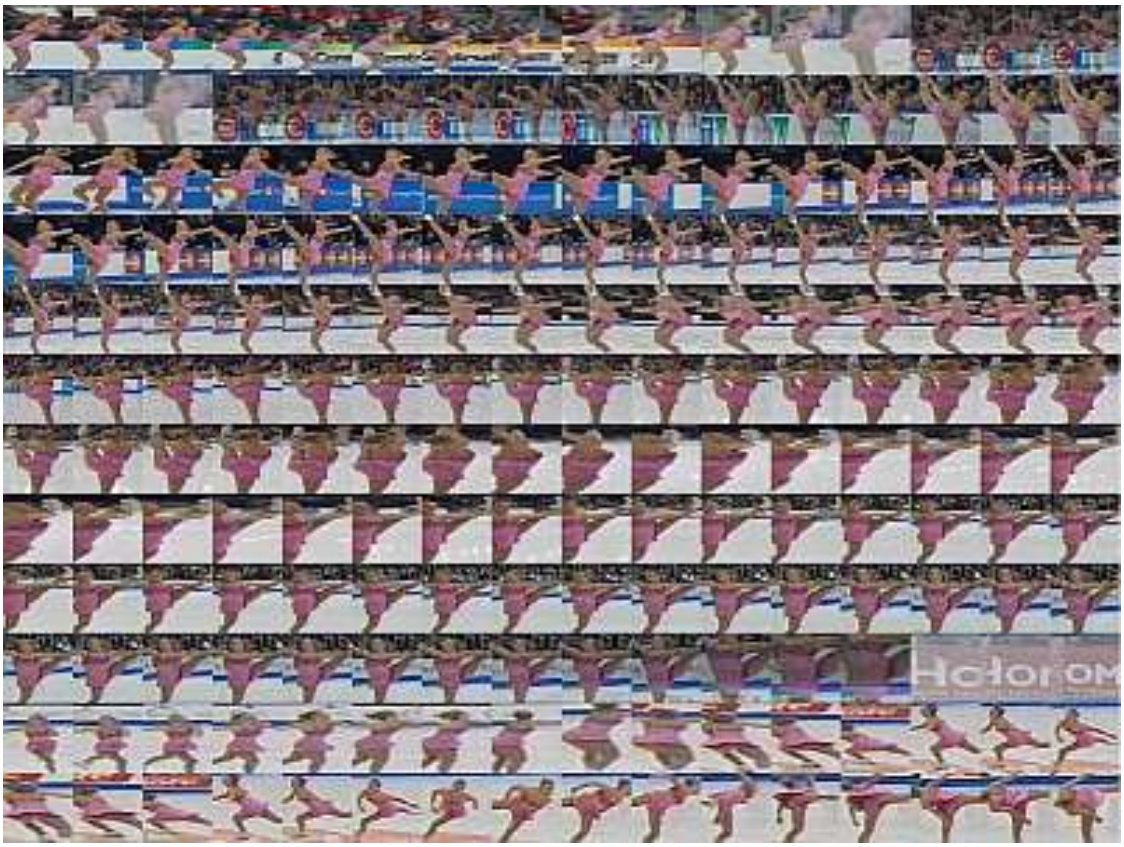

Figure 6.3: Shown above are a few sequences from Cluster3. Each row shows contiguous frames of a sequence. Notice that this cluster dominantly corresponds to 'Spirals'. Image best viewed in color. Please see http://www.umiacs.umd.edu/∼pturaga/VideoClustering.html for video results.

the rayspace, leading to simpler designs. We explore masks for uniform and non-uniform ray sampling and show a practical solution to analyze the 4D statistics without significantly compromising image resolution. Although diffuse scattering of the lens introduces 4D low-frequency glare, we can produce useful solutions in a variety of common scenarios. Such an approach handles photography looking into the sun and photos taken without a hood, removes the effect of lens smudges and reduces loss of contrast due to camera body reflections. Figure 6.4 shows a comparison of glare formation in ray-space. It shows how inserting a high frequency occluder in the optical path of the camera the low frequency glare components are converted to high frequency 2D image information and can therefore be easily removed by simple filtering. Figure 6.5 shows an example of an image captured in the presence of a high frequency occluder. Using a 4D analysis of glare inside the camera, we can emphasize or reduce glare. The photo in the middle shows a person standing against a sunlit window. We extract reflection glare generated inside lens and manipulate it to synthesize the result shown on the left. On the right we show the glare-reduced component. Notice that the face is now visible with improved contrast.

6.4.2 Coded Illumination

This dissertation was focussed on the effect of a non-refractive coded aperture and how to enhance the flexibility available during photography using such coded apertures. In some applications such as capturing Bidirection Reflectance Distribution Functions (BRDF) it might be acceptable to use active illumination. Bidirection Reflectance Distribution Function (BRDF) is a 4-dimensional function that describes how an opaque surface point reflects incoming light [136]. The incoming

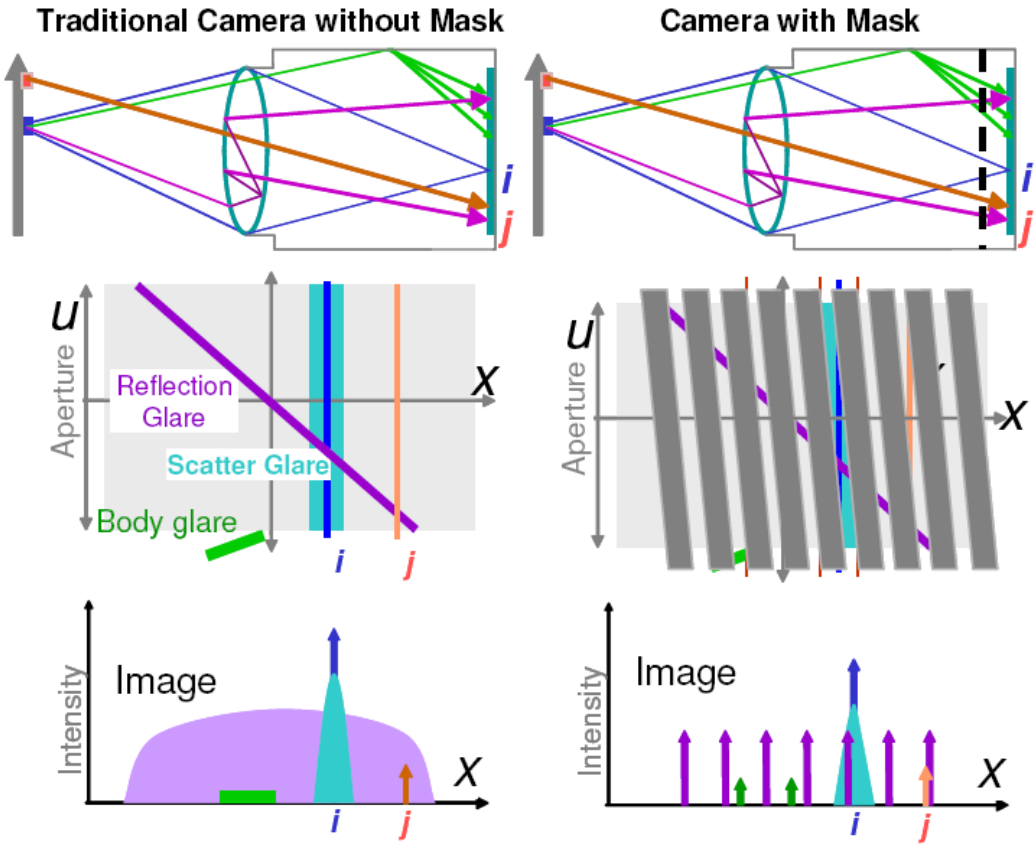

Figure 6.4: Comparison of glare formation in ray-space and sensor image for a traditional camera and our mask based camera. A focused blue scene patch could contribute to scattering (cyan), reflection (purple) and body glare (green). Since the sensor image is a projection of the ray-space along angular dimensions, the sum of these components creates a low frequency glare for a traditional camera. However, by inserting a high frequency occluder (gray), in front of the sensor, these components are converted into a high frequency 2D pattern and can be separated.

Figure 6.5: We extract glare components from a single-exposure photo in this high dynamic range scene. Using a 4D analysis of glare inside the camera, we can emphasize or reduce glare. The photo in the middle shows a person standing against a sunlit window. We extract reflection glare generated inside lens and manipulate it to synthesize the result shown on the left. On the right we show the glare-reduced component. Notice that the face is now visible with improved contrast.

lighting direction θ is a two-dimensional quantity (azimuth and elevation) while the outgoing lighting direction ϕ is another two-dimensional quantity making the BRDF 4-dimensional function $B(\theta, \phi)$. The slice of the BRDF corresponding to the viewing direction being fixed (as would be the case when the scene is being observed by a fixed camera), while the incident illumination changes freely, is called the reflectance field and is a two-dimensional function $R(\theta)$. Observing and measuring the reflectance field of an object or a scene typically involves acquiring images of the object/scene under varying illumination conditions. Typical methods for capturing such reflectance fields are based on acquiring images with a single light source 'ON' in each image. Recently, [138] have shown that using multiple light sources per each acquired image and performing a linear inversion in order to recover the reflectance field results in higher signal to noise ratios of the captured reflectance fields. Nevertheless, the number of images to be acquired to infer

the reflectance field remains identical to the number of illumination sources. Recently, we have been working on a method for acquiring accurate reflectance fields of objects with significantly lower number of captured images than the number of illumination sources. This reduction in the number of required images is achieved by exploiting recent developments in compressive sensing, which essentially show that if the signal to be acquired is sparse in some basis, then the signal can be accurately reconstructed using sub-Nyquist linear samples of the signal. We have emperically found that reflectance fields are sparse in the Haar wavelet basis. We wish to motivate our analysis using the Phong illumination model and empirically verify the degree of sparsity. We are currently developing a scheme for capturing reflectance fields using multiplexed illumination, thereby achieving the signal-to-noise ratio advantages of multiplexed illumination and use a compressive sensing based recovery algorihm to infer reflectance fields. Such methods using active illumination to capture visual properties of surfaces might be another avenue for active future research.

BIBLIOGRAPHY

[1] E.H. Adelson and J.R. Bergen. The plenoptic function and the elements of early vision. *Computational Models of Visual Processing*, 1, 1991.

[2] T. Adelson and J.Y.A Wang. Single lens stereo with a plenoptic camera. *IEEE Trans. on Pattern Analysis and Machine Intelligence*, 14:99–106, 1992.

[3] Aseem Agarwala, Mira Dontcheva, Maneesh Agrawala, Steven Drucker, Alex Colburn, Brian Curless, David Salesin, and Michael Cohen. Interactive digital photomontage. *ACM Trans. Graph.*, 23(3):294–302, 2004.

[4] J.K. Aggarwal and Q. Cai. Human motion analysis: A review. *Computer Vision and Image Understanding*, 73(3):428–440, 1999.

[5] A. Agrawal, R. Raskar, S.K. Nayar, and Y. Li. Removing photography artifacts using gradient projection and flash-exposure sampling. *ACM Trans. Graph.*, 24(3):828–835, 2005.

[6] E.M. Arkin, L.P. Chew, D.P. Huttenlocher, K. Kedem, and J.S.B. Mitchell. An efficiently computable metric for polygonal shapes. *IEEE Trans. on Pattern Analysis and Machine Intelligence*, 27:209–216, 1986.

[7] S. Belongie, J. Malik, and J. Puzicha. Shape matching and object recognition using shape contexts. *IEEE Trans. on Pattern Analysis and Machine Intelligence*, 24:509–522, April 2002.

[8] R. Berthilsson. A statistical theory of shape. *Statistical Pattern Recognition*, pages 677–686, 1998.

[9] A. Bhattacharya. On a measure of divergence between two statistical populations defined by their probability distributions. *Bull. Calcutta Math. Soc.*, 35:99–109, 1943.

[10] A. Bissacco, A. Chiuso, Y. Ma, and S. Soatto. Recognition of human gaits. *Conference on Computer Vision and Pattern Recognition*, 2:52–57, 2001.

[11] A. Bissacco, P. Saisan, and S. Soatto. Gait recognition using dynamic affine invariants. *Proc. Of MTNS 2004, Belgium*, July 2004.

[12] M. Black and A. Jepson. Eigentracking: Robust matching and tracking of articulated objects using a view-based representation. *International Journal of Computer Vision*, 26(1):63–84, 1998.

[13] M.J. Black and A.D. Jepson. A probabilistic framework for matching temporal trajectories. *International Conference on Computer Vision*, 22:176–181, 1999.

[14] S.S. Blackman and R. Popoli. *Design and Analysis of Modern Tracking Systems*. Artech House, 1999.

[15] A. Blake, B. North, and M. Isard. Learning multi-class dynamics. *Advances in NIPS*, pages 389–395, 1999.

[16] M. Blank, L. Gorelick, E. Shechtman, M. Irani, and R. Basri. Actions as Space-Time Shapes. *Computer Vision, 2005. ICCV 2005. Tenth IEEE International Conference on*, 2, 2005.

[17] H. Blum and R. Nagel. Shape description using weighted symmetric axis features. *Pattern Recognition*, 10:167–180, 1978.

[18] A. Bobick and Tanawongsuwan. Performance analysis of time-distance gait parameters under different speeds. *4th International Conference on Audio and Video based Biometric Person Authentication,Guilford,UK*, June 2003.

[19] A.F. Bobick and A. Johnson. Gait recognition using static activity-specific parameters. *Conference on Computer Vision and Pattern Recognition*, Dec. 2001.

[20] F.L. Bookstein. Size and shape spaces for landmark data in two dimensions. *Statistical Science*, 1:181–242, 1986.

[21] M. Brand, N. Oliver, and A. Pentland. Coupled hidden markov models for complex action recognition. *Computer Vision and Pattern Recognition*, pages 994–999, 1997.

[22] C. Bregler. Learning and recognizing human dynamics in video sequences. *CVPR*, 1997.

[23] P.J. Brockwell and R.A. Davis. *Time Series: Theory and Methods*. Springer-Verlang, 1987.

[24] T.J. Broida, S. Chandra, and R. Chellappa. Recursive techniques for the estimation of 3-d translation and rotation parameters from noisy image sequences. *IEEE Transactions on Aerospace and Electronic systems*, AES 26:639–656, 1990.

[25] C. Cédras and M. Shah. Motion-based recognition a survey. *Image and Vision Computing*, 13(2):129–155, 1995.

[26] Jin-Xiang Chai, Shing-Chow Chan, Heung-Yeung Shum, and Xin Tong. Plenoptic sampling. In *SIGGRAPH*, pages 307–318, 2000.

[27] MT Chan, A. Hoogs, R. Bhotika, A. Perera, J. Schmiederer, and G. Doretto. Joint Recognition of Complex Events and Track Matching. *Computer Vision and Pattern Recognition, 2006 IEEE Computer Society Conference on*, 2, 2006.

[28] C. C. Chen. Improved moment invariants for shape discrimination. *Pattern Recognition*, 26(5):683–686, 1993.

[29] J.C. Cheng and J.M.F. Moura. Capture and representation of human walking in live video sequence. *IEEE Transactions on Multimedia*, 1(2):144–156, 1999.

[30] O. Chomat and J.L. Crowley. Probabilistic recognition of activity using local appearance. *Proceedings of the IEEE Computer Society Conference on Computer Vision and Pattern Recognition*, 2:104–109, 1999.

[31] K.D. Cock and D.B. Moor. Subspace angles and distances between arma models. *Proc. of the Intl. Symp. of Math. Theory of networks and systems*, 2000.

[32] R.T. Collins, R. Gross, and J. Shi. Silhoutte based human identification using body shape and gait. *Intl. Conf. on Automatic Face and Gesture Recognition*, pages 351–356, October 2002.

[33] D. Comaniciu, V. Ramesh, and P. Meer. Real-time tracking of non-rigid objects using mean-shift. *Conference on Computer Vision and Pattern Recognition*, 2:142–149, 2000.

[34] D. Cunado, M.J. Nash, S.M. Nixon, and N.J Carter. Gait extraction and description by evidence gathering. *Proc. of the Intl. Conf. on AVBPA*, pages 43–48, 1994.

[35] J.E. Cutting and L.T. Kozlowski. Recognizing friends by their walk : Gait perception without familiarity cues. *Bulletin of the Psychonomic Society*, 9(5):353–356, 1977.

[36] J.E. Cutting and D.R. Proffitt. Gait perception as an example of how we may perceive events. *Intersensory perception and sensory integration*, 1981.

[37] P. Dollar, V. Rabaud, G. Cottrell, and S. Belongie. Behavior recognition via sparse spatio-temporal features. *Visual Surveillance and Performance Evaluation of Tracking and Surveillance, 2005. 2nd Joint IEEE International Workshop on*, pages 65–72, 2005.

[38] A. Doucet and N. De Freitas. *Sequential Monte Carlo Methods in Practice*. Springer, 2001.

[39] A. Doucet, N.D. Freitas, and N. Gordon. *Sequential Monte Carlo methods in practice*. Springer-Verlag, New York, 2001.

[40] E. R. Dowski and W.T. Cathey. Extended depth of field through wavefront coding. *Appl. Optics*, 34(11):1859–1866, April 1995.

[41] E. R. Dowski and G. E. Johnson. Wavefront coding: A modern method of achieving high performance and/or low cost imaging systems. In *SPIE Annual Meeting*, August 1999.

[42] I.L. Dryden. Statistical shape analysis in high level vision. *IMA Workshop: Image analysis and High level vision*, 2000.

[43] I.L. Dryden and K.V. Mardia. *Statistical shape analysis*. John Wiley and sons, 1998.

[44] Frédo Durand, Nicolas Holzschuch, Cyril Soler, Eric Chan, and François X. Sillion. A frequency analysis of light transport. *ACM Trans. Graph.*, 24(3):1115–1126, 2005.

[45] E. Eisemann and F. Durand. Flash photography enhancement via intrinsic relighting. *ACM Trans. Graph.*, 23(3):673–678, August 2004.

[46] H Farid and E.P. Simoncelli. Range estimation by optical differentiation. *Journal of the Optical Society of America A*, 15(7):1777–1786, 1998.

[47] A. Feldman and T. Balch. Automatic identification of bee movement using human trainable models of behavior. *Mathematics and Algoritms of Social Insects*, Dec 2003.

[48] R. Fergus, A. Torralba, and W.T. Freeman. Random lens imaging. Technical report, MIT, 2006.

[49] R.A. Fessenden. Wireless telephony. *Trans. American Institute of Electrical Engineers*, 27:553–629, 1908.

[50] S. Fine, Y. Singer, and N. Tishby. The hierarchical hidden markov model: Analysis and applications. *Machine Learning*, 32(1):41–62, 1998.

[51] J.P. Foster, M.S. Nixon, and A. Prugel-Bennett. Automatic gait recognition using area-based metrics. *Pattern Recognition Letters*, 24:2489–2497, 2003.

[52] D. Freedman and M.W. Turek. Illumination-invariant tracking via graph cuts. *IEEE International Conference on Computer Vision and Pattern Recognition*, 2005.

[53] H. Freeman. On the encoding of arbitary geometric configurations. *IRE Transactions*, 10:260–268, 1961.

[54] Von Frisch. *The Dance Language and orientation of bees.* Cambridge MA:Harvard University Press, 1993.

[55] D.M. Gavrila. The visual analysis of human movement: A survey. *CVIU*, 73(1):82–98, January 1999.

[56] D.M. Gavrilla. The visual analysis of human movement: A survey. *Elsevier Journal on Computer Vision and Image Understanding*, 73(1):82–98, January 1999.

[57] D. Geiger, T. Liu, and R.V. Kohn. Representation and self-similarity of shapes. *IEEE Trans. on Pattern Analysis and Machine Intelligence*, 25-1:86–99, January 2003.

[58] T. Georgiev, C. Zheng, S. Nayar, B. Curless, D. Salasin, and C. Intwala. Spatio-angular resolution trade-offs in integral photography. In *Eurographics Symposium on Rendering*, pages 263–272, 2006.

[59] G. Golub and C.V. Loan. *Matrix Computations.* The Johns Hopkins University Press, Baltimore, 1989.

[60] S. Gong and T. Xiang. Recognition of group activities using dynamic probabilistic networks. *Computer Vision, 2003. Proceedings. Ninth IEEE International Conference on*, pages 742–749, 2003.

[61] N.J. Gordon, D.J. Salmond, and A.F.M Smith. Novel approach to nonlinear/non-gaussian babayesian state estimation. *IEE Proceedings on Radar and Signal Processing*, 140:107–113, 1993.

[62] S.J. Gortler, R. Grzeszczuk, R. Szeliski, and M.F. Cohen. The lumigraph. In *SIGGRAPH*, pages 43–54, 1996.

[63] A. Goshtasby. Description and discrimination of planar shapes using shape matrices. *IEEE Trans. on Pattern Analysis and Machine Intelligence*, 7:738–743, 1985.

[64] Stephen R. Gottesman and E. E. Fenimore. New family of binary arrays for coded aperture imaging. *Appl. Optics*, 28(20):4344–4352, Oct 1989.

[65] A. Gritai, Y. Sheikh, and M. Shah. On the use of anthropometry in the invariant analysis of human actions. *ICPR*, 2004.

[66] Paul Haeberli. A multifocus method for controlling depth of field. GraficaObscura, 1994.

[67] G.D. Hager and P.N. Belhumeur. Efficient region tracking with parametric models of geometry and illumination. *IEEE Trans. on Pattern Analysis and Machine Intelligence*, 20:1025–1039, 1998.

[68] J. Han and B. Bhanu. Individual recognition using gait energy image. *Workshop on Multimodal User Authentication (MMUA 2003)*, pages 181–188, December 2003.

[69] S. Hiura and T. Matsuyama. Depth measurement by the multi-focus camera. In *Conference on Computer Vision and Pattern Recognition*, pages 953–961, 1998.

[70] E. Hoenkamp. Perceptual cues that determine the labelling of human gait. *Journal of Human Movement Studies*, 4:59–69, 1978.

[71] S. Hongeng and R. Nevatia. Large-scale event detection using semi-hidden Markov models. *Computer Vision, 2003. Proceedings. Ninth IEEE International Conference on*, pages 1455–1462, 2003.

[72] M.K. Hu. Visual pattern recognition by moment invariants. *IRE Transactions on Information Theory*, 8:179–187, 1962.

[73] T. Huang, D. Koller, J. Malik, G. Ogasawara, B. Rao, S. Russell, and J. Weber. Automatic symbolic traffic scene analysis using belief networks. *Proceedings 12th National Conference in AI*, pages 966–972, 1994.

[74] S.S. Intille and A.F. Bobick. A framework for recognizing multi-agent action from visual evidence. *AAAI/IAAI*, 99:518–525, 1999.

[75] A. Isaksen, L. McMillan, and S.J. Gortler. Dynamically reparameterized light fields. In *SIGGRAPH*, pages 297–306, 2000.

[76] M. Isard and A. Blake. Contour tracking by stochastic propogation of conditional density. *European Conference on Computer Vision*, pages 343–356, 1996.

[77] M. Isard and A. Blake. Icondensation: Unifying low-level and high-level tracking in a stochastic framework. *European Conference on Computer Vision*, 1:767–781, 1998.

[78] H. Ives. Camera for making parallax panoramagrams. *J. Opt. Soc. Amer.*, 17:435–439, 1928.

[79] A.K. Jain. *Fundamentals of digital image processing*. Prentice-Hall, Inc. Upper Saddle River, NJ, USA, 1989.

[80] B. Javidi and F. Okano, editors. *Three-Dimensional Television, Video and Display Technologies*. Springer-Verlag, 2002.

[81] G. Johansson. Visual perception of biological motion and a model for its analysis. *PandP*, 14(2):201–211, 1973.

[82] G. E. Johnson, E. R. Dowski, and W. T. Cathey. Passive ranging through wave-front coding: Information and application. *Applied Optics*, 39:1700–1710, 2000.

[83] B.H. Juang and L.R. Rabiner. A probabilistic distance measure for hidden markov models. *ATT Technical Journal*, 64:391–408, 1985.

[84] A. Kale, AKR Chowdhury, and R. Chellappa. Towards a view invariant gait recognition algorithm. *Proceedings. IEEE Conference on Advanced Video and Signal Based Surveillance, 2003.*, pages 143–150, 2003.

[85] A. Kale, A.N Rajagopalan, Sundaresan.A., N. Cuntoor, A. Roy Cowdhury, V. Krueger, and R. Chellappa. Identification of humans using gait. *IEEE Transactions on Image Processing*, Under review.

[86] Karcher, H. Riemannian center of mass and mollifier smoothing. *Communications on Pure and Applied Mathematics*, 30:509–541, 1977.

[87] R. Kashyap and R. Chellappa. Stochastic models for closed boundary analysis: Representation and reconstruction. *IEEE Transactions on Information Theory*, 27:627–637, 1981.

[88] D.G. Kendall. Shape manifolds, procrustean metrics and complex projective spaces. *Bulletin of London Mathematical society*, 16:81–121, 1984.

[89] Z. Khan, T. Balch, and F. Dellaert. A rao-blackwellized particle filter for eigen tracking. *Conference on Computer Vision and Pattern Recognition*, 2004.

[90] A. Khotanzad and Y.H. Hong. Invariant image recognition by zernike moments. *IEEE Trans. on Pattern Analysis and Machine Intelligence*, 12(5):489–497, 1990.

[91] X. Koutsoukos and P. Antsaklis. Hierarchical control of piecewise linear hybrid dynamical systems based on discrete abstractions. *ISIS Technical Report*, Feb 2001.

[92] B. Laxton, J. Lim, and D. Kriegman. Leveraging temporal, contextual and ordering constraints for recognizing complex activities in video. *Computer Vision and Pattern Recognition, 2007. CVPR'07. IEEE Conference on*, pages 1–8, 2007.

[93] H.J. Lee and Z. Chen. Determination of 3d human body posture from a single view. *Computer Vision, Graphics, Image Processing*, 30:148–168, 1985.

[94] L. Lee, G. Dalley, and K. Tieu. Learning pedestrian models for silhoutte refinement. *International Conference on Computer Vision*, 2003.

[95] M. Levoy, B. Chen, V. Vaish, M. Horowitz, M. McDowall, and M. Bolas. Synthetic aperture confocal imaging. *ACM Trans. Graph.*, 23:825–834, 2004.

[96] M. Levoy and P. Hanrahan. Light field rendering. In *SIGGRAPH 96*, pages 31–42, 1996.

[97] G. Lippmann. Epreuves reversible donnant la sensation du relief. *J. Phys*, 7:821–825, 1908.

[98] C. Liu and N. Ahuja. A model for dynamic shape and its applications. *Conference on Computer Vision and Pattern Recognition*, 2004.

[99] J.S. Liu and R. Chen. Sequential monte carlo for dynamical systems. *Journal of the American Statistical Association*, 93:1031–1041, 1998.

[100] X. Liu and H.G. Mller. Functional convex averaging and synchronization for time-warped random curves. *J. American Statistical Association*, 99:687–699, 2004.

[101] Z. Liu and S. Sarkar. Improved gait recognition by gait dynamics normalization. *IEEE Transactions on Pattern Analysis and Machine Intelligence*, 28(6):863–876, 2006.

[102] S. Loncaric. A survey of shape analysis techniques. *Pattern Recognition*, 31(8):983–1001, 1998.

[103] M. Martnez-Corral, B. Javidi, R. Martnez-Cuenca, and G. Saavedra. Integral imaging with improved depth of field by use of amplitude-modulated microlens arrays. *Applied Optics*, 43:5806–5813, 2004.

[104] P. Maurel and G. Sapiro. Dynamic shapes average. *www.ima.umn.edu/preprints/may2003/1924.pdf*.

[105] C. Mazzaro, M. Sznaier, O. Camps, S. Soatto, and A. Bissacco. A model (in)validation approach to gait recognition. *1st International Symposium on 3D Data Processing Visualization and Transmission*, 2002.

[106] S. D. Mowbray and M. S. Nixon. Extraction and recognition of periodically deforming objects by continuous, spatio-temporal shape description. *Conference on Computer Vision and Pattern Recognition*, 2:895–901, 2004.

[107] F. Mura and N. Franceschini. Visual control of altitude and speed in a flight agent. *Proceedings of 3rd International Conference on Simulation of Adaptive Behaviour: From Animal to Animats*, pages 91–99, 1994.

[108] M. Murray, A. Drought, and R. Kory. Walking patterns of normal men. *Journal of Bone and Joint surgery*, 46-A(2):335–360, 1964.

[109] E. Muybridge. *The Human Figure in Motion*. Dover Publications, 1901.

[110] Shree K. Nayar, Vlad Branzoi, and Terry E. Boult. Programmable imaging: Towards a flexible camera. *International Journal of Computer Vision*, 70(1):7–22, 2006.

[111] S.K. Nayar and T. Mitsunaga. High dynamic range imaging: spatially varying pixel exposures. In *Conference on Computer Vision and Pattern Recognition*, volume 1, pages 472–479, 2000.

[112] T.R. Neumann and H.H. Bulthoff. Insect inspired visual control of translatory flight. *Proceedings of the 6th European Conference on Artificial Life ECAL 2001*, pages 627–636, 2001.

[113] R. Ng, M. Levoy, M. Brdif, G. Duval, M. Horowitz, and P. Hanrahan. Light field photography with a hand-held plenoptic camera. Technical report, Stanford Univ., 2005.

[114] Ren Ng. Fourier slice photography. *ACM Trans. Graph.*, 24:735–744, 2005.

[115] S.A. Niyogi and E.H. Adelson. Analyzing and recognizing walking figures in xyt. Technical Report 223, MIT Media Lab Vision and Modeling Group, 1994.

[116] S. M. Oh, J. M. Rehg, T. Balch, and F. Dellaert. Learning and inference in parametric switching linear dynamic systems. *IEEE International Conference on Computer Vision*, 2005.

[117] S. M. Oh, J. M. Rehg, T. Balch, and F. Dellaert. Parameterized duration modeling for switching linear dynamic systems. *IEEE International Conference on Computer Vision and Pattern Recognition*, 2006.

[118] F. Okano, J. Arai, H. Hoshino, and I. Yuyama. Three dimensional video system based on integral photography. *Optical Engineering*, 38:1072–1077, 1999.

[119] F. Okano, H. Hoshino, and A.J. Yuyama. Real-time pickup method for a three-dimensional image based on integral photography. *Applied Optics*, 36:15981603, 1997.

[120] Alan V. Oppenheim, Ronald W. Schafer, and John R. Buck. *Discrete-Time Signal Processing*. Prentice-Hall, 1999.

[121] P.V. Overschee and B.D. Moor. Subspace algorithms for the stochastic identification problem. *Automatica*, 29:649–660, 1993.

[122] V. Parameswaran and R. Chellappa. View invariants for human action recognition. *CVPR*, 2003.

[123] S. Park and JK Aggarwal. Recognition of two-person interactions using a hierarchical Bayesian network. *International Multimedia Conference*, pages 65–76, 2003.

[124] S. Parui, E. Sarma, and D. Majumder. How to discriminate shapes using the shape vector. *Pattern Recognition Letters*, 4:201–204, 1986.

[125] T. Pavlidis. A review of algorithms for shape analysis. *Computer Graphics and Image Processing*, 7:243–258, 1978.

[126] V. Pavlovic, J. Rehg, T.J. Cham, and K. Murphy. A dynamic bayesian network approach to figure tracking using learned dynamic models. *ICCV*, 1999.

[127] E. Persoon and K.S. Fu. Shape Discrimination Using Fourier Descriptors. *IEEE Transactions on Systems, Man and Cybernetics*, 7(3):170–179, 1977.

[128] G. Petschnigg, M. Agrawala, H. Hoppe, R. Szeliski, M. Cohen, and K. Toyama. Digital photography with flash and no-flash image pairs. *ACM Trans. Graph.*, 23(3):664–672, August 2004.

[129] J. Phillips, S. Sarkar, I. Robledo, P. Grother, and K.W. Bowyer. The gait identification challenge problem: Data sets and baseline algorithm. *Intl. Conference on Pattern Recognition*, August 2002.

[130] M.J. Prentice and K.V. Mardia. Shape changes in the plane for landmark data. *The annals of statistics*, 23-6:1960–1974, 1995.

[131] L. Rabiner and B. Juang. *Fundamentals of speech recognition.* Prentice Hall, 1993.

[132] A. Rangarajan, H. Chui, and F.L. Bookstein. The softassign procrustes matching algorithm. *Information Processing in medical imaging*, pages 29–42, Springer 1997.

[133] C. Rao, A. Yilmaz, and M. Shah. View-invariant representation and recognition of actions. *IJCV*, 2002.

[134] Ramesh Raskar, Amit Agrawal, and Jack Tumblin. Coded exposure photography: motion deblurring using fluttered shutter. *ACM Trans. Graph.*, 25(3):795–804, 2006.

[135] C.A. Ratanamahatana and E. Keogh. Making time-series classification more accurate using learned constraints. *Proceedings of SIAM International Conference on Data Mining*, pages 11–22, 2004.

[136] S. Rusinkiewicz. A survey of brdf representation for computer graphics. *available via the WWW at http://graphics. stanford. edu/smr/cs348c/surveypaper. html*.

[137] S. Sarkar, P.J. Phillips, Z. Liu, I.R. Vega, P. Grother, and K.W. Bowyer. The humanid gait challenge problem: data sets, performance, and analysis. *IEEE Trans. on Pattern Analysis and Machine Intelligence*, pages 162–177, Feb 2005.

[138] Y.Y. Schechner, S.K. Nayar, and P.N. Belhumeur. Multiplexing for Optimal Lighting. *IEEE TRANSACTIONS ON PATTERN ANALYSIS AND MACHINE INTELLIGENCE*, pages 1339–1354, 2007.

[139] T. D. Seeley. The tremble dance of the honeybee: message and meanings. *Behavioral Ecology and Sociobiology*, 31:375–383, 1992.

[140] E. Shechtman and M. Irani. Space-time behavior based correlation. *Computer Vision and Pattern Recognition, 2005. CVPR 2005. IEEE Computer Society Conference on*, 1, 2005.

[141] Y. Sheikh and M. Shah. Exploring the space of an action for human action recognition. *ICCV*, Oct 2005.

[142] G. K. Skinner. X-Ray Imaging with Coded Masks. *Scientific American*, 259:84, August 1988.

[143] C. Sminchisescu and B. Triggs. Covariance scaled tracking for monocular 3d body tracking. *Conference on Computer Vision and Pattern Recognition*, 2001.

[144] S. Soatto, G. Doretto, and Y.N. Wu. Dynamic textures. *International Conference on Computer Vision*, 2:439–446, 2001.

[145] M.V. Srinivasan, S.W. Zhang, M. Lehrer, and T.S. Collett. Honeybee navigation en route to the goal: visual flight control and odometry. *The Journal of Experimental Biology*, 199:237–244, 1996.

[146] A. Srivasatava and E. Klassen. Bayesian geometric subspace tracking. *Advances in Applied Probability*, 36(1):43–56, March 2004.

[147] A. Srivastava, I. Jermyn, and S. H. Joshi. Riemannian analysis of probability density functions with applications in vision. In *CVPR*, 2007.

[148] A. Srivastava, S. H. Joshi, W. Mio, and X. Liu. Statistical shape analysis: Clustering, learning and testing. *IEEE Transactions on Pattern Analysis and Machine Intelligence*, 27(4):590–602, 2005.

[149] A. Srivastava, W. Mio, E. Klassen, and S. Joshi. Geometric analysis of continuous, planar shapes. *Proc. 4th International Workshop on Energy Minimization Methods in Computer Vision and Pattern Recognition*, 2003.

[150] W. Sun and G. Barbastathis. Rainbow volume holographic imaging. *Opt. Lett.*, 30:976–978, 2005.

[151] R. Tanawongsuwan and A. Bobick. Modelling the effects of walking speed on appearance-based gait recognition. *Conference on Computer Vision and Pattern Recognition*, 2:783–790, 2004.

[152] D. Tolliver and R.T. Collins. Gait shape estimation for identification. *4th Intl. Conf. on AVBPA*, June 2003.

[153] P. Turaga, A. Veeraraghavan, and R. Chellappa. Unsupervised View and Rate Invariant clustering of Video Sequences. *Elsevier Journal on Computer Vision and Image Understanding*, Under Review.

[154] V. Vaish, B. Wilburn, N. Joshi, and M Levoy. Using plane + parallax for calibrating dense camera arrays. In *Conference on Computer Vision and Pattern Recognition*, pages 2–9, 2004.

[155] J. van der Gracht, E.R. Dowski, M. Taylor, and D. Deaver. Broadband behavior of an optical-digital focus-invariant system. *Optics Letters*, 21(13):919–921, July 1996.

[156] N. Vaswani. Change detection in partially observed nonlinear dynamic systems with unknown change parameters. *American Control Conference*, 2004.

[157] N. Vaswani. Additive change detection in nonlinear systems with unknown change parameters. *IEEE Transactions on Signal Processing*, page accepted, 2006.

[158] N. Vaswani, A. RoyChowdhury, and R. Chellappa. "shape activities" : A continuous state hmm for moving/deforming shapes with application to abnormal activity detection. *IEEE Trans. on Image Processing*, Accepted for Publication- 2004.

[159] A. Veeraraghavan, R. Chellappa, and A.K. Roy-Chowdhury. The Function Space of an Activity. *Proceedings of the 2006 IEEE Computer Society Conference on Computer Vision and Pattern Recognition-Volume 1*, pages 959–968, 2006.

[160] A. Veeraraghavan, R. Raskar, A. Agrawal, A. Mohan, and J. Tumblin. Dappled photography: Mask enhanced cameras for heterodyned light fields and coded aperture refocusing. *ACM Trans. Graph.*, 26(3):69, 2007.

[161] A. Veeraraghavan, AK Roy-Chowdhury, and R. Chellappa. Matching Shape Sequences in Video with Applications in Human Movement Analysis. *Pattern Analysis and Machine Intelligence, IEEE Transactions on*, 27(12):1896–1909, 2005.

[162] A. Veeraraghavan, A. RoyChowdhury, and R. Chellappa. Role of shape and kinematics in human movement analysis. *CVPR*, 2004.

[163] Ashok Veeraraghavan, Ramesh Raskar, Amit Agrawal, Ankit Mohan, and Jack Tumblin. Non-refractive modulators for coding and capturing scene appearance. Technical Report UMIACS-TR-2007-21, Univ. of Maryland, 2007.

[164] R. C. Veltkamp and M. Hagedoorn. State of the art in shape matching. *Technical Report UU-CS-1999-27, Utrecht*, 27, 1999.

[165] G.V. Veres, L. Gordon, J.N. Carter, and M.S. Nixon. What image information is important in silhouette based gait recognition? *Conference on Computer Vision and Pattern Recognition*, 2:776–782, 2004.

[166] C. Vogler and D. Metaxas. ASL recognition based on a coupling between HMMs and 3D motion analysis. *International Conference on Computer Vision*, pages 363–369, 1998.

[167] L. Wang, H. Ning, W. Hu, and T. Tan. Gait recognition based on Procrustes shape analysis. *International Conference on Image Processing*, 2002.

[168] Shuzhen Wang and Wolfgang Heidrich. The design of an inexpensive very high resolution scan camera system. *Eurographics*, 23:441–450, 2004.

[169] D. Weinland, R. Ronfard, and E. Boyer. Automatic Discovery of Action Taxonomies from Multiple Views. *Proceedings of the 2006 IEEE Computer Society Conference on Computer Vision and Pattern Recognition-Volume 2*, pages 1639–1645, 2006.

[170] D. Weinland, R. Ronfard, and E. Boyer. Free viewpoint action recognition using motion history volumes. *Computer Vision and Image Understanding*, 104(2-3):249–257, 2006.

[171] Bennett Wilburn, Neel Joshi, Vaibhav Vaish, Eino-Ville Talvala, Emilio Antunez, Adam Barth, Andrew Adams, Mark Horowitz, and Marc Levoy. High performance imaging using large camera arrays. *ACM Trans. Graph.*, 24(3):765–776, 2005.

[172] A.D. Wilson and A.F. Bobick. *Learning visual behavior for gesture analysis*. Perceptual Computing Section, Media Laboratory, Massachusetts Institute of Technology, 1995.

[173] Y. Xu and A. Roy-Chowdhury. Integrating motion, illumination and structure in video sequences, with applications in illumination-invariant tracking. *Accepted for Publication at IEEE Transactions on Pattern Analysis and Machine Intelligence*, 2006.

[174] Jason C. Yang. A light field camera for image based rendering. Master's thesis, Massachussettes Institute of Technology, 2000.

[175] A.J. Yezzi and S. Soatto. Deformotion: Deforming motion, shape average and the joint registration and approximation of structure in images. *International Journal of Computer Vision*, 53(2):153–167, 2003.

[176] L. Zelnik-Manor and M. Irani. Event-based analysis of video. *Computer Vision and Pattern Recognition, 2001. CVPR 2001. Proceedings of the 2001 IEEE Computer Society Conference on*, 2, 2001.

[177] T. Zhao and R. Nevatia. 3d tracking of human locomotion: a tracking as recognition approach. *ICPR*, 2002.

[178] T. Zhao, T.S. Wang, and H.Y. Shum. Learning a highly structured motion model for 3d human tracking. *Proc. of 5th Asian Conference on Computer Vision*, 2002.

[179] S.K. Zhou, R. Chellappa, and B. Moghaddam. Visual tracking and recognition using appearance-adaptive models in particle filters. *IEEE Trans. on Image Processing*, 11:1434–1456, 2004.

[180] A. Zomet and S.K. Nayar. Lensless imaging with a controllable aperture. In *Conference on Computer Vision and Pattern Recognition*, pages 339–346, 2006.